TID INDUCED SMALL SIGNAL MODEL VARIATION IN CMOS AND SiGe BiCMOS

by

Brilliant Habeenzu

Submitted in partial fulfilment of the requirements for the degree

Philosophiae Doctor (Electronic Engineering)

in the

Department of Electrical, Electronic and Computer Engineering

Faculty of Engineering, Built Environment and Information Technology

UNIVERSITY OF PRETORIA

January 2019

SUMMARY

TID-INDUCED SMALL SIGNAL MODEL VARIATION IN CMOS AND SiGe BiCMOS

by

Brilliant Habeenzu

Promotor: Dr. T. Stander

Department: Electrical, Electronic and Computer Engineering

University: University of Pretoria

Degree: Philosophiae Doctor (Electronic Engineering)

Keywords: Silicon germanium (SiGe), Heterojunction bipolar transistors (HBT), complementary metal oxide semiconductor (CMOS), radiation, Radiation dosage, Total ionizing dose (TID), Parameter extraction, Millimeter wave measurements, Noise modelling, Noise figure

The thesis presents data, and fitting equations, that model the degradation of linear small signal parameters for SiGe HBT and bulk CMOS devices due to TID irradiation damage.

The 0.13 µm SiGe HBT was fabricated with a base of 4.5 µm in common emitter configuration with the substrate tied to emitter and connected to ground. The device was exposed to electron radiation using the Sr 90 source. Linear measurements were done in the frequency range of 1 GHz to 110 GHz before and after incremental radiation doses. The measured S-parameters were de-embedded using SHORT and OPEN calibration standards to remove the effect of parasitics from pads, vias and feedlines, and shift the calibration plane to the terminals of the device. Small signal parameters and noise parameters were extracted from the de-embedded S-parameter pre-and post-radiation. The major model variations due to total ionizing dose (TID) were found to be an increase in junction resistances and capacitances, as well as a reduction in transconductance. These result in a decrease in the

unilateral gain (U), f_t and f_{max}, as reported in prior literature. Exponential regression and curve fitting techniques were employed to derive model equations for the line of best fit for each of the small signal parameter. The coefficient of determination was calculated to ascertain the accuracy of the established equations. Through the coefficient of determination, it was observed that all the derived equations were reliable and could be used to predict the performance of a transistor at a given radiation dose. Performance degradation up to 10 Mrad dose was predicted using extrapolation from small-signal model parameters.

Noise modelling was also conducted using measured S-parameters at incremental radiation doses. The modelled noise figure was compared to the simulated noise figure from the model in the process design kit (PDK), with good agreement observed.

Four 0.35 µm bulk CMOS devices were fabricated with different gate widths in common source configuration with the substrate tied to the source and connected to ground. The devices were exposed to electron radiation. Linear measurement was done pre- and post-irradiation in the frequency range of 1 GHz to 50 GHz with a vector network analyser (VNA). The measured S-parameters were de-embedded using THRU, REFLECT and LINE calibration standards. Small signal parameters were extracted from the de-embedded S-parameters before and at incremental radiation dose. The major model variations due to total ionizing dose exposure were increases in the gate resistance (R_g), gate drain capacitance (C_{gd}) and gate source capacitance (C_{gs}), with a reduction in transconductances (g_m and g_{ds}). This caused S_{11} and S_{22} to become more resistive as d was increased, with a decrease in the unilateral gain, f_T and f_{max}. A curve fitting tool was used to derive equations for the curves of best fit for each of the small signal parameters. Coefficient of determination values were calculated to evaluate the accuracy of the curves of best fit. Good fitting was observed. The application of the data in predictive modelling of radiation damage was demonstrated.

This study represents the first effort in published literature to model TID-induced changes to small-signal CMOS and SiGe BiCMOS models at mm-wave frequencies, and the results support previously published data on degradation of S-parameters and other performance metrics.

LIST OF ABBREVIATIONS

BiCMOS	Bi Complementary Metal Oxide Semiconductor
BJT	Bipolar Junction Transistor
CMOS	Complementary Metal Oxide Semiconductor
DD	Displacement Damage
DRC	Design Rule Checking
DUT	Device Under Test
ERB	Earth Radiation Belt
ESCC	European Space Components Coordination
GCR	Galactic Cosmic Rays
GSG	Ground Signal Ground
HBT	Heterojunction Bipolar Transistor
ISS	Impendence Substrate Standard
LEO	Low Earth Orbit
LVS	Layout Versus Schematic
MOS	Metal Oxide Semiconductor
NMOS	Negative Metal Oxide Semiconductor
SEE	Single Event Effects
SiGe	Silicon Germanium
SPE	Solar Particle Events
TID	Total Ionizing Dose
VNA	Vector Network Analyser

LIST OF SYMBOLS

B	Radiation activity
ε_r	Dielectric constant
k_c	Conversion factor
s	Dose rate
$\emptyset$	Fluence rate
R_n	Noise Resistance
Y	Admittance
G	Conductance
B	Susceptance
NF	Noise figure
d	Total radiation dose
$S_{\{mn\}}$	Two-port scattering parameters
$Y_{\{mn\}}$	Two-port admittance parameters
$H_{\{mn\}}$	Two-port hybrid parameters
$Z_{\{mn\}}$	Two-port impedance parameters

TABLE OF CONTENTS

CHAPTER 1 INTRODUCTION ... 1

1.1 PROBLEM STATEMENT ... 1

1.1.1 Context of the problem ... 1

1.1.2 Research gap ... 3

1.2 RESEARCH OBJECTIVES ... 3

1.3 APPROACH ... 3

1.4 RESEARCH GOALS ... 4

1.5 RESEARCH CONTRIBUTION ... 4

1.6 RESEARCH OUTPUTS ... 5

1.7 THESIS OVERVIEW ... 5

CHAPTER 2 LITERATURE STUDY ... 7

2.1 CHAPTER OVERVIEW ... 7

2.2 SMALL SIGNAL MODELS FOR TRANSISTORS ... 7

2.2.1 Small signal models for BJT and HBT devices ... 8

2.2.2 Noise models for BJT and HBT devices ... 13

2.2.3 Small signal models for bulk CMOS devices 15
2.3 IONIZING RADIATION IN SPACE 17
2.4 RADIATION EFFECT IN SiGe HBT 19
2.4.1 Radiation effect on DC performance of SiGe HBTs 20
2.4.2 Radiation effect on the RF and noise performance of SiGe HBTs 20
2.5 RADIATION EFFECTS IN BULK CMOS DEVICES 21
2.5.1 Radiation effect on DC performance of bulk CMOS devices 21
2.5.2 Radiation effect on RF performance of bulk CMOS devices 22
2.6 CHAPTER SUMMARY 23

CHAPTER 3 METHODOLOGY 24
3.1 DESIGN OF THE 0.13 µm SiGe HBT AND CALIBRATION STANDARDS ... 24
3.2 DESIGN OF THE 0.35 µm CMOS TRANSISTORS AND CALIBRATION STANDARDS 30
3.3 IRRADIATION OF DEVICES 34
3.3.1 Radiation experiment methods and procedures 34
3.3.2 Radiation experiment setup... 35
3.3.3 Fluence rate calculation 36
3.3.4 Determination of dose rate and radiation dose 39
3.3.5 Radiation exposure of SiGe HBT 39
3.3.6 Radiation exposure of bulk CMOS devices.. 40
3.4 S-PARAMETER MEASUREMENTS 40
3.5 MODEL EXTRACTION 42
3.5.1 Linear small signal model extraction for SiGe HBT 42
3.5.2 Noise model 48
3.5.3 Model for the 0.35 µm AMS CMOS Devices 49
3.6 CURVE FITTING AND MODEL EXTRAPOLATION...................................... 53
3.7 CHAPTER SUMMARY 54

CHAPTER 4 SiGe BiCMOS RESULTS 56
4.1 SMALL SIGNAL MODEL PRE-AND POST-RADIATION.............................. 56
4.2 SIMULATION, MODEL AND MEASUREMENT RESULTS 57
4.3 NOISE FIGURE SIMULATION AND MODELLING RESULTS 59
4.4 CURVE FITTING FOR INTRINSIC SMALL SIGNAL PARAMETERS........... 60
4.5 MODEL VALIDATION AND USAGE DEMOSTRATION 61

4.6 CHAPTER SUMMARY 64

CHAPTER 5 BULK CMOS RESULTS 65

5.1 SMALL SIGNAL MODEL PRE-AND POST-RADIATION 65

5.2 SIMULATION, MODEL AND MEASUREMENT RESULTS 67

5.3 CURVE FITTING AND REGRESSION METHOD FOR SMALL SIGNAL PARAMETERS 74

5.4 MODEL VALIDATION AND USAGE DEMONSTRATION 76

5.4.1 Model validation and usage demonstration for the model of the NMOS device with total gate width of 5 µm 76

5.4.2 Model validation and usage demonstration for the model of the NMOS device with total gate width of 10 µm 79

5.4.3 Model validation and usage demonstration for the model of the NMOS device with total gate width of 25 µm 81

5.4.4 Model validation and usage demonstration for the model of the NMOS device with total gate width of 50 µm 83

5.5 CHAPTER SUMMARY 85

CHAPTER 6 DISCUSSION 86

6.1 PHYSICAL INTERPRETATION OF MODEL CHANGES IN SiGe HBT 86

6.2 IMPACT OF RADIATION ON THE PERFORMANCE OF SiGe HBT 87

6.3 PHYSICAL INTERPRETATION OF MODEL CHANGES IN BULK CMOS DEVICES 91

6.4 IMPACT OF RADIATION ON THE PERFORMANCE OF CMOS DEVICES . 92

6.4.1 Impact of radiation on NMOS device with total gate width of 5 µm 92

6.4.2 Impact of radiation on NMOS device with total gate width of 10 µm 95

6.4.3 Impact of radiation on NMOS device with total gate width of 25 µm 99

6.4.4 Impact of radiation on NMOS device with total gate width of 50 µm 102

CHAPTER 7 CONCLUSION 106

7.1 GENERAL CONCLUSION BASED ON THE DISCUSSION 106

7.1.1 General conclusion on SiGe HBT 106

7.1.2 General conclusion on bulk CMOS devices 107

7.2 CONCLUSION BASED ON RESEARCH OBJECTIVES 108

7.3 LIMITATIONS AND CHALLENGES 108

7.4 RECOMMENDATIONS FOR FUTURE WORKS 109

REFERENCES 111

APPENDICES 116

CHAPTER 1 INTRODUCTION

1.1 PROBLEM STATEMENT

There has been an increase in demand for bandwidth in space-based communication applications in the recent past. This has led to an increase in research seeking to exploit the available bandwidth in the millimetre wave (mm-wave) frequency band (30GHz to 300GHz) for space based applications [1]. Space-based systems are, however, exposed to ionizing radiation with a potential to degrade small signal parameters for microelectronics at device level, leading to system failure. Ionizing radiation can also lead to degradation of noise performance, as well as shifts in biasing voltages in transistors. Accurate prediction of the degradation of small signal parameters in transistors at mm-wave frequencies is important in determining the lifespan of microelectronic circuits operating in ionizing radiation environments at mm-wave frequencies. This study aims to derive adaptive model parameters from experimental data that relates degradation of small signal characteristics of silicon germanium heterojunction bipolar transistors (SiGe HBTs) and bulk complementary metal oxide semiconductor (CMOS) devices at mm-wave frequencies to total ionizing dose (TID).

1.1.1 Context of the problem

The availability of the unlicensed and lightly licenced spectrum in the mm-wave frequency bands, has led to an increased amount of research towards SiGe HBTs and bulk CMOS at mm-wave frequencies in the recent past. This is evident from the space-based applications for mm-wave transceivers which have been proposed in [2], where devices will be exposed to ionizing radiation.

Three forms of radiation effects are typically considered in space, namely displacement damage (DD), single event effects (SEE) and total ionizing dose (TID) [3].

DD is a cumulative long-term nonionizing damage caused by particles with high momentum; mainly protons, but also electrons and secondary neutrons. These particles displace the silicon atom from the lattice of the silicon based semiconductor device. This produces defects known as “traps” in the semiconductor lattice of materials that result in degradation of properties such as the dielectric constant [4].

SEE, on the other hand is caused by highly energetic particles which deposit electron-hole pairs as they transit the semiconductor. The particles are swept into the transistor terminals, causing voltage and current transients, thereby creating unwanted circuit responses. SEE cannot easily be shielded against [3].

TID is a cumulative long-term ionizing damage due mainly to protons and electrons that ionizes and damages devices at an atomic level. It causes traps or induced incomplete bonding which leads to threshold voltage shifts in transistors, increased leakage current, and transconductance (g_m) variations. Damage first manifests as parametric degradation of the device, but can ultimately result in functional failure [5].

Since both DD and TID damage is cumulative, devices that are exposed to TID and DD are expected to degrade and eventually fail after some time as the radiation dose would have accumulated to levels that would damage the device at atomic level. It is expected, however, that DD will take longer than TID to accumulate to the level that would damage devices, since its energy is lower than that of TID. Investigating the manner in which DD affects devices requires a considerable long period of time than TID. It is, however, known from literature that TID and DD causes similar effects on devices, except for the extent of the damage and the period it takes to cause the damage due to differences in the energy of the two.

The focus of this study, therefore, falls on degradation of small signal parameters due to TID in SiGe HBTs and bulk CMOS devices at mm-wave frequencies.

1.1.2 Research gap

The following research gap is addressed in this study.

i. The current body of knowledge contains numerous small signal device circuit models for both for SiGe HBTs and bulk CMOS devices. These models relate small signal characteristics to complex linear 2-port parameters over frequency at a specific bias point. However, none of these models establish a relationship between changes in the small signal parameters of a transistor to the radiation dose the device has been exposed to.

ii. Numerous studies have published the degradation of S-parameters and associated performance metric (f_T, f_{max}, etc.) [6] due to incremental TID damage. These results have, however, always been presented as macro-effects; the internal small-signal model changes have never been studied explicitly.

1.2 RESEARCH OBJECTIVES

The research study will have two objectives.

i. To model changes in the small signal parameters of devices at constant voltage bias against TID in SiGe HBT.
ii. To model changes in the small signal parameters of devices at constant voltage bias against TID in bulk CMOS devices.

1.3 APPROACH

A variety of SiGe HBT and bulk CMOS transistors were prototyped. The SiGe HBT was connected in common emitter configuration with its body tied to the emitter and grounded, while CMOS devices were connected in common source configuration with their bodies tied to the source and grounded. Simulations were performed to determine the bias conditions for maximum f_T as well as excitation power levels that ensure small signal operation.

Linear measurements were done in the frequency range of 1 GHz up to 110 GHz for the biased SiGe HBT and in the frequency range of 1 GHz to 50 GHz for biased bulk CMOS devices. The devices were then subjected to ionizing electron radiation with their terminals floating for selected periods to enable them absorb varying radiation doses. Linear measurements were then repeated after each incremental radiation experiment cycle. Small signal parameters were extracted from measured S-parameters before and after each incremental radiation dose. Data fitting methods were then used to derive equations relating the extracted small signal parameters to radiation dose.

1.4 RESEARCH GOALS

The following are the goals of this research study:

i. To study the effect of TID on individual small signal model parameters for SiGe HBTs and bulk CMOS devices at microwave and mm-wave frequencies.
ii. To derive expressions that relate changes in model parameters to radiation dose at microwave and mm-wave frequencies for SiGe HBT and bulk CMOS devices respectively.

1.5 RESEARCH CONTRIBUTION

i. The effect of TID on individual small signal model parameters in SiGe HBT and bulk CMOS devices at microwave and mm-wave frequencies has been established.
ii. Expressions relating small signal parameters to radiation dose have been derived.

.

1.6 RESEARCH OUTPUTS

i. B. Habeenzu, W. Meyer and T. Stander, "Effect of electron radiation on small signal and noise model parameters in SiGe HBT at mm-wave frequencies," *IEEE Trans. Nucl. Sci.* (Submitted), 2019.

ii. B. Habeenzu, W. Meyer and T. Stander, "Effect of electron radiation on small signal parameters for bulk CMOS devices at microwave and mm-wave frequencies," *IEEE Trans. Nucl. Sci.* (Submitted), 2019.

1.7 THESIS OVERVIEW

In Chapter 2 a literature study is performed, in which the effect of radiation on microelectronic devices is covered. Various small signal models for both the SiGe HBT and bulk CMOS devices are reviewed to select the most suitable ones for the 0.13 μm SiGe HBTs and 0.35 μm NMOS at mm-wave frequencies.

In Chapter 3 the research methodology is discussed. The details of the experimental setup and procedure are presented, including the choice of radiation source, offset distance, and dose rates. Calibration, de-embedding and measurements of S-parameters are discussed in this chapter. The chapter further discusses model extraction methods as well as regression and data fitting techniques for derivation of model equations.

In Chapter 4, the extracted small signal model parameters are presented. A comparison of simulated S-parameters from the extracted model to the measured S-parameters, as well as to S-parameters simulated from the model of the PDK, is presented. This is followed by a presentation of a comparison of the modelled noise figure from measured S-parameters to the simulated noise figure from the model of the PDK. The chapter then presents equations relating the extracted small signal parameters to radiation dose derived though data fitting, and concludes with the validation of the model and a check on its ability to predict changes in small signal parameters at high radiation doses.

In Chapter 5, the extracted small signal model parameters for four NMOS devices with different gate widths at various radiation doses are presented. A comparison of S-parameters simulated from the extracted model to measured S-parameters, as well as to S-parameters simulated from the model of the PDK, is done for each of the four CMOS devices. The chapter then presents extracted equations relating changes in small signal model parameters to radiation dose for the four CMOS devices and ends with a presentation on the validation of the extracted small signal parameter equations and their ability to predict changes as radiation dose is increased.

Chapter 6 gives a detailed discussion and analysis of the results presented in Chapter 4 and Chapter 5 while concluding remarks and proposed future works are presented in Chapter 7.

CHAPTER 2 LITERATURE STUDY

2.1 CHAPTER OVERVIEW

The chapter presents an overview of the body of scholarly literature in various topics related to this study. The first part of this chapter discusses small signal models for BJT and HBT devices, as well as small signal models for bulk CMOS devices. A detailed review of parameter extraction methods for the models, and the strength and weaknesses for each of the parameter extraction model are discussed. Following this, ionizing radiation in space, particularly in the low earth orbit (LEO), is discussed. This is followed by a discussion on the effect of TID on transistors. The chapter concludes with a discussion on radiation effects on DC performance, as well as RF and noise performance of SiGe HBT and the effect of radiation on DC and RF performance of bulk CMOS devices.

2.2 SMALL SIGNAL MODELS FOR TRANSISTORS

Transistor modelling is the analysis and prediction of the behaviour of a transistor towards small signals and/or large signals. The behaviour of the transistor can be modelled using linear and nonlinear models, as well as compact models, which are used by simulators such as Keysight ADS and Cadence Spectre (integrated in Cadence Virtuoso) [11, 12]. Linear small signal models are still often used in the design of small signal components such as low noise amplifiers, as they model relationships which are easy to analyse. Compact models, on the other hand, model far more complex relationship than can be analysed through manual calculations. Linear models consist of extrinsic and intrinsic linear circuit elements which are typically extracted using S-parameter measurements. Nonlinear model extraction, on the

other hand, uses pulsed IV and CV measurements in addition to S-parameters to study electrical performance in safe operating regions [13].

An extensive literature review has revealed numerous models for both HBTs and CMOS transistors. Among the models are compact models, such as the Gummel Poon [7]–[11] and Mextram [12], [13] models, as well as linear small signal models such as the hybrid-π and T-model. Compact models model the response of a transistor in a circuit model irrespective of bias point, but need to be populated with a large amount of model parameter values through a long series of measurements. This typically requires specialised software such as IC-CAP [16]. Linear models, on the other hand, can have their parameters easily extracted from IV, CV and RF measurements but are typically only valid under a single bias point and small signal operation. Linear models can be applied to components such as LNAs under small signal operation at a single bias point, and have therefore been chosen in this study. A literature review has revealed numerous methods of extracting small signal model parameters at microwave and mm-wave frequencies.

2.2.1 Small signal models for BJT and HBT devices

In [14], a SiGe HBT small signal and high frequency noise model is proposed. This model's small signal equivalent circuit under forward active operation with grounded emitter is shown in Figure 2.1. To extract the small signal parameters, a semi-automatic on-wafer probe station connected to the Agilent 4155 semiconductor parameter analyser for the measurement of DC characteristics is used, along with an HP 8510 network analyser for measurement of S-parameters up to 40 GHz. Measured S-parameters are de-embedded using OPEN and SHORT calibration standards to remove both parallel and series contact pad parasitics from measurements. This model has only been validated up to 40 GHz and may not be reliable at mm-wave frequencies. The disadvantage of this model is that it requires curve fitting to be performed on measurements from the parameter analyser. This implies setting up an additional measurement during the time sensitive radiation experiment measurement cycle.

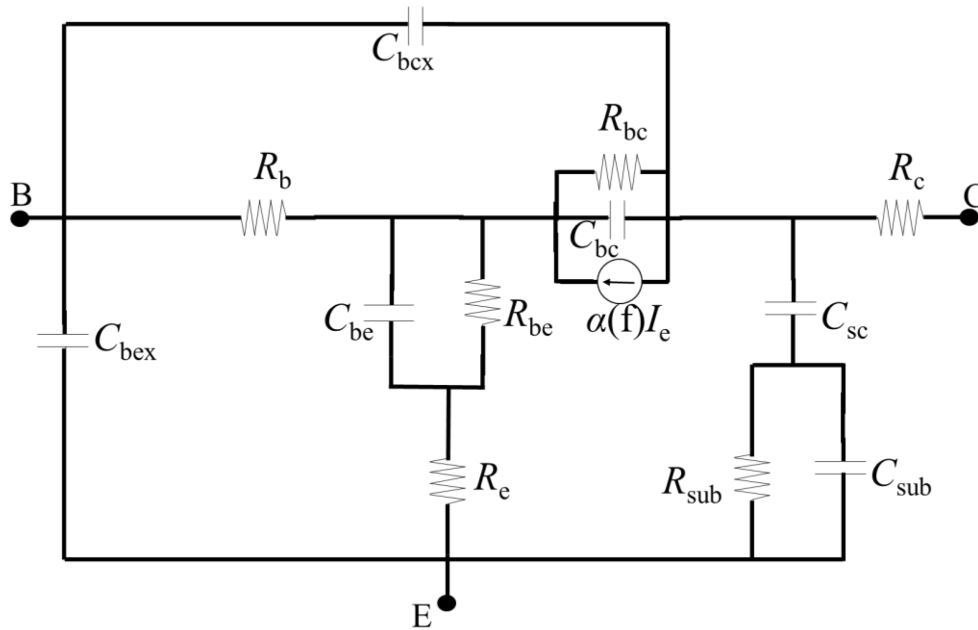

Figure 2.1: Small signal equivalent circuit model for SiGe HBT as proposed by [14]

Another method for determining HBT small signal model parameters using analytical methods is proposed in [15]. In this model, the small signal circuit is divided into two parts as shown in Figure 2.2. The outer part represents the bias independent extrinsic model, whereas the inner part represents the bias-dependent intrinsic device. This model differs from the previous one as it has the base resistance divided into two parts, with one being the extrinsic base resistance (R_b) while the other one is the intrinsic base resistance (R_{bb}). Furthermore, it takes into account parasitic inductances at the base, collector and emitter, which are not accounted for in the previous model. While the previous model accounts for the substrate network, this model does not. To extract small signal parameters, the transistor is initially biased in the forward active region of operation with a high base current to extract parasitic resistances and inductances. The transistor is then biased in cut off with the resulting S-parameters used to extract the parasitic capacitances. The values of all the parasitic elements in the extrinsic device are used to de-embed the measured S-parameters of the device so as to obtain the S-parameters of the intrinsic device using equations given in [15]. This model, however, has only been validated on an HBT device for frequencies up to 30 GHz and may not be accurate for frequencies beyond 30 GHz.

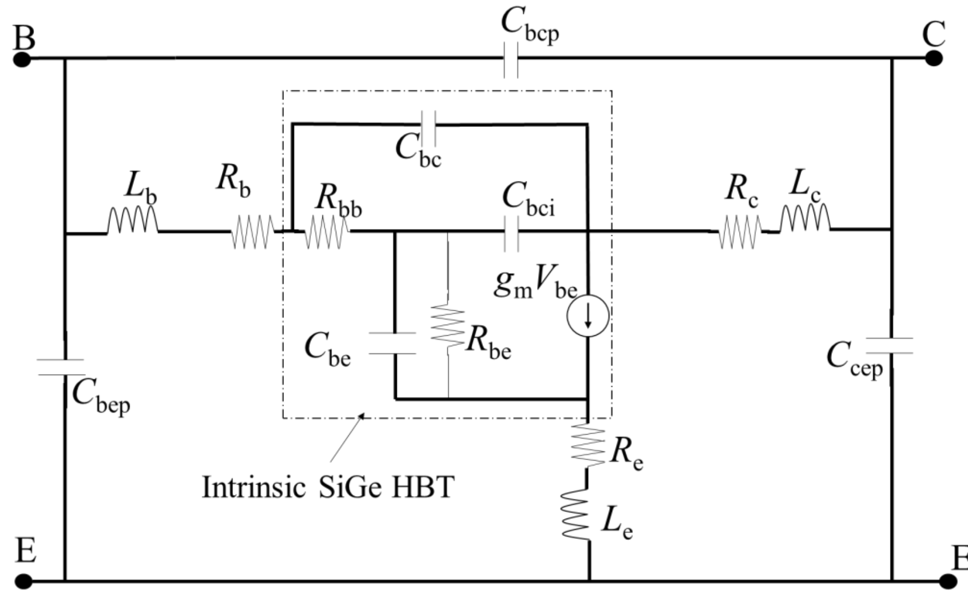

Figure 2.2: Small signal equivalent circuit model for SiGe HBT as proposed by [15]

An analytical method for robust extraction of the small signal equivalent circuit for SiGe HBTs operating at cryogenic temperatures is proposed in [16], which is shown in Figure 2.3. This model takes into account the parasitic effects from bond pads and feed lines. Small signal parameters are extracted from measured S -parameter in the frequency range of up to 22 GHz using a four step method [16]. In the first step, the measured S-parameters of the active transistor are converted to y-parameters. In the second step, the de-embedding process is performed to remove admittance parameters (Y_{p1}, Y_{p2}, and Y_{p3}), which are determined from measurements of an OPEN calibration standard. In the third step, the resulting y-parameters from the second step are transformed to z-parameters and then Z_{L1}, Z_{L2}, and Z_{L3}, which are determined from the measurements of a SHORT calibration standard (together with R_c and R_e) are removed. R_b is composed of two parts, namely the intrinsic part and the extrinsic part. The extrinsic part is removed together with Z_{L1} and the intrinsic part is determined from the resulting z-parameters.

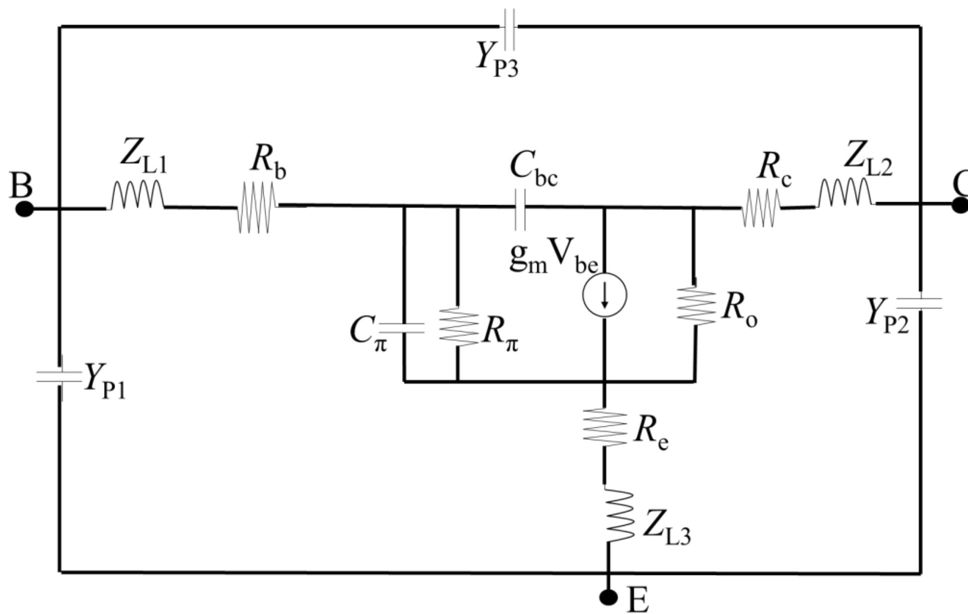

Figure 2.3: Small signal equivalent circuit model for SiGe HBT as proposed by [16]

In the fourth and final stage, the resulting z-parameters are transformed to y-parameters and all the small signal parameters for the intrinsic device are determined. As in the previous model, this one does not take into account the substrate network but differs from the previous one in its inclusion of an output resistance (R_o). Although the extraction of small signal parameters for this model is not complex, it has the disadvantage of having only been validated for the frequency range 2-22 GHz at a constant temperature of 77 K. The model may, therefore, not be reliable at mm-wave frequencies.

A small signal modelling method for SiGe HBTs based on the hybrid π model is reported in [17] and shown in Figure 2.4. The circuit of this small signal model is again divided into two parts, with one part consisting of bias dependent intrinsic element and the other one consisting of bias independent extrinsic elements. The circuit also comprises of the substrate network. To extract the small signal model parameters, S-parameters are measured for the device under common emitter configuration and another set under common collector configuration. SHORT and OPEN calibration standards are then used to de-embed the measured S-parameters to remove the effect of parasitics. This is followed by the removal of the substrate network. Some of the intrinsic small signal parameters are extracted from

the S-parameters obtained from the measurement under common emitter configuration, while other small signal parameters are extracted from S-parameters measured with the transistor connected in the common collector configuration. The disadvantage of this model is that it requires two sets of dies, one in the common emitter configuration and the other in the common collector configuration. Further, this model has only been verified up to 30 GHz.

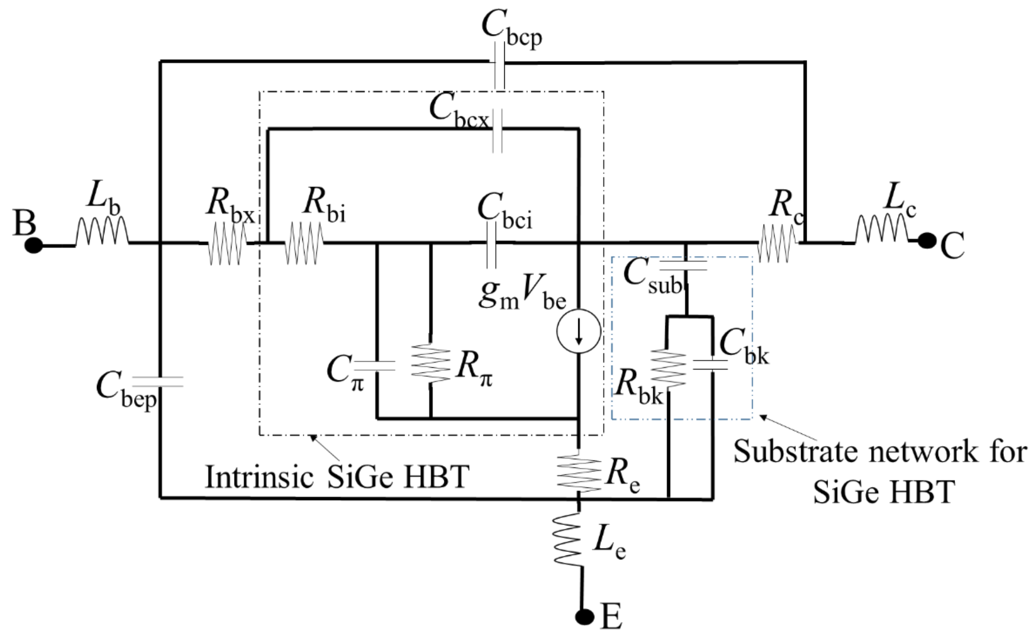

Figure 2.4: Small signal equivalent circuit model for SiGe HBT as proposed by [17]

In [18], a model based on the VBIC bipolar compact model is proposed. This model consists of the extrinsic part, intrinsic part, and substrate network, as shown in Figure 2.5. To extract small signal parameters, measured S-parameters are de-embedded using SHORT and OPEN calibration standards. The substrate network is extracted from S-parameters obtained from measurement with the transistor biased with a high base current and the collector biased with 0 voltage. This model has an advantage of having a simplified way of extracting the substrate network which consists of only two parameters. Its disadvantage is that it does not take into account inductance at the base, collector and emitter and as a result, it is not validated beyond 10.2 GHz. Because of the advantages of this model, a modified version of it to include inductances at the base, collector and emitter has been adopted for this study.

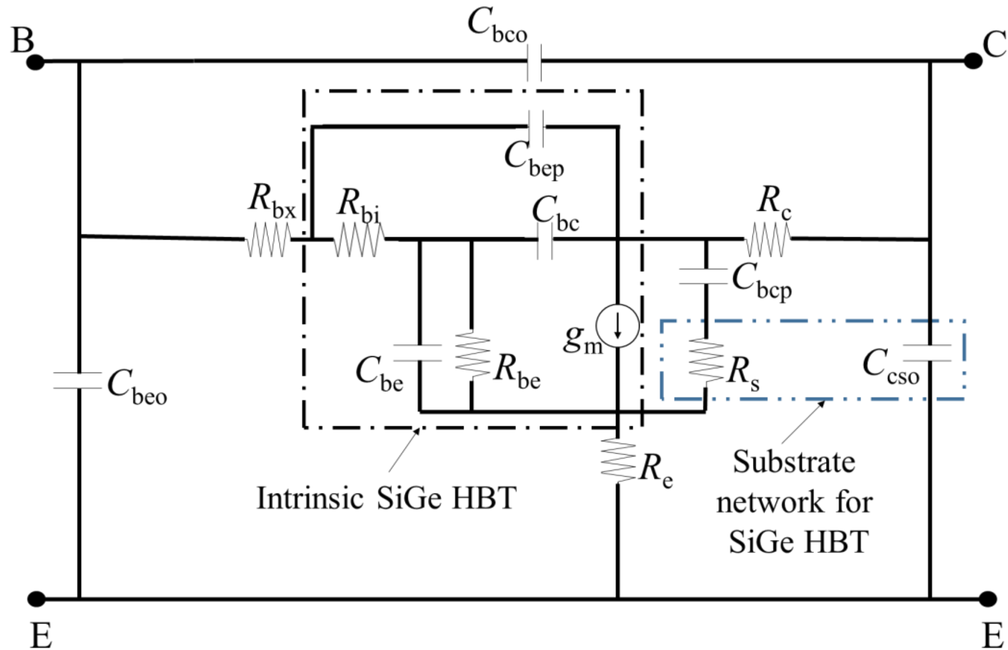

Figure 2.5: Small signal equivalent circuit model for SiGe HBT as proposed by [18]

2.2.2 Noise models for BJT and HBT devices

A physical noise model for SiGe HBTs at high frequencies, which predicts measured noise parameters up to 18 GHz, is presented in [14]. The advantage of this noise model is that it takes into account thermal noise from all the resistances in the circuit as well as the shot noise. Figure 2.6 shows this high frequency physical noise model. The disadvantage of this physical noise model is that it has only been validated up 18 GHz.

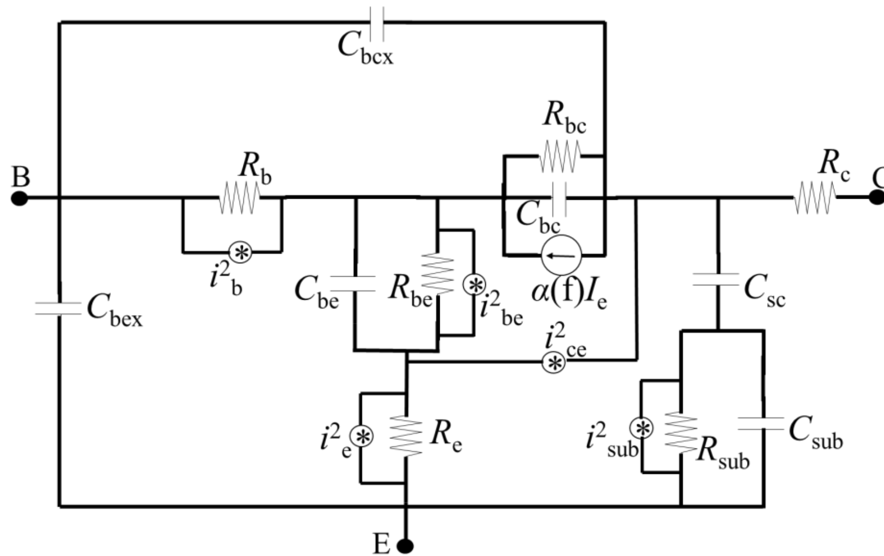

Figure 2.6: High frequency noise model with noise thermal and shot sources [14]

RF noise modelling in SiGe HBTs using quasi-static equivalent circuits, shown in Figure 2.7 is presented in [19]. Noise parameters for this noise model are calculated from S-parameters measured between 2 - 26 GHz using an 8510C VNA and compared to noise parameters measured using an ATN NP5 system from 2–25 GHz as a way of validating it. Again, is not evident that the model is reliable at mm-wave frequencies.

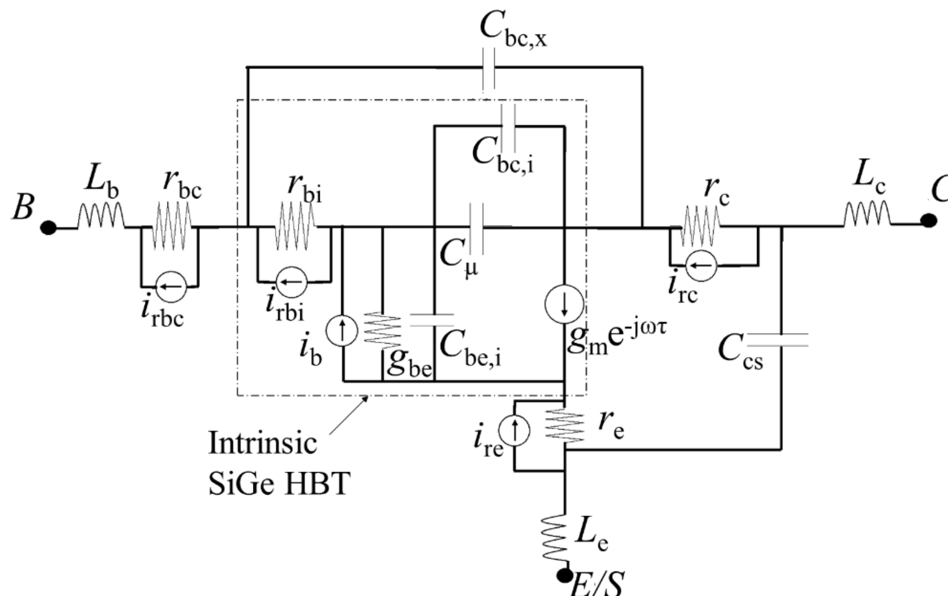

Figure 2.7: QS small-signal equivalent circuit of SiGe HBTs [19]

A noise model suitable for both BJTs and HBTs is presented in [20]. This model takes into account thermal noise at the base and shot noise due to the base current and the collector current. Figure 2.8 shows a complete description of major noise sources in a device, including the thermal noise and shot noise for this noise model. This model is adopted for this study.

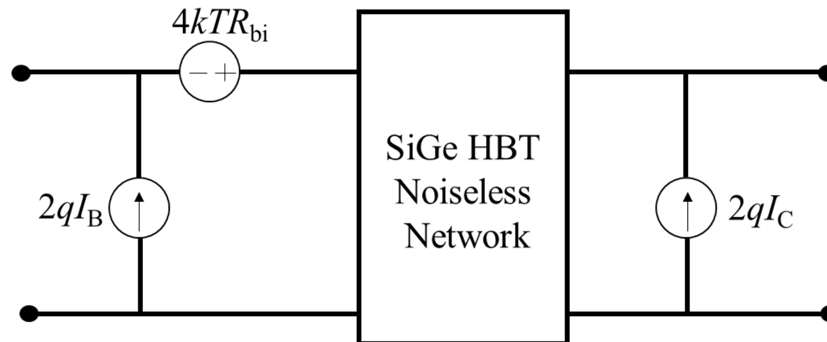

Figure 2.8: A complete description of major noise sources with thermal noise and shot noise [20].

2.2.3 Small signal models for bulk CMOS devices

A model and method for extraction of small signal transistor parameters in NMOS has been proposed in [21] and is shown in Figure 2.9.

In this model, the small signal parameters are characterised using S-parameters measured at four different bias points. The measured S-parameters at each of the four bias points are de-embedded to remove the effect of interconnect parasitic using OPEN and SHORT calibration standards. The de-embedded S-parameters are then transformed to y-parameters and all the small signal parameters including the substrate network but excluding the gate inductance are extracted. The gate inductance is then extracted using the best fit method. This model presents a simple method of extracting substrate parameters. The weakness, however, is on the determination of the gate inductance values, which requires the use of the iterative best fit method from measured results after all the other parameters are determined. This results in inaccurate values. The model has, however, been validated up to 110 GHz at all the four bias points.

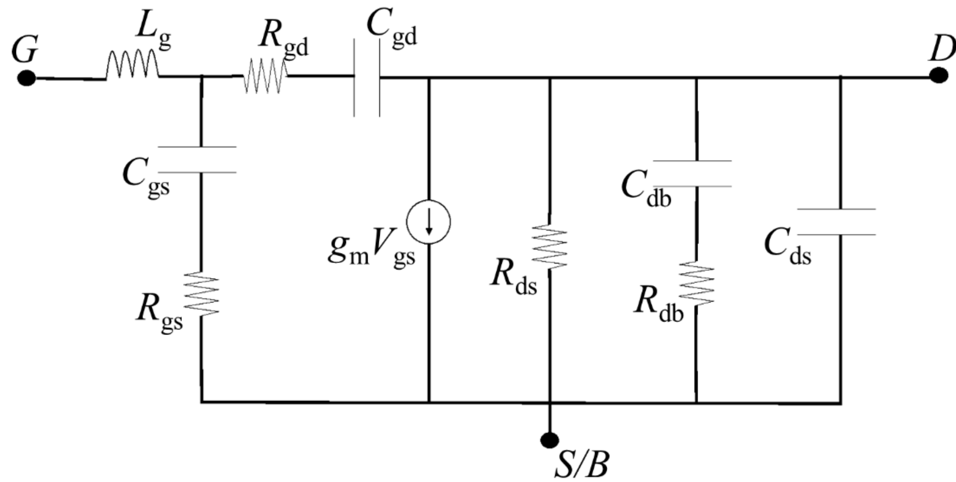

Figure 2.9: Small-signal equivalent circuit of the MOSFET used for mm-wave simulation [21]

Another model for the extraction of MOSFET small signal parameters is proposed in [22] with an accurate extraction method for the substrate network. This model has been validated up to 30 GHz. Figure 2.10 shows the representation of the model in its circuit format.

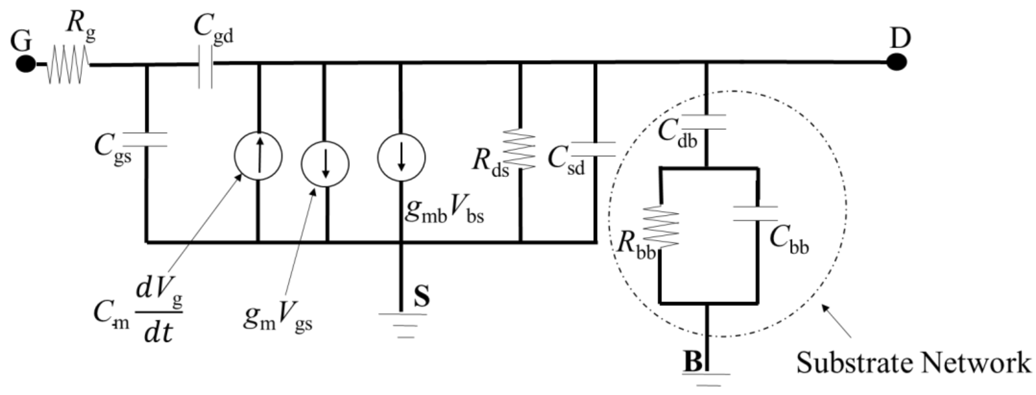

Figure 2.10: Simplified small-signal equivalent circuit of MOSFET with proposed drain-to-substrate network [22]

In this model, measured S-parameters are used to extract all the small signal parameters. The disadvantage of this model is that it does not take into account parasitics from the pads, feedlines and vias. Furthermore, this model is not a simple linear model; however, because of its advantage in the extraction of the substrate network, it has been adopted for this study with some modifications to make it a linear model.

2.3 IONIZING RADIATION IN SPACE

The presence of ionizing radiation in the space environment presents a serious challenge to the operation of electronic systems at a device, circuit and system level. In orbit around Earth, it originates from the interaction of the earth's magnetic field with the solar wind, which is produced by the sun. This radiation is predominantly due to charged particles, as opposed to X-rays and gamma rays [23]. The exact nature of the radiation environment that a semiconductor device in a spacecraft encounters in orbit is, however, dependent on many factors [20].

The potential spacecraft orbits are classified using the IEEE standard 1156.4 as LEO (describing space below the altitude of 10,000 km), medium earth orbit (MEO which is the environment in space whose altitude range from 10,000 km to 20,000 km), the geostationary orbit (GEO with altitude at 36,000 km) and the highly elliptical orbit (HEO) [20]. The diagram in Figure 2.11 shows the orbits.

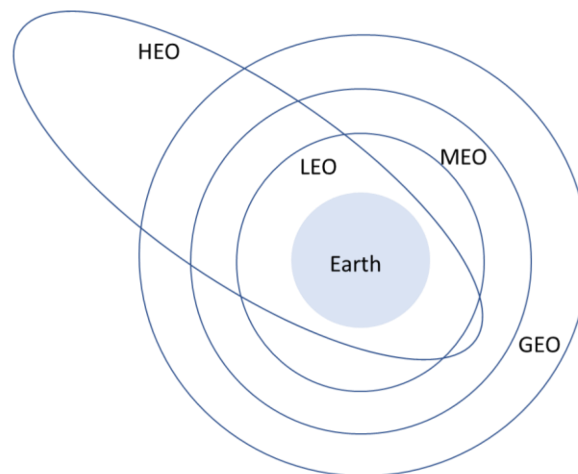

Figure 2.11: Location of orbits in space

Most spacecraft missions take place in LEOs, making radiation in this orbit the primary consideration in this study. LEOs have three principal components of primary ionizing radiation which include galactic cosmic rays (GCRs), earth radiation belts (ERBs), and solar particle events (SPEs) [23].

GCRs are charged particles originating beyond the solar system. Most GCR particles carry energy of around 0.3 GeV, but particles with an energy up to 10^{20} eV have been observed. They are comprised of 98% hadrons and 2% leptons. Hadrons are made up of 87% protons, 12% alpha particles and 1% heavy ions, while leptons are made up of electrons and positrons. GCRs tend to follow the lines of the geomagnetic field, which are parallel to the surface of the Earth near the equator. The geomagnetic field near the equator deflects most of the energetic particles, thereby directing them towards the north and south poles. It is for this reason that a LEO spacecraft receives more exposure to GCR when located near the poles than near the equator. GCRs are also attenuated by the solar wind. It therefore follows that GCR flux is high during solar minima when the solar wind has reduced intensity, and low when the solar wind has increased intensity. This depends on the particular phase of the 11-year solar cycle. Although the relative contribution from all sources is highly dependent on several factors including orbital inclination, altitude, spacecraft orientation, solar cycle and temporal variations in the geomagnetic field, GCRs are however more dominant for high inclination orbits [24].

The earth's magnetic field can trap particles, thereby generating intense regions of protons and electrons known as the Van Allen Belts or ERBs. ERBs form a toroidal structure with electrons being confined to two high intensity toroids. The first one which extends a distance of 2.4 times the radius of the Earth (characterised by energy levels below 5 MeV) and the second band extends a distance of between 2.8 and 12 times the radius of the Earth. Protons are confined to a single toroid, with intensity decreasing as a function of distance from Earth. Their energy distribution peaks between 150 MeV and 250 MeV. Electronics in satellites are greatly influenced by these proton and electron belts. ERBs are primarily comprised of electrons with energy less than 6 MeV and protons with energy less than 250 MeV, and are more of a concern for low inclination, high altitude orbits [24].

Two types of SPEs exist, namely those emitted by the sun during coronal mass ejections (CMEs) and those formed by solar flares. The first type of SPE is characterised by protons with a lifespan in the order of days. These have a total fluence of 10^9 cm^{-2} and can spread over a broad angle of 60° to 180°. They are mostly composed of low energy protons and

electrons with a few higher energy protons and some heavy ions. The second type of SPE is associated with solar flares characterised by fluxes of electrons having a short lifespan (on the order of hours). The SPEs associated with solar flares have a total fluence of between 10^7 cm^{-2} and 10^8 cm^{-2} restricted to an angle of between 30° and 45° in solar longitude [24].

The relative size, energy and charge distribution of each component (GCRs, ERBs and SPEs) in LEO, however, are dependent on a large number of parameters. These include the altitude and inclination of the spacecraft's orbit, the orientation of the spacecraft relative to the Earth and Sun and the particular phase of the 11-year solar cycle. It therefore follows that, depending on these conditions, a spacecraft could be exposed to a combination of any of the three components and hence more electrons or protons. Both protons and electrons cause DD and TID, but the exact nature and ratio depends on the particle as well as on its energy. In order to ensure repeatability, and due to ease of use, in this study, a Sr-90 source was used to study the effects of electron radiation.

2.4 RADIATION EFFECT IN SiGe HBT

To best understand the effect of radiation on SiGe HBT, the operating principles of a SiGe HBT need to be understood from the energy band engineering point of view, as is reported in [3]. An ideal, graded-base SiGe HBT with constant doping in the emitter, base, and collector regions was examined. In SiGe HBTs, the Ge content in the base is linearly graded from 0% to a maximum value of Ge. The content is minimal near the metallurgical emitter-base (EB) junction and maximum near the metallurgical collector-base (CB) junction and thereafter rapidly drops to 0% of Ge. The reason for introducing Ge into the base region of SiGe is the reduction of the potential barrier to injection of electrons from the emitter into the base. The implication is that more electron injection would be obtained for the same applied base emitter voltage (V_{BE}) which translates into a higher collector current and, hence, higher current gain for the same base current. The presence of Ge in the CB junction of SiGe HBT further positively influences the output conductance [5].

SiGe HBTs are also made up of a heavily doped, thin base of SiGe alloy, a thin base emitter (EB) spacer oxide, a thin shallow trench isolation (STI) in the collector base junction (which

is away from the transport path of the transistor) and deep trench isolation (DTI) [5]. The implication of a heavily doped thin base is an increased tolerance to TID and DD by SiGe HBT, as explained in [25]. This also explains why reduced size scaling increases the resistance against radiation damage. However, despite this tolerance to TID and DD, SiGe HBTs are expected to fail once subjected to a long duration of ionizing radiation exposure leading to a high dose, as observed from past research studies.

2.4.1 Radiation effect on DC performance of SiGe HBTs

The effect of ionizing radiation on the DC performance of SiGe HBTs was investigated and covered in [5]. It was found that ionizing radiation causes atomic displacement in the bulk of the SiGe HBT leading to an increase in the forward mode base current, which is attributed to the generation/recombination (G/R) trap centres at the base emitter (EB) junction. The implication of this increase in the forward mode base current is a degradation in the forward current gain (β) and a shift in the peak β.

2.4.2 Radiation effect on the RF and noise performance of SiGe HBTs

The effect of ionizing radiation on RF and noise performance in SiGe HBTs was extensively investigated in numerous studies including in [5].

In the study carried out in [26], S-parameters were measured up to 48 GHz over a wide span of bias currents at fixed collector base voltage and de-embedded in order to calculate both the small signal current gain and the maximum unilateral gain before and after radiation. The f_T as well as the maximum oscillation frequency (f_{max}) were determined by extrapolating a -20 dB/decade slope from the measured values at 40 GHz. This was done before and after radiation, indicating some negligible changes in f_T and f_{max}. The study, however, did not investigate the effect of radiation on individual small signal parameters, making it impossible to determine whether the input or output matching networks would need to be significantly altered due to radiation degradation over time.

The effect of proton irradiation on RF performance on SiGe HBTs was investigated and reported in [27]. In the study, S-parameters were measured and the minimum noise figure (NF_{min}), f_T, f_{max}, and the total emitter and base resistance (r_{BE}) were extracted before and after proton radiation. Some minimal increase in NF_{min} and base r_{BE}, and minimal decrease in f_T and f_{max} at extreme proton fluences, were observed, confirming the resilience of SiGe HBTs to radiation damage. The study, however, only investigated the effect of proton radiation on cumulative parameters, and did not investigate the effect of proton radiation on individual small signal parameters for a complete small signal model of a SiGe HBTs.

Radiation effects on RF and noise performance of SiGe HBTs were also investigated in [5]. In their research work, devices from the first generation, second generation, third generation and fourth generation SiGe HBT technologies were investigated. The impact of radiation was assessed by first measuring S-parameters up to 40 GHz before and after radiation. The NF_{min} for first generation SiGe HBTs and f_T for devices from each of the four technologies were extracted from the measured S-parameters. A slight increase in NF_{min} and decrease in f_T were observed after radiation. This confirmed previous research studies suggesting that SiGe HBTs was tolerant to ionizing radiation damage. However, as with other studies, the investigation in [5] did not establish sufficient data to constitute a complete small signal model of a SiGe HBTs after radiation.

2.5 RADIATION EFFECTS IN BULK CMOS DEVICES

It is evident from a review of the relevant literature that ionizing radiation causes significant performance degradation in bulk CMOS devices [18].

2.5.1 Radiation effect on DC performance of bulk CMOS devices

In bulk CMOS devices, ionizing radiation is reported to cause a buildup of trapped charges at the silicon – silicon dioxide interface, thereby distorting the electric field. The distortion of the electric field can lead to an increase in the offset voltage, thereby increasing the gate bias voltage required to induce a drain–source conducting channel at the silicon surface.

This increase in the offset voltage effectively causes an increase in the threshold voltage of the device [28].

Ionizing radiation also causes a reduction in g_m of the Si CMOS devices [29]. There are two ways in which trapped charges caused by ionizing radiation at the conducting channel interface of the Si CMOS can reduce g_m. Firstly, the carrier mobility in the channel can be decreased by the presence of trapped charges, and secondly, trapped charges can cause an increase in the channel resistivity, thereby decreasing g_m. The trapped charges also create new interface states at the silicon-silicon dioxide interface that reduces carrier lifetime, thereby increasing leakage current at the junction. Furthermore, ionizing radiation causes an increase in the gate leakage and off state leakage currents [29].

2.5.2 Radiation effect on RF performance of bulk CMOS devices

Studies have indicated the negative effect of ionizing radiation on the RF performance of bulk CMOS devices [29]. Radiation induced damage in bulk CMOS devices cause a reduction in the magnitude of S_{21}. Furthermore, radiation induced damage causes a decrease in f_T of the device. This decrease in f_T is as a result of the radiation induced decrease in g_m, as well as increase in C_{gd} and C_{gs}, since f_T is directly proportional to g_m and inversely proportional to C_{gs} and C_{gd} [29].

$$f_T = \frac{g_m}{2\pi\left(C_{gs} + C_{gd}\right)} \tag{2.1}$$

Whilst previous literature studies have covered the effect of radiation on the RF performance in a general sense [6], the effect of ionizing radiation on small signal parameters for a complete equivalent circuit model of a bulk CMOS device has not been covered. A significant research gap has been left in bulk CMOS devices for predicting their performance in newer generations of transistors under ionizing radiation.

2.6 CHAPTER SUMMARY

In this chapter, small signal models and noise models for both BJT and HBT devices were discussed in detail. The weaknesses and strengths of the models were pointed out and justification for adopting the chosen model provided. The chapter also presented small signal models for bulk CMOS devices and adopted one of them for use in this study. Ionizing radiation in space was discussed, in which a justification for the choice of an electron source of radiation was given. The chapter went on to present the effect of TID damage to transistors. The effect of radiation on the DC performance on SiGe HBT was then presented, in which it was observed from previous research studies that radiation increased the forward base current, consequently degrading β of the device. A presentation on the effects of radiation on RF performance followed, where it was revealed that radiation caused a decrease in the key RF parameters f_T and f_{max} and an increase in NF_{min}. The chapter went on to present the effects of radiation on the DC performance of bulk CMOS devices and concluded with a presentation on the effect of radiation on RF performance of bulk CMOS devices.

Previous studies did not establish the effect of radiation on the individual small signal parameters in both SiGe HBTs and bulk CMOS devices. In this study, the effect of radiation on the individual small signal parameters will be investigated.

CHAPTER 3 METHODOLOGY

The chapter will introduce the two semiconductor process technologies used for prototyping experimental transistors in this study, namely the 8HP 0.13µm SiGe BiCMOS process from GlobalFoundries US and the C35B4C3 0.35 µm CMOS process from austriamicrosystems (ams AG). This is followed by a discussion on how the transistor models and extraction procedures were selected. The procedure which was followed to generate layouts for the devices and the calibration standards for post-processing will be discussed. The simulation setup, radiation experiment setup, and S-parameter measurement setup is presented next. The chapter then gives a detailed description of the model extraction procedure for SiGe HBTs, a detailed description of the extraction of noise model parameters for SiGe HBTs, and a detailed explanation of model extraction for bulk CMOS devices. The noise model for bulk CMOS devices requires measurements not generated in this study, and will therefore not be covered.

3.1 DESIGN OF THE 0.13 µm SiGe HBT AND CALIBRATION STANDARDS

The 8HP process has several back end of line (BEOL) metallurgy options, of which the 7 metal layer option is selected for this study. It consists of M1, M2, M3, and M4 made of thin copper, MQ made of thick copper, and LY and AM made of thick aluminium, as shown in Figure 3.1.

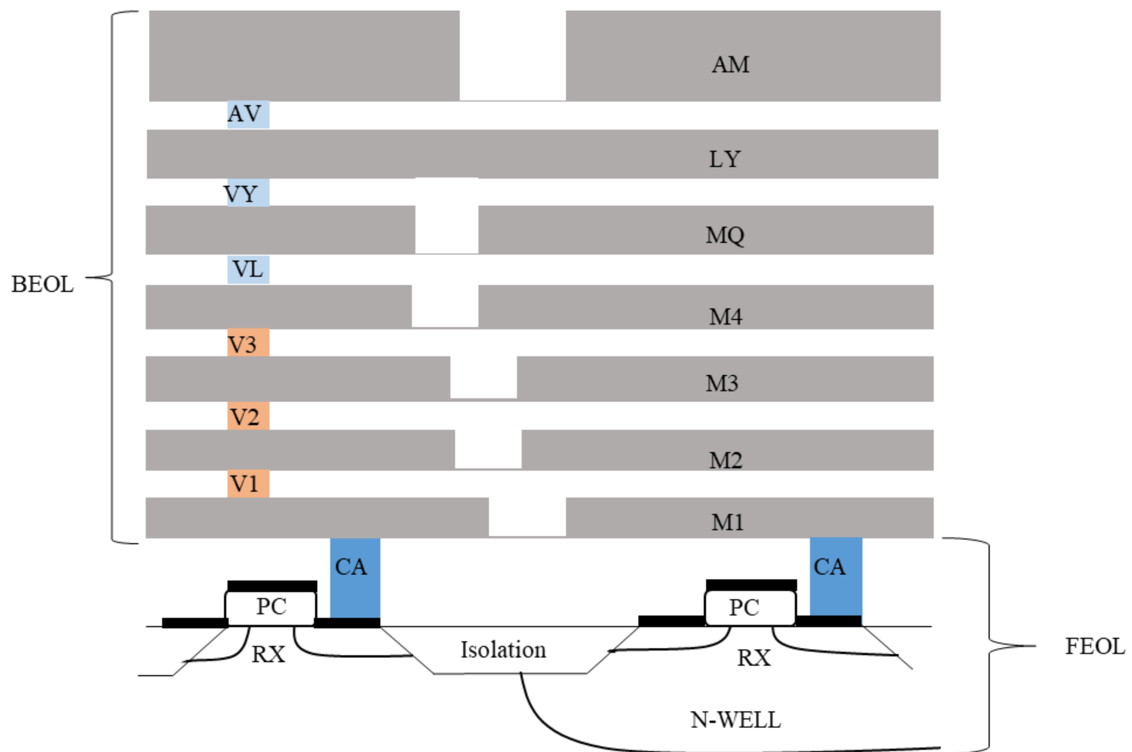

Figure 3.1: The 7 metal BEOL and FEOL stacked in 8HP

The technology also has a PDK library with several pcells for various devices. A pcell is a scalable model of the device including parasitics. Parasitics of the interconnecting metals leading up to the device are, however, not part of the pcell. Among the pcells in the PDK library is the SiGe HBT, of which the interconnecting contacts are located at M1 layer. The pcell has two layout options, namely the collector-base-emitter-base-collector (cbebc) configuration and the collector-base-emitter (cbe) configuration. Routing from M1 to the contact pads is accomplished through wiring on the available metal layers interconnected by vias (for which models are also included in the PDK).

The kit also offers two types of SiGe HBTs namely the non-RF high breakdown and the RF high f_T options. The high breakdown SiGe HBT can be biased with a high voltage for greater power output, while the high f_T device has more limited power output but provides faster performance. The high breakdown device can only be prototyped in the cbebc configuration while the high f_T device has the option of both the cbebc and cbe configurations.

For maximum f_T, the SiGe HBT with emitter length of 0.12 µm and width of 4.5 µm was used, as this size compared well with the dimensions of devices used in previous studies [16]. The SiGe HBT configured in cbebc, and setup in common emitter configuration, with the substrate tied to the emitter and grounded. The simulation circuit, comprising of two 50 Ω impedance ports at the input and at the output, and bias tees with capacitance and inductance values of 1 µF and 1 µH respectively was setup, in which the base and collector voltages were varied to determine the bias voltages for maximum f_T. From simulations, the bias voltage requirements for maximum f_T were determined to be 0.88 V at the base and 1.1 V at the collector, at which the device drew collector a current of 5.473 mA. Once the bias conditions necessary for maximum f_T were ascertained, simulations were carried out with the circuit biased at the determined base and collector voltages as shown in Figure 3.2, to determine the linear dynamic range at both the input and output. The 1 dB input compression point was found to be -2.8622 dBm. Simulations of S-parameters and noise figure were then done.

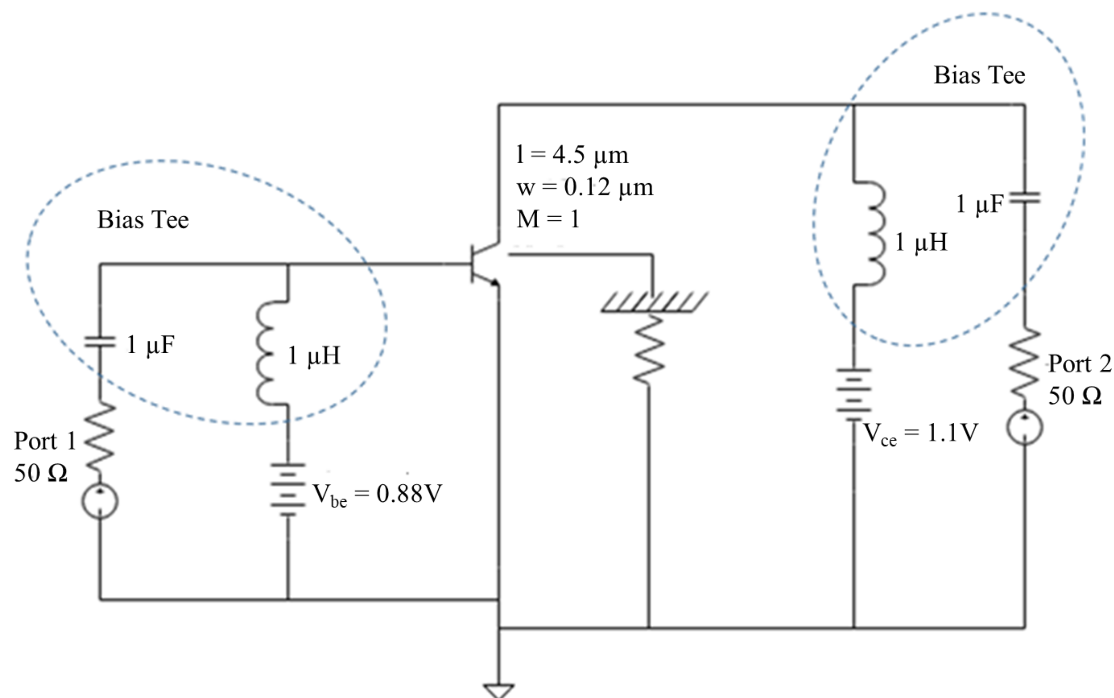

Figure 3.2: Simulation circuit setup to test the linear dynamic range at input and output

Once simulations were completed, the SiGe HBT was drawn in Cadence Virtuoso layout using the pcell. The two collectors of the pcell in the cbebc configuration were connected together using the M1 to M2 vias and a bridge on the M2 layer. The two bases were connected on the left hand side on layer M1, with the emitter routed out from M1 at the right hand side. The short copper leads at M1 were routed to the upper aluminium AM layer using via stacks, as shown in Figure 3.3.

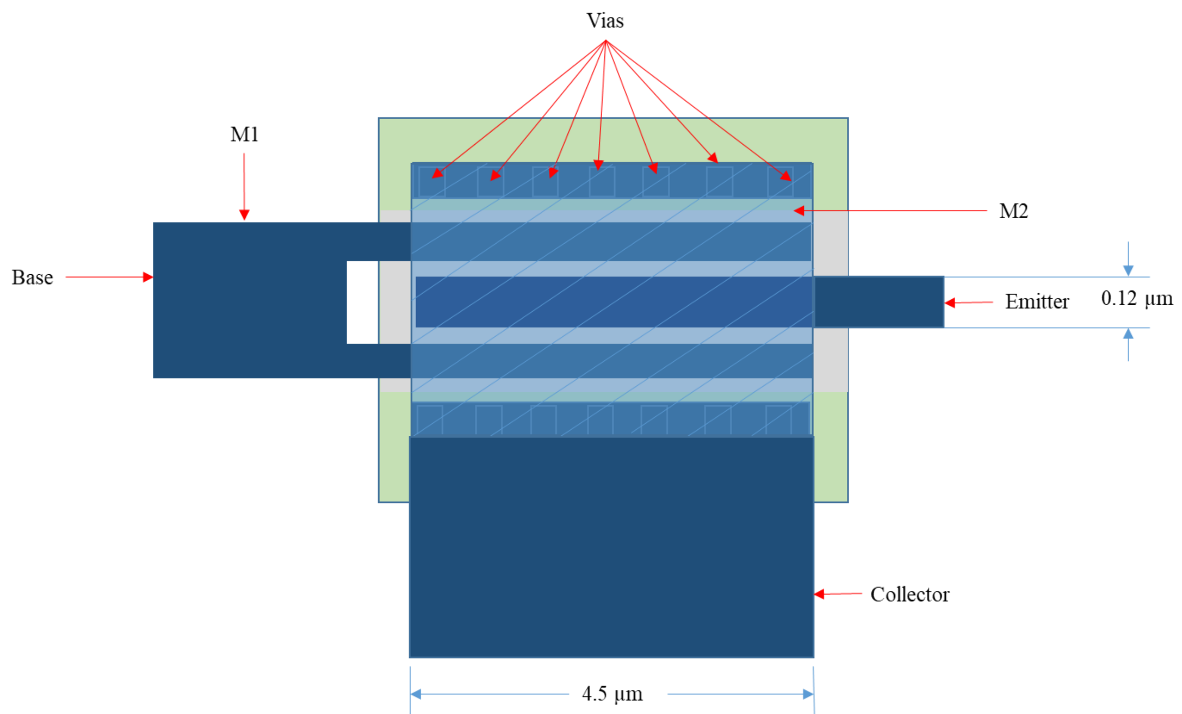

Figure 3.3: Layout of SiGe HBT

The short copper leads for the base on the left and the collector on the right were routed to the respective via stacks connecting M1 to AM. At the AM layer, via stacks on the left were routed to the signal probe pad to connect the base, while via stacks on the right were routed to the other signal probe pad to connect the collector. To connect the emitter to the ground probe pad, the short M1 copper lead was connected to a via stack and at AM layer, the via stack was connected to the ground probe pad using aluminium wiring. Design rule checking (DRC) tests were then completed to check for any design rule violations in the layout. The artwork was found to satisfy all the rules and a GDSII file was generated for consideration

in a larger prototyping chip. The layout of the SiGe HBT connected to the probe pads is shown in Figure 3.4.

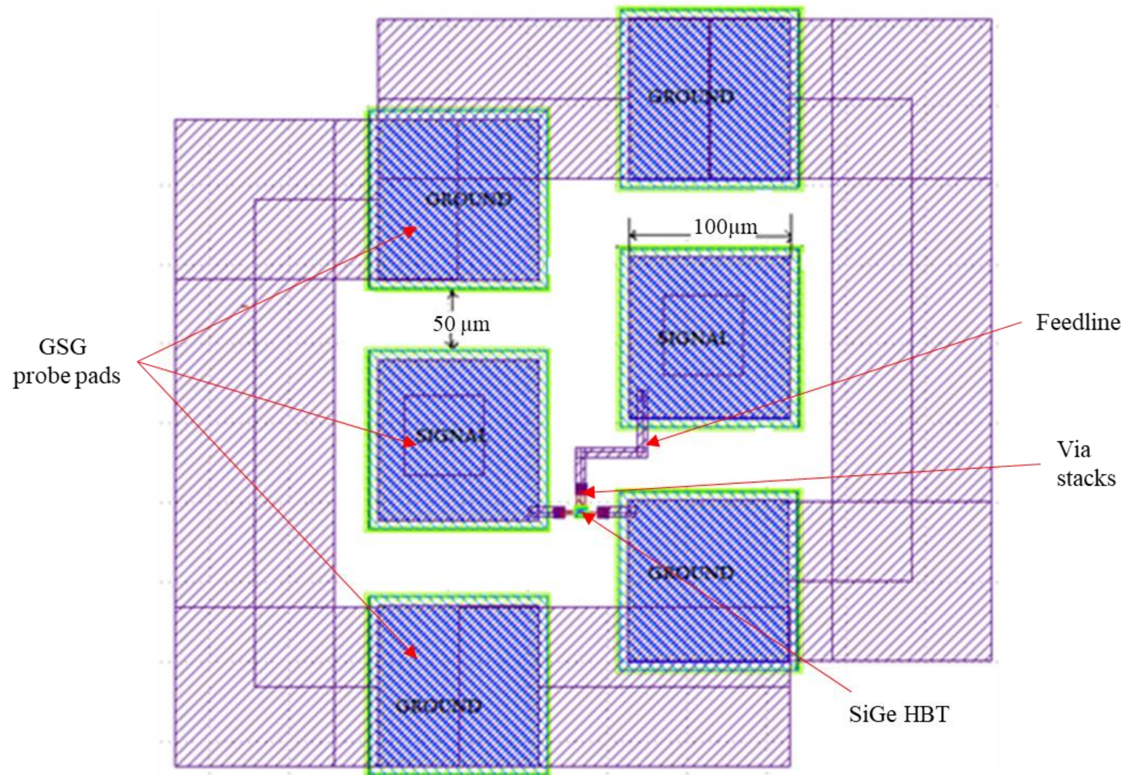

Figure 3.4: Layout of SiGe HBT with probe pads connected

Calibration standards were also designed to de-embed the transistor up to the M1 pcell boundary. The OPEN calibration standard had the dummy collector terminals connected to each other using the M1 and M2 vias while the dummy base terminals were connected to each other on the left side to allow for connection to the dummy emitter metal on the right. The SHORT calibration standard had all the dummy terminals connected together so as to create a short circuit. Figure 3.5 and Figure 3.6 show the OPEN and SHORT calibration standards respectively.

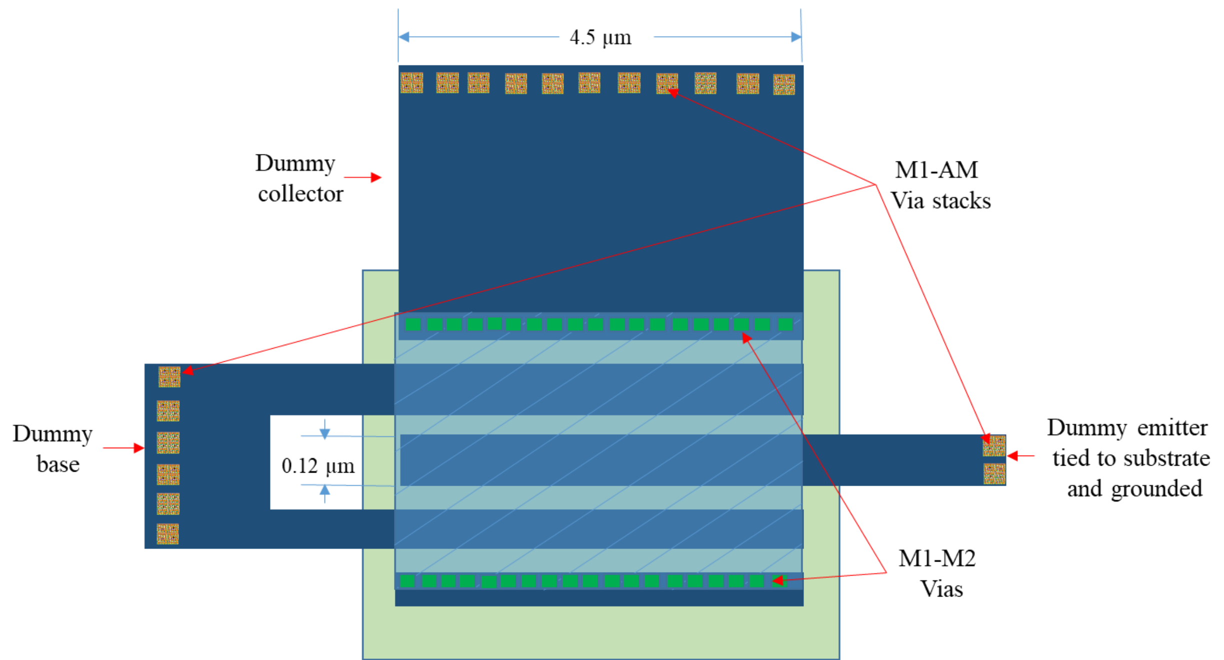

Figure 3.5: Layout for the OPEN calibration standard with collector terminals connected together using M1/M2 via stacks

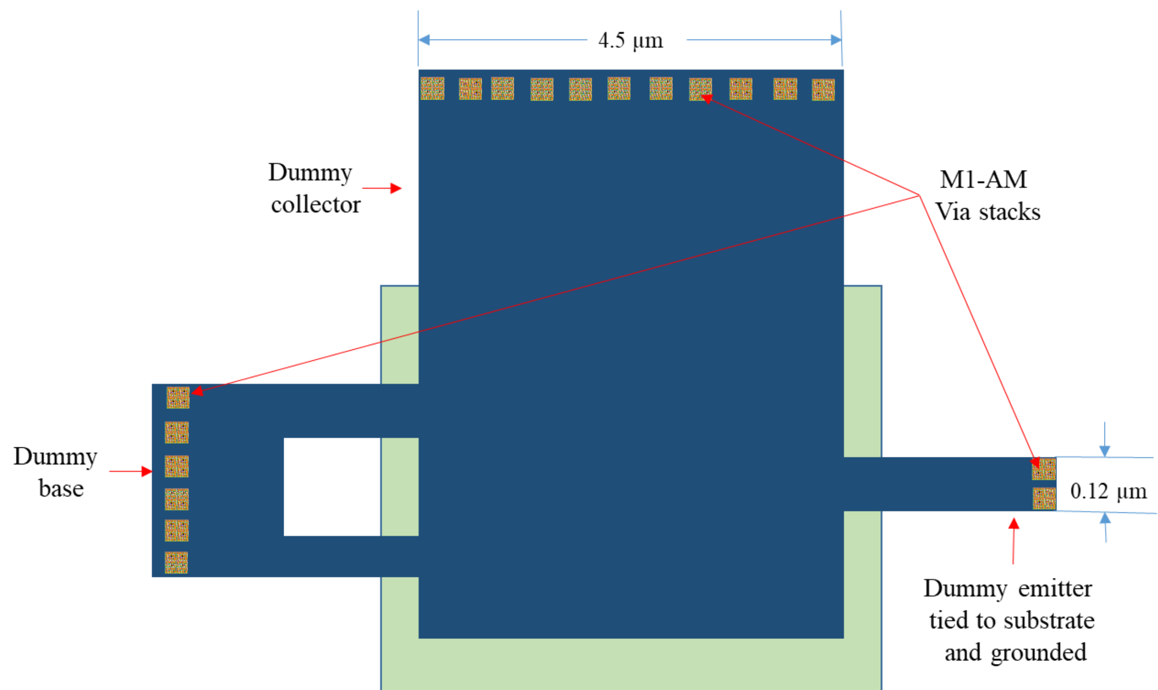

Figure 3.6: Layout for the SHORT calibration standard with all the terminals connected together

The SiGe HBT, SHORT and OPEN calibration standards are shown on the multi-project die in Figure 3.7.

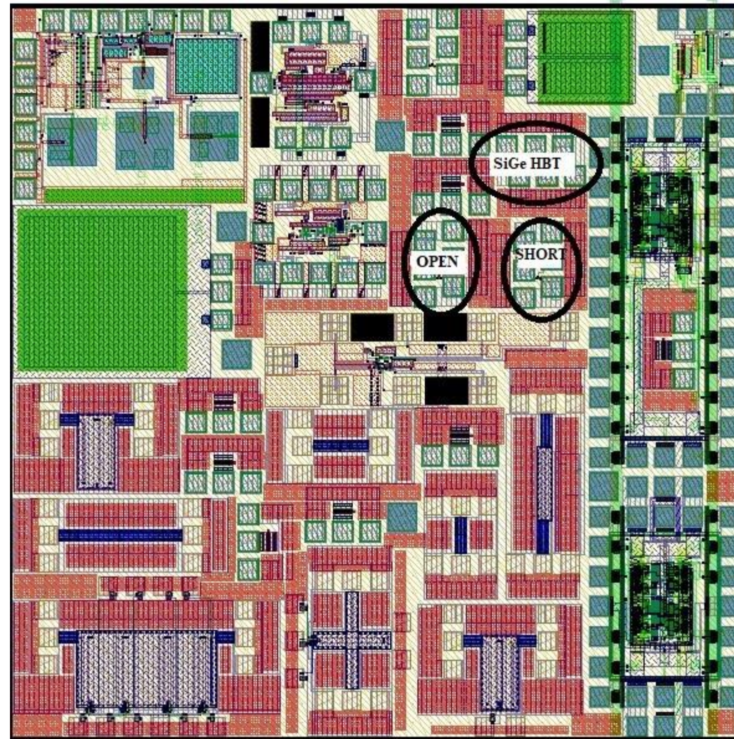

Figure 3.7: Location of the SiGe HBT and the OPEN and SHORT on wafer calibration standards on die

3.2 DESIGN OF THE 0.35 µm CMOS TRANSISTORS AND CALIBRATION STANDARDS

The C35 0.35µm CMOS process by ams AG has several metallization options. The four metal layer stack is used in this study, which consists of two polysilicon layers and four thin copper layers, as shown in Figure 3.8.

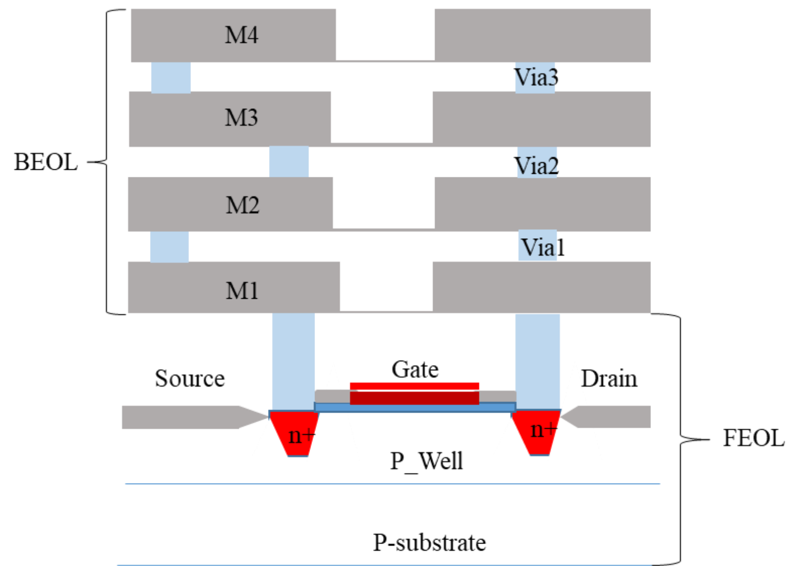

Figure 3.8: Layers of C35 process stack up

The PDK features a wide range of pcells for active and passive components. Among these is the NMOSRF pcell which contains RF-optimised scalable layout and compact models of NMOS devices. The pcell has an option of 5 μm or 10 μm for the width of a single gate finger, with the option for multi-finger layout. Figure 3.9 and Figure 3.10 show the NMOS device with a single finger and multi-finger gate respectively.

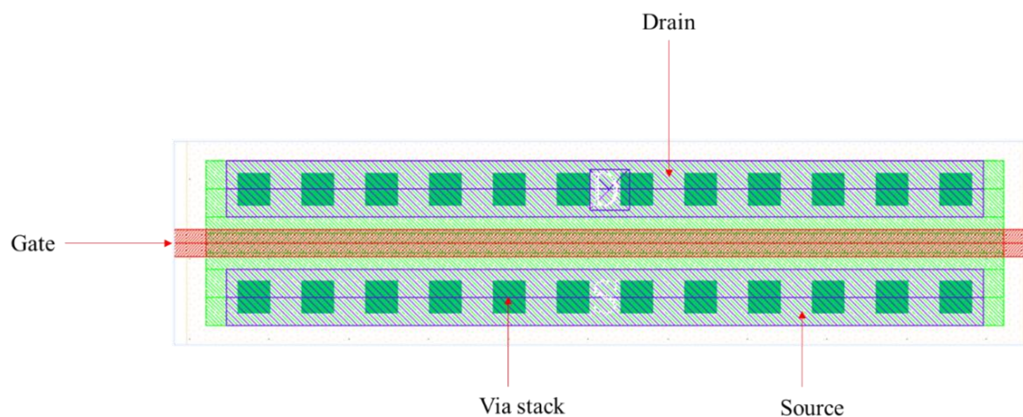

Figure 3.9: Single finger NMOS device

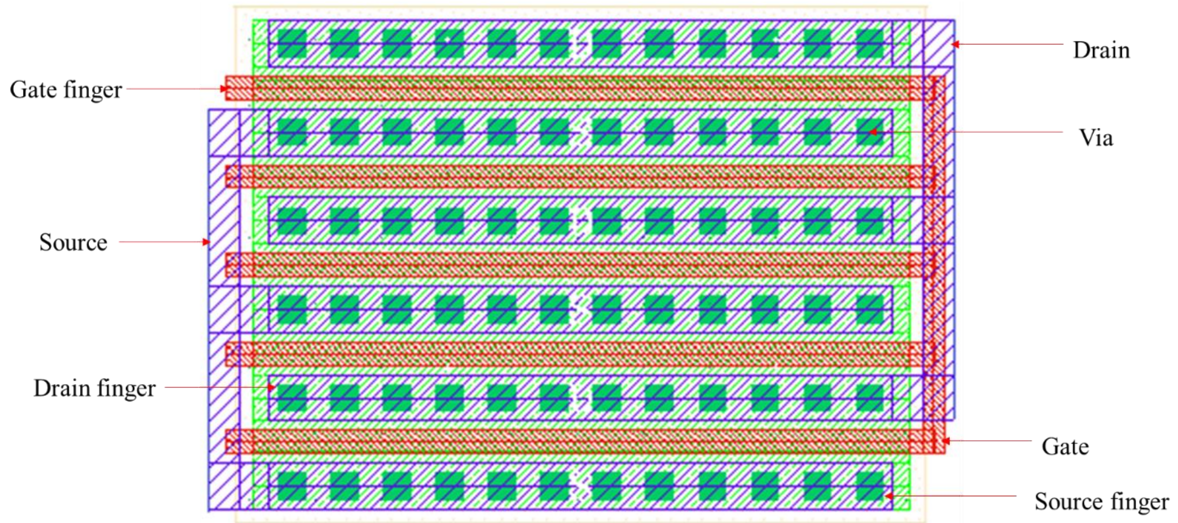

Figure 3.10: Multi finger NMOS device

Four transistors were chosen for this study. Two had a gate width of 5 µm and another two, a gate width of 10 µm. One of the two transistors with a gate width of 5 µm had five fingers while the other one was drawn with a single finger. Similarly, one of transistors with a gate width of 10 µm had five fingers while the other one had a single finger. Simulations were done in Spectre RF to determine the bias conditions for maximum f_T and the resulting linear dynamic range for each of the four transistors. The determined biasing conditions, input power 1 dB compression point are shown in Table 3.1.

Table 3.1: Biasing voltages and input power compression point for various transistors

Total Gate width	Gate- Source Voltage	Drain- Source Voltage	Input Compression Power
5	2.08 V	3.5 V	10.01 dBm
10	2.03 V	3.5 V	10.06 dBm
25	2.10 V	3.5 V	11.05 dBm
50	2.03 V	3.5 V	12.28 dBm

S-parameter simulations were carried out with the input and output driven by 50 Ω impedance ports via *analoglib* bias tee connection of capacitance and inductance values of

1 µF and 1 µH, respectively. Once the simulations were done, the four transistors were drawn in common source configuration in layout. The probe pads, having a dimension of 100 µm by 100 µm and 150 µm pitch, were drawn on the top M4 metal layer. They were connected to the transistor using 50 Ω impedance microstrip lines, the width of which was determined to be 8 µm using EM simulation in CST Microwave studio. The signal line of the microstrip was connected to the polysilicon using a via stack between the polysilicon and M4 at the gate side and a via stack between M4 and M1 for the source and drain, as shown in Figure 3.11. In order to satisfy metal density rules, the ground plane was perforated with square holes measuring 5 µm by 5 µm. These holes were, however, placed not to overlap with the signal trace, to minimize the influence on the line's propagation characteristics.

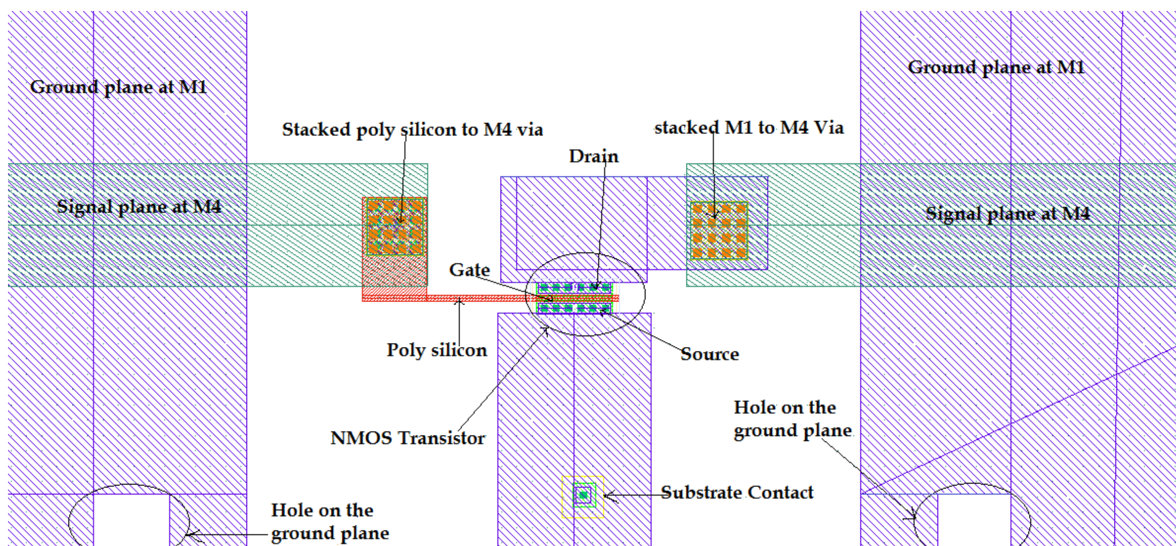

Figure 3.11: Microstrip connection to the NMOS transistor

The four NMOS transistors were fabricated to share the ground pads in a GSGSGSGSG configuration, both at the gate input and the drain output side, along with the THRU and REFLECT calibration standards. The LINE calibration standard, with an electrical length of 60° at 50 GHz and a physical length of 1032 µm, was fabricated separately with its own signal and ground pads. These calibration standards were designed to de-embed the transistors up to M4 level by removing the pads and the feedlines at M4 layer. The calibration standards were, however, not designed to remove the metallization of the M1-M4 via stacks and the feedlines at M1 layer.

3.3 IRRADIATION OF DEVICES

This section will provide some background on radiation test procedures, before continuing to present the radiation experiment conducted in this study.

3.3.1 Radiation experiment methods and procedures

Various radiation standards have been developed to ensure that radiation tests follow best practices both to ensure safety, produce repeatable results, and reduce and bound systematic and random errors [30].

Key radiation test standards are presented in [30]. These include the US DoD MIL-STD-750 and MIL-STD-883 radiation test standards, as well as the European Space Agency - European Space Components Coordination (ESA-ESCC) 22900 radiation test standard.

The MIL-STD-750 [31] includes two test methods which are of interest. These are TM 1017, a neutron irradiation test, and TM 1019, a steady state total dose irradiation procedure. TM 1017 is performed with a radiation source used in a TRIGA Reactor or Fast Burst Reactor while TM 1019 uses a Cobalt 60 gamma ray radiation source.

The MIL-STD-883 radiation test method standard was specifically developed for microcircuits [31]. This radiation test method standard like the MIL-STD-750, has different test areas. The test areas which are of interest are TM 1017 for neutron radiation and TM 1019, stipulating the procedure for ionizing radiation total dose test. The radiation test method used for TM 1017 and TM 1019 in MIL-STD-883 is similar to that used for the same test methods in MIL-STD-750.

The ESCC 22900 radiation test method was developed for steady-state irradiation testing of integrated circuits and discrete semiconductors necessary for space applications. In this radiation test standard, two radiation sources are applicable, namely the Cobalt 60 gamma ray radiation source and the electron radiation source. The electron radiation source required

in this radiation test standard is a steady state electron source with energy equal to or greater than 1 MeV. The radiation test standard further stipulates that the electron beam must be monitored by a Faraday cup and current integrator, although it gives an allowance to use other methods to monitor the electron beam. The dose profile of the beam is required to be uniform within ±10% for a separation distance between the source and the DUT of at least 24 mm or 5 times the diagonal of the DUT, whichever is greater. Two windows are specified for the dose rates for this radiation test standard. The first window, known as the standard rate with dose rate in the range of 0.36 to 180 krad (Si)/hour while the second window is designated as the slow rate with dose rate in the range of 36 to 360 rad (Si)/hour. There are, furthermore, two ways in which experiments can be done under this test standard, namely the in-situ testing or remote testing. In-situ testing requires electrical characterization to be done while the DUT is under radiation exposure, while remote testing requires electrical measurements to be done away from the radiation site. It is further specified that for remote testing, measurements must be done within one hour of removing the DUT from the radiation exposure. If re-exposure of the same device has to continue, it must be done within two hours after removing it from radiation exposure [32].

3.3.2 Radiation experiment setup

In this study, a test method similar to the standard window for ESCC 22900 radiation test method was adopted. In this method, electrons from a Strontium 90 (Sr-90) lab source was adopted. This deviates from ESCC 22900 as the prescribed method requires a steady electron source, while Sr-90 is not a steady source. It does, however, produce electrons with energy ranging from 0 to just over 2 MeV. The radiation is emitted in two peaks, one with energy ranging from 0 to about 500 keV (average 200 keV) due to Sr-90 and the second with energy ranging from 0 to 2.2 MeV (average 940 keV) due to the daughter Y-90 decaying [33]. Since the stopping power of silicon for electrons varies by less than 50% over the range 100 eV to 40 MeV [34], the results are expected to agree qualitatively (if not quantitatively) to those produced by ESCC 22900.

The separation distance between the radiation source and the DUT was set such that the radiation dose rate was 32 krad (Si)/hr to satisfy the requirements for the standard window of ESCC 22900. The radiation experiment in this study was planned as a remote testing experiment in which radiation exposure was done in the separate lab from where linear measurement for S-parameters were carried out. The transistors were irradiated with floating terminals and linear measurements were completed within an hour from the time of removing them from the radiation source and returned to the source environment within an hour for continued irradiation. The setup of the radiation experiment is shown in Figure 3.12.

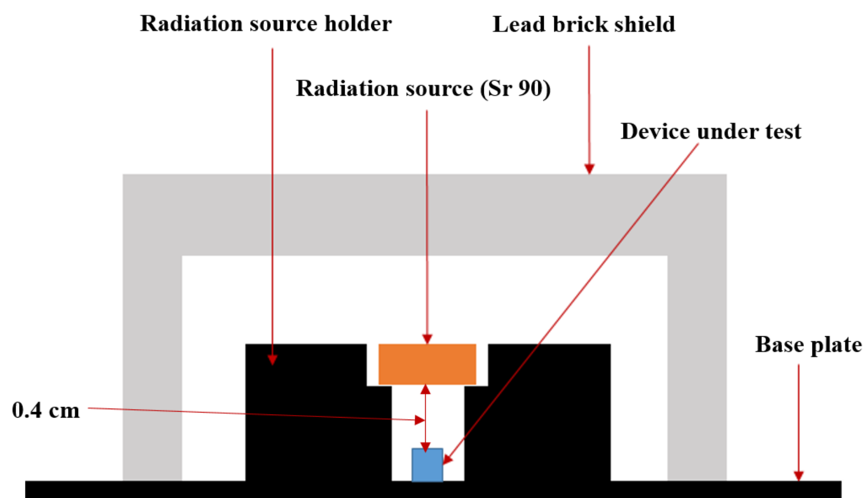

Figure 3.12 Setup for radiation experiment

3.3.3 Fluence rate calculation

The radiation source used in this experiment was the Sr-90 beta source US model SIF D1, ID # AC-2957, shown in Figure 3.13.

Figure: 3.13: Sr-90 beta source US model SIF D1, ID # AC-2957

This radiation source has a nominal radiation activity (B) of 3.7 GBq at date of 30 April 2013, with Sr-90 evenly distributed from the center extending outwards to the circumference forming a disc shape, as shown in Figure 3.14. Given the half-life of Sr-90, the source activity at the time of measurement (July 2018, i.e. 5.3 years later) was 3.0 GBq.

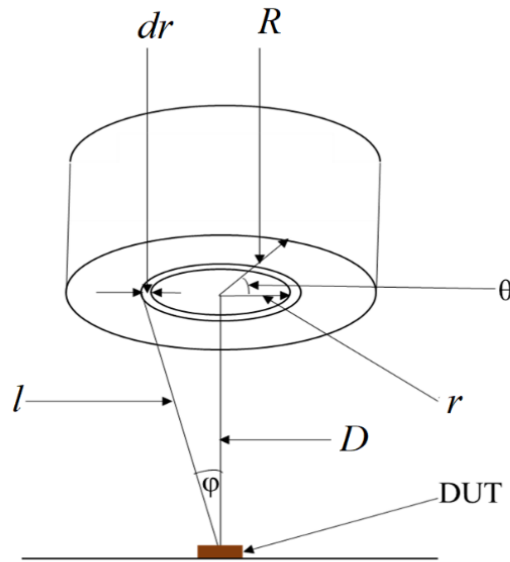

Figure 3.14: Disc shape of the Sr-90 electron radiation source used to calculate the required height for a given dose rate

In Figure 3.14, *R* is the total exterior radius of the disc shaped radiation source, *D* is the distance between the center of the disc and the DUT, *l* is the distance between the periphery of the Sr-90 material and the DUT, and *r* is the radius of the Sr-90 material disc. The angle φ extends from 0° up to $\tan^{-1}(R/D)$, while θ curves the full 0^{0} to 360^{0} circumference. The infinitesimal radiation activity δB, of an element on a ring with radius *r*, width δr and subtending an angle $\delta\theta$ was derived from Figure 3.3.1 as;

$$\delta B = \frac{B}{\pi R^2} r\delta r\delta\theta \, . \tag{3.1}$$

The relationship between *B* and the fluence rate *Ø* incident on the surface was established as,

$$\delta\phi = \frac{\delta B}{4\pi l^2}\cos\varphi \tag{3.2}$$

where

$$\cos\varphi = \frac{D}{\sqrt{D^2 + r^2}} \tag{3.3}$$

Therefore ∅, can be re-written as:

$$\phi = \int_0^R \int_0^{2\pi} \frac{\frac{B}{\pi R^2}\cos\varphi . r\delta\theta\delta r}{4\pi l^2}$$

$$\phi = \frac{BD}{2\pi R^2}\left[\frac{1}{D} - \frac{1}{\sqrt{R^2 + D^2}}\right] \tag{3.4}$$

B for the radiation source is 3.0 GBq and the radius *R* is 0.945 cm.

If we let $\frac{B}{2\pi R^2}$ in the equation above be equal to σ_o , then ϕ will be given as,

$$\phi = \sigma_o D\left[\frac{1}{D} - \frac{1}{\sqrt{R^2 + D^2}}\right] \tag{3.5}$$

This eventually give as a relationship between *D* and ϕ expressed as,

$$D = \frac{R}{\sqrt{\frac{1}{\left(1 - \frac{\phi}{\sigma_o}\right)^2} - 1}} \tag{3.6}$$

3.3.4 Determination of dose rate and radiation dose

The maximum value of $\emptyset$=6.0 x 10^8/cm^{2}s of the radiation source is achieved at the surface when the dose rate is also maximum. The relationship between the dose rate s and $\emptyset$ is:

$$s = k_c Q\left({dE}/{dx} \right) \tag{3.7}$$

where s is the dose rate in rad(Si)/s, k_c = 6.9 x 10^{-9} rad(Si)/(MeV/cm^3) [35] is the conversion factor to rad(Si), ${dE}/{dx}$ is the linear stopping power in MeV/cm. The linear stopping power is obtained by multiplying the mass stopping power with the density of the absorbing medium. Using the density and the stopping power of silicon as 2.33 g/cm^3 and 1.5 MeV.cm^2/g respectively, the calculated ${dE}/{dx}$ was 3.7 MeV/cm.

3.3.5 Radiation exposure of SiGe HBT

SiGe HBT was exposed to different radiation doses at a constant dose rate of 32 krad(Si)/hr, with linear measurements taken after each incremental radiation dose. This radiation dose rate was chosen to be within the range of dose rates in the standard window of ESCC 22900, with further consideration to the targeted total dose and personal safety considerations. At this dose rate, the separating distance between the radiation source and DUT was determined to be 0.4 cm using (3.6). The radiation exposure periods and accumulated TID dose (*d*) are shown in Table 3.2.

Table 3.2: Dose rate and cumulative *d* in SiGe HBT radiation experiment

Radiation Exp	Dose Rate (krad(Si)/hr)	Cumulative *d* (krad)
1	32	240
2	32	600
3	32	1200
4	32	1800
5	32	2400

3.3.6 Radiation exposure of bulk CMOS devices

Bulk CMOS devices were equally exposed to different total dose levels at a constant dose rate of 32 krad(Si)/hr, and linear measurements followed after each incremental radiation dose. The radiation exposure period and the accumulated total dose are shown in Table 3.3.

Table 3.3: Dose rate and cumulative total dose in bulk CMOS radiation experiment

Radiation Exp	Dose Rate (krad(Si)/hr)	Cumulative TID (krad)
1	32	32
2	32	110
3	32	210
4	32	320
5	32	430

3.4 S-PARAMETER MEASUREMENTS

Linear measurements were done to obtain S-parameters before and after incremental doses of TID for both the SiGe HBT and bulk CMOS devices. To achieve this, the Anritsu ME 7828A vector network analyser (VNA) was setup and connected to the DUT through GSG wafer probing. Muxcouplers at both ports provided bias tees for DC biasing.

The VNA was calibrated for frequencies between 1 GHz and 110 GHz at an input power of -15 dBm and 1001 points using LRM algorithm to shift the calibration plane to the probe tips, using calibration standards from the ceramic ISS. S-parameters measurements were then done for the SiGe HBT, as well as for the OPEN and SHORT calibration standards for purposes of de-embedding (to shift the plane to the terminals of the device). The de-embedding process and parameter extraction method for the SiGe HBT are discussed in Section 3.6.1.

To measure S-parameters for the bulk CMOS devices, the VNA was set to frequencies between 1 GHz and 50 GHz, the input power was set to -15 dBm and the number of point was set to 1001. The first tier LRM calibration was used again to shift the calibration plane to the probe tips. Measurement of S-parameters for the devices were done and were followed by measurements of S-parameters for the THRU, REFLCT and LINE calibration standards in preparation for de-embedding using the TRL method during post processing to remove the effect of pad and feedline parasitics from the measurement. Figure 3.15 to Figure 3.16 show the photos taken in the cleanroom for S-parameter measurements setup.

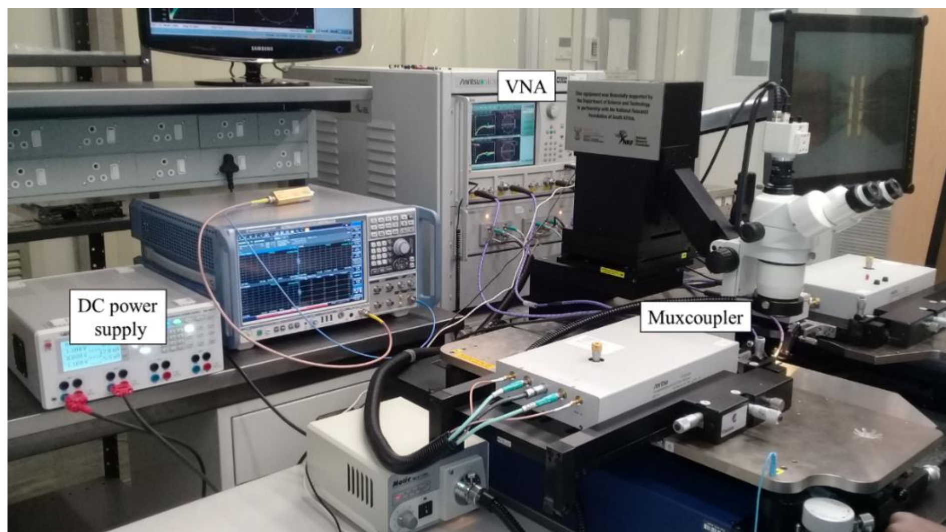

Figure 3.15: Photo of the setup for S-parameter measurements in the cleanroom

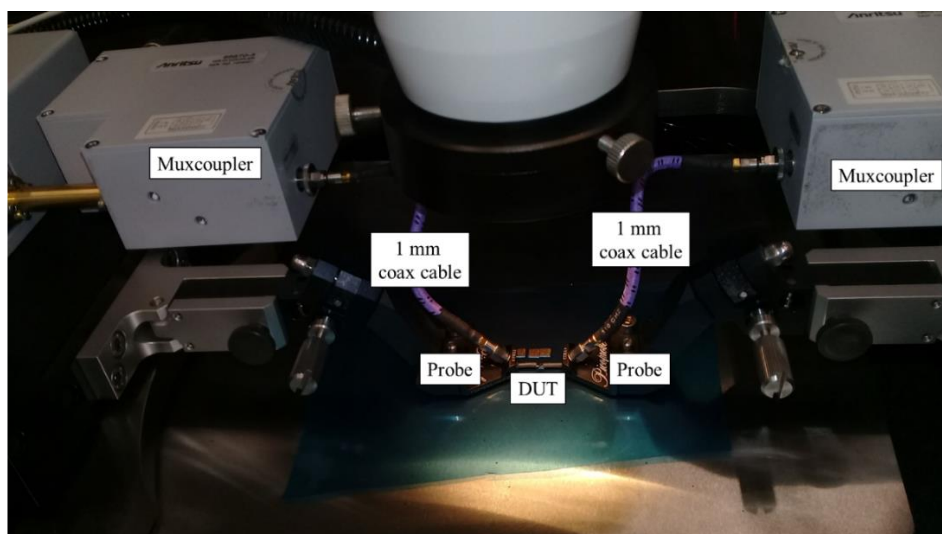

Figure 3.16: Photo of the DUT under the probes in the cleanroom

3.5 MODEL EXTRACTION

Small signal model parameters were extracted for both SiGe HBT and bulk CMOS devices from the measured S-parameters pre- and post-irradiation.

3.5.1 Linear small signal model extraction for SiGe HBT

In this work, the small signal equivalent circuit model presented in [18] and in [36], has been modified and adopted for the DUT at mm-wave frequencies. The modifications to the already existing model include the introduction of inductors at the base, collector and emitter which has been done to improve the accuracy of the model at mm-wave frequencies. The adopted small equivalent circuit model shown in Figure 3.17 is therefore inclusive of parasitics from pads, vias and feedlines.

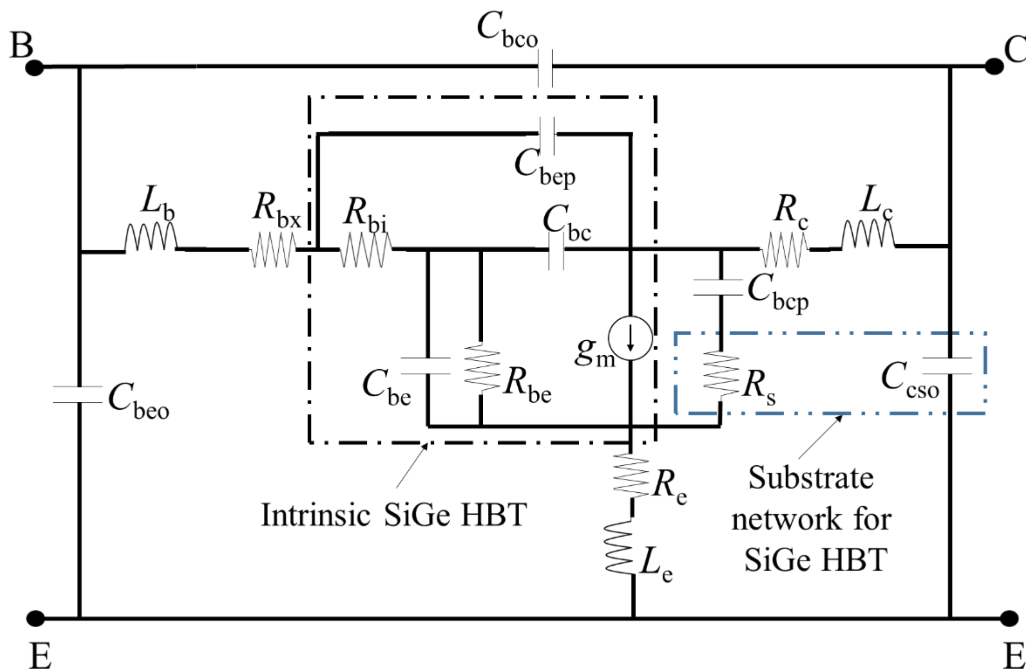

Figure 3.17: Small signal equivalent circuit for SiGe HBT

To extract the small signal model parameters, measured S-parameters are de-embedded to remove the effect of parasitics from the pads, vias and feedlines represented by the extrinsic

parameters C_{beo}, C_{bco}, C_{bcp}, L_b, L_c, L_e, R_{bx}, R_c and R_e in Figure 3.17; no distinction is, therefore, drawn between extrinsic parameters of the transistor layout and the connecting circuitry. As the purpose of the study is to study changes to the intrinsic, rather than the extrinsic model, this was considered a fair approach. The extraction is done using the SHORT and OPEN de-embedding method [36] with the OPEN and SHORT calibration standards. As this method de-embeds all interconnect parasitics up to the junction, including extrinsic device parasitics, no further de-embedding (using e.g TRL) is possible, or necessary. The Y matrix for the complete device model inclusive of the extrinsic parameters can be represented as;

$$Y = Y_{PAD} + \left[Z_{RL} + Z_D\right]^{-1} \tag{3.8}$$

In (3.8), Y_{PAD} represents the pad capacitances, Z_{RL} represents the parasitic resistances and inductances due to vias and feedlines and Z_D represents impendence of the intrinsic circuit. The matrices for Y_{PAD} and Z_{RL} are given as;

$$Y_{PAD} = \begin{bmatrix} j\omega\left(C_{beo} + C_{bco}\right) & -j\omega C_{bco} \\ -j\omega C_{bco} & j\omega\left(C_{bcp} + C_{bco}\right) \end{bmatrix} \tag{3.9}$$

$$Z_{RL} = \begin{bmatrix} R_{bx} + R_c + j\omega\left(L_b + L_e\right) & R_e + j\omega L_e \\ R_e + j\omega L_e & R_c + R_e + j\omega\left(L_c + L_e\right) \end{bmatrix} \tag{3.10}$$

To determine the parasitic capacitances in (3.10), S-parameters measured from the OPEN calibration standard are converted to Y-parameters using the equations shown below.

$$\Delta S = \left(\left(1 + s_{11}\right)\left(1 + s_{22}\right) - s_{12}s_{21}\right) \tag{3.11}$$

$$y_{11} = \frac{\left(\left(1 - s_{11}\right)\left(1 + s_{22}\right) + s_{12}s_{21}\right)}{\Delta S} \tag{3.12}$$

$$y_{12} = \frac{-2s_{12}}{\Delta S} \tag{3.13}$$

$$y_{21} = \frac{-2s_{21}}{\Delta S} \tag{3.14}$$

$$y_{22} = \frac{\left((1+s_{11})(1-s_{22})+s_{12}s_{21}\right)}{\Delta S} \tag{3.15}$$

Parasitic capacitances can then be directly extracted from Y-parameters using the following equations.

$$C_{beo} = \frac{1}{\omega}\mathrm{Im}\left(y_{11}+y_{12}\right) \tag{3.16}$$

$$C_{bep} = \frac{1}{\omega}\mathrm{Im}\left(y_{22}+y_{21}\right) \tag{3.17}$$

$$C_{bco} = \frac{1}{\omega}\mathrm{Im}\left(y_{21}\right) \tag{3.18}$$

Z-parameters can be obtained from the transformation of measured S-parameters using the following equations.

$$\Delta S = (1-s_{11})(1-s_{22})-s_{12}s_{21} \tag{3.19}$$

$$z_{11} = \frac{\left((1+s_{11})(1-s_{22})+s_{12}s_{21}\right)}{\Delta S}Z_0 \tag{3.20}$$

$$z_{12} = \frac{2\,\mathrm{s}_{12}}{\Delta S}Z_0 \tag{3.21}$$

$$z_{21} = \frac{2\,\mathrm{s}_{21}}{\Delta S}Z_0 \tag{3.22}$$

$$z_{22} = \frac{\left((1-s_{11})(1+s_{22})+s_{12}s_{21}\right)}{\Delta S}Z_0 \tag{3.23}$$

Parasitic resistances and inductances in (3.10) can be extracted from for the SHORT calibration standard.

$$R_{bx} = \mathrm{Re}\left(z_{11}-z_{12}\right) \tag{3.24}$$

$$R_c = \mathrm{Re}\left(z_{22}-z_{21}\right) \tag{3.25}$$

$$R_e = \mathrm{Re}\left(z_{12}\right) \tag{3.26}$$

$$L_b = \frac{1}{\omega}\operatorname{Im}\left(z_{11} - z_{12}\right) \tag{3.27}$$

$$L_c = \frac{1}{\omega}\operatorname{Im}\left(z_{22} - z_{21}\right) \tag{3.28}$$

$$L_e = \frac{1}{\omega}\operatorname{Im}\left(z_{12}\right) \tag{3.29}$$

To determine the substrate elements R_s and C_{cso}, S-parameters obtained from 'cold' measurements of SiGe HBT with the base voltage V_{BE} = 0V and the collector voltage V_{CE} = 1V are transformed to admittance parameters Y_c. The substrate elements are then extracted as:

$$C_{cso} = -\left[\omega \operatorname{Im}\left\{\frac{1}{y_{c_{12}} + y_{c_{22}}}\right\}\right]^{-1} \tag{3.30}$$

$$R_s = \operatorname{Re}\left\{\frac{1}{y_{c_{12}} + y_{c_{22}} - j\omega C_{cso}}\right\} \tag{3.31}$$

The substrate parameter y_{sub} can then be obtained as:

$$y_{sub} = \frac{j\omega C_{bcp}}{1 + j\omega C_{bcp} R_s} \tag{3.32}$$

Once the parasitic and the substrate elements are known, the extraction of the intrinsic elements can be carried out as follows:

1. The measured S-parameters for the SiGe HBT can be transformed into admittance parameters Y_D and the pad capacitances determined in (3.16) to (3.18) can be subtracted to obtain the admittance parameters Y'_D as:

$$Y_D^{'} = Y_D - \begin{bmatrix} j\omega\left(C_{beo} + C_{bco}\right) & -j\omega C_{bco} \\ -j\omega C_{bco} & j\omega\left(C_{bep} + C_{bco} + C_{cso}\right) \end{bmatrix} \tag{3.33}$$

2. The admittance parameters Y'_D can then be transformed to impedance parameters Z'_D, after which parasitic resistance and inductances can be subtracted to obtain the impedance parameters Z.

$$Z = Z_D^{'} - \begin{bmatrix} R_{bx} + R_c + j\omega(L_b + L_e) & R_e + j\omega L_e \\ R_e + j\omega L_e & R_c + R_e + j\omega(L_c + L_e) \end{bmatrix} \quad (3.34)$$

3. The impedance parameter Z can then be transformed into admittance parameter Y_n and the substrate parameter y_{sub} can be de-embedded to obtain the admittance parameter Y_i for the intrinsic network.

$$Y_i = Y_n - \begin{bmatrix} 0 & 0 \\ 0 & y_{sub} \end{bmatrix} \quad (3.35)$$

4. The intrinsic parameters can then be obtained from Y_i with elements shown in (3.36),

$$Y_i = \begin{bmatrix} y_{i_{11}} & y_{i_{12}} \\ y_{i_{21}} & y_{i_{22}} \end{bmatrix} \quad (3.36)$$

The intrinsic base resistance R_{bi} can be determined from intrinsic admittance parameters.

$$R_{bi} = \mathrm{Re}\left\{ \frac{1}{y_{i_{11}}} \right\} \quad (3.37)$$

The intrinsic parameters C_{bc} and C_{bep} can be determined from admittance parameters.

$$C_{bc} + C_{bep} = \frac{1}{\omega} \mathrm{Im}\left(\frac{y_{i_{11}} y_{i_{22}} - y_{i_{12}} y_{i_{22}}}{y_{i_{11}} + y_{i_{21}}} \right) \quad (3.38)$$

$$\frac{C_{bc}}{C_{bc}+C_{bcp}}=\left[R_{bi}\,\mathrm{Re}\left\{\frac{y_{i_{11}}y_{i_{22}}-y_{i_{12}}y_{i_{21}}}{y_{i_{22}}+y_{i_{12}}}\right\}\right]^{-1} \tag{3.39}$$

g_{m} can be determined:

$$g_m=\left[\mathrm{Re}\left\{\frac{1}{y_{i_{21}}-y_{i_{12}}}\right\}-R_{bi}\,\mathrm{Re}\left\{\frac{y_{i_{11}}+y_{i_{12}}}{y_{i_{21}}-y_{i_{12}}}\right\}\right]^{-1} \tag{3.40}$$

The parameters C_{be} and R_{be} can be determined as follows:

$$R_{be}=\left[\mathrm{Re}\left(\frac{-y_{i_{11}}\left(1+R_{bi}.j\omega C_{bc}\right)+j\omega C_{bc}\left(1+R_{bi}.j\omega C_{bep}\right)+j\omega C_{bep}}{R_{bi}\left(y_{i_{11}}-j\omega C_{bep}\right)-1}\right)\right]^{-1} \tag{3.41}$$

$$C_{be}=\frac{1}{\omega}\mathrm{Im}\left(\frac{-y_{i_{11}}\left(1+R_{bi}.j\omega C_{bc}\right)+j\omega C_{bc}\left(1+R_{bi}.j\omega C_{bep}\right)+j\omega C_{bep}}{R_{bi}\left(y_{i_{11}}-j\omega C_{bep}\right)-1}\right) \tag{3.42}$$

This process is repeated for measured set of S-parameters after each incremental radiation dose.

To validate the extracted small signal model, Y-parameters are calculated from the extracted small signal parameters and later transformed to S-parameters. A comparison of the calculated S-parameters to measured S-parameters is then done. The following equations relating Y-parameters to small signal parameters are used

$$y_{11}=\frac{y_{be}+y_{bc}}{1+R_{bi}\left(y_{be}+y_{bc}\right)}+y_{bep} \tag{3.43}$$

$$y_{12}=\frac{-y_{bc}}{1+R_{bi}\left(y_{be}+y_{bc}\right)}-y_{bep} \tag{3.44}$$

$$y_{21}=\frac{g_m-y_{bc}}{1+R_{bi}\left(y_{be}+y_{bc}\right)}-y_{bep} \tag{3.45}$$

$$y_{22} = \frac{y_{bc} + R_{bi} y_{bc} \left(g_m + y_{be} \right)}{1 + R_{bi} \left(y_{be} + y_{bc} \right)} + y_{bep} \tag{3.46}$$

where, $y_{be} = 1/R_{be} + j\omega C_{be}$, $y_{bc} = j\omega C_{be}$ and $y_{bep} = j\omega C_{bep}$.

3.5.2 Noise model

The noise model presented in [20] and shown in Figure 2.8 was adopted in this study. The principal noise sources in this model are the base and collector shot noise ($2qI_b$ and $2qI_c$) and base thermal noise ($4kTR_{bi}$). The following equations can be used to determine the spectral densities for the input noise voltage S_{vn}, input noise current S_{in} and their cross-correlation S_{invn}^*.

$$S_{v_n} = \frac{2qI_C}{\left| y_{21} \right|^2} + 4kTR_{bi} \tag{3.47}$$

$$S_{i_n} = 2qI_B + \frac{2qI_C}{\left| h_{21} \right|^2} \tag{3.48}$$

$$S_{i_n v_n^*} = 2qI_C \frac{y_{11}}{\left| y_{21} \right|^2} \tag{3.49}$$

The optimum source admittance ($Y = G+jB$), NF and the noise resistance (R_n) can all be determined from the spectral densities given in (3.47) to (3.49) as

$$G = \sqrt{\frac{S_{i_n}}{S_{v_n}} - \left[\frac{\mathrm{Im}\left(S_{i_n v_n^*} \right)}{S_{v_n}} \right]^2} \tag{3.50}$$

$$B = -\frac{\mathrm{Im}\left(S_{i_n v_n^*} \right)}{S_{v_n}} \tag{3.51}$$

$$R_n = \frac{S_{v_n}}{4kT} \tag{3.52}$$

$$NF_{\min} = 1 + 2R_n \left(G + \frac{\operatorname{Re}\left(S_{i_n v_n^*}\right)}{S_{v_n}} \right) \tag{3.53}$$

3.5.3 Model for the 0.35 µm AMS CMOS Devices

In this work, the small signal model for a MOSFET presented in [22] has been adopted, with some modifications. The modifications include the removal of the two current sources from the circuit. Since the devices in this study have the substrate and the source tied together and connected in common source configuration, the substrate to source voltage (V_{bs}) is 0. It therefore follows that the voltage controlled current source, which depends on V_{bs}, becomes an open circuit. Similarly, the current source which is dependent on dV_g/dt has been neglected in the modifications and converted to an open circuit. This leaves the adopted model with only one voltage controlled current source which is shown in Figure 3.18.

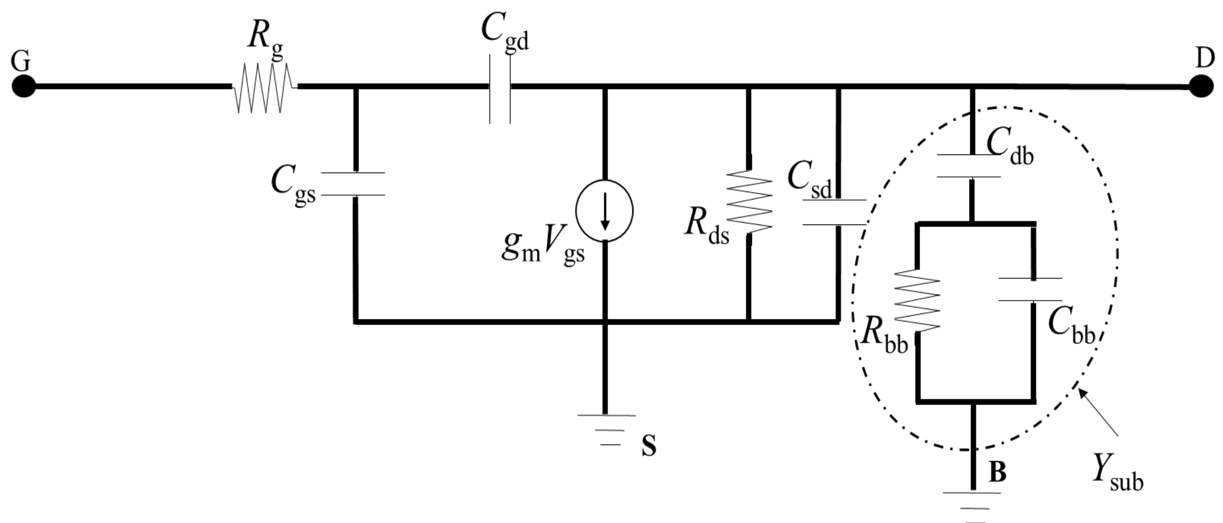

Figure 3.18: Small signal model for NMOS with some modifications

To extract small signal parameters, the measured S-parameters are first de-embedded using the TRL method presented in [37] and converted to Y-parameters. Small signal parameters are then extracted from the Y-parameters.

The gate resistance (R_g) can be extracted from the real and imaginary parts of y_{11} as

$$R_g = \frac{\mathrm{Re}(y_{11})}{\left[\mathrm{Im}(y_{11})\right]^2} \tag{3.54}$$

The gate to drain capacitance (C_{gd}) can be extracted by dividing the imaginary part of y_{12} by ω.

$$C_{gd} = \frac{-\mathrm{Im}(y_{12})}{\omega} \tag{3.55}$$

The gate to source capacitance (C_{gs}) can be obtained from the division of the sum of the imaginary parts of y_{11} and y_{12} by ω.

$$C_{gs} = \frac{\mathrm{Im}(y_{11}) + \mathrm{Im}(y_{12})}{\omega} \tag{3.56}$$

g_m can then be calculated as the y intercept of the real part of y_{21} when $\omega^2 = 0$

$$g_m = \mathrm{Re}(y_{21})|\omega^2 = 0. \tag{3.57}$$

The drain to gate capacitance (C_{dg}) can be calculated using the gradient (m_1) for the imaginary part of y_{21} against ω and other small signal parameters already extracted as

$$C_{dg} = -m_1 - \left(C_{gd} + C_{gs}\right) R_g g_m \tag{3.58}$$

The output conductance (g_{ds}) can be obtained from the y intercept of the real part of y_{22} against ω^2 as

$$g_{ds} = \mathrm{Re}(y_{22})|\omega^2 = 0. \tag{3.59}$$

The reciprocal of g_{ds} gives the parameter R_{ds} indicated in the small signal equivalent circuit. To extract the next set of small signal parameters, the parameter C_{sd} can first be ignored and y_{22} manipulated to obtain the following

$$\left[R + jI\right]\left[1 + \omega^2\sigma + \omega^4\delta\right] = \omega^4\alpha + \omega^2\mu + j\left[\omega^5\varepsilon + \omega^3\rho + \omega\tau\right] \tag{3.60}$$

with,

$$R = \mathrm{Re}(y_{22}) - g_{ds} - \mathrm{Re}(y_a) \tag{3.61}$$

$$I = \mathrm{Im}(y_{22}) - \omega C_{gd} - \mathrm{Im}(y_a) \tag{3.62}$$

while

$$y_a = \frac{\omega^2 C_{gd} R_g \left[\left(C_{gd} + C_{gs}\right) R_g g_m + C_{dg}\right] + j\omega C_{gd} R_g \left[g_m - \omega^2 C_{gd} R_g \left(C_{gd} + C_{gs}\right)\right]}{1 + \omega^2 R_g^2 \left(C_{gd} + C_{gs}\right)^2} \tag{3.63}$$

and

$$\alpha = R_{bb}^2 C_{db} C_{bb}^2 \left[C_{db}\left(1 + g_{mb} R_{bb}\right) + g_{mb} R_{bb} C_{bb}\right] \tag{3.64}$$

$$\mu = R_{bb} C_{db} \left[C_{db}\left(1 + g_{mb} R_{bb}\right) + g_{mb} R_{bb} C_{bb}\right] \tag{3.65}$$

$$\sigma = R_{bb}^2 \left[C_{bb}^2 + \left(C_{db} + C_{bb}\right)^2\right] \tag{3.66}$$

$$\delta = R_{bb}^4 C_{bb}^2 \left(C_{db} + C_{bb}\right)^2 \tag{3.67}$$

$$\varepsilon = R_{bb}^4 C_{db} C_{bb}^3 \left(C_{db} + C_{bb}\right) \tag{3.68}$$

$$\rho = R_{bb}^2 C_{db} C_{bb} \left[C_{db} + C_{bb} + C_{bb}\left(1 + g_{mb} R_{bb}\right)\right] \tag{3.69}$$

$$\tau = C_{db}\left(1 + g_{mb} R_{bb}\right) \tag{3.70}$$

At high frequencies, the following linear relationships can be obtained from (3.61) and (3.62).

$$\frac{\omega^2}{R} = \omega^2 m_2 + c_2 \tag{3.71}$$

$$\omega \frac{I}{R} = \omega^2 m_3 + c_3 \tag{3.72}$$

The parameter C_{db}, can then be calculated from the slope of (3.71) and (3.72) as

$$C_{db} = \frac{m_3}{m_2} \tag{3.73}$$

To extract the parameters C_{bb} and R_{bb}, the relationship between the slopes and intercepts of (3.71) and (3.72) must be established and can be expressed as;

$$m_2^2 = \frac{m_3}{c_3}\left[\frac{C_{bb}^2 + \left(C_{db} + C_{bb}\right)^2}{C_{db}^2\left(1 + g_{mb} R_{bb}\right)^2 + \left(g_{mb} R_{bb} C_{bb}\right)^2 + 2C_{db}\left(1 + g_{mb} R_{bb}\right)\left(g_{mb} R_{bb} C_{bb}\right)}\right] \tag{3.74}$$

Where $g_{mb}R_{bb} = \tau/C_{db} - 1$, while τ is obtained from (3.70) and C_{db} is obtained from (3.73). The parameter g_{mb} is part of the current source ($g_{mb}V_{bs}$) which as ignored, because the voltage

V_{bs} is zero, as the substrate is tied to the source. This parameter is however required in the process of parameter extraction as other parameters depend on it. The expression in (3.74) can therefore be rearranged and reduced to a quadratic relationship given as;

$$xC_{bb}^2 + yC_{bb} + z = 0 \tag{3.75}$$

with;

$$x = 2 - \frac{m_3^2 c_2}{m_2}\left(g_{mb}R_{bb}\right)^2 \tag{3.76}$$

$$y = 2C_{db} - 2\left(\frac{m_3^2}{m_2}\right)\left(g_{mb}R_{bb}C_{db}\right)\left(1 + g_{mb}R_{bb}\right) \tag{3.77}$$

$$z = C_{db}^2\left[1 - \left(\frac{m_3^2 c_2}{m_2}\right)\left(1 + g_{mb}R_{bb}\right)^2\right] \tag{3.78}$$

The parameters C_{bb} and R_{bb} can then be extracted as,

$$C_{bb} = \frac{-y + \sqrt{y^2 - 4xz}}{2x} \tag{3.79}$$

and

$$R_{bb} = \frac{1}{C_{bb}\left(C_{db} + C_{bb}\right)}\sqrt{\frac{m_2}{c_2}\left[C_{bb}^2 + \left(C_{db} + C_{bb}\right)^2\right]} \tag{3.80}$$

Finally, the parameter C_{sd} can be extracted as:

$$C_{sd} = \frac{I - \left(\omega^5\varepsilon + \omega^3\rho + \omega\tau\right)\Big/\left(1 + \omega^2\sigma + \omega^4\delta\right)}{\omega} \tag{3.81}$$

This process of small signal parameter extraction was repeated before and after incremental doses of TID.

To validate the small signal model, Y-parameters are calculated from the extracted small signal model parameters and transformed to S-parameters. These S-parameters are then compared to S-parameters from measurements. The equations relating Y-parameters to small signal parameters which were derived in [22] with an assumption that $\omega^2 R_g^2(C_{gd} + C_{gs})^2 << 1$ are expressed as:

$$y_{11} = \omega^2 \left(C_{gd} + C_{gs}\right)^2 R_g + j\omega\left(C_{gd} + C_{gs}\right) , \quad (3.82)$$

$$y_{12} = -\omega^2 C_{gd} \left(C_{gd} + C_{gs}\right) R_g - j\omega C_{gd} , \quad (3.83)$$

$$y_{21} = g_m - \omega^2 C_{dg} \left(C_{gd} + C_{gs}\right) R_g - j\omega\left[\left(C_{gd} + C_{gs}\right) R_g g_m + C_{dg}\right] , \quad (3.84)$$

$$y_{22} = y_{sub} + g_{ds} + j\omega\left(C_{sd} + C_{gd}\right) + g_{mb}\left[\frac{V_{bs}}{V_{ds}}\right] + \omega^2 C_{gd} R_g \left[\left(C_{gd} + C_{gs}\right) R_g g_m + C_{dg}\right] + j\omega C_{gd} R_g \left[g_m - \omega^2 C_{gd} R_g \left(C_{gd} + C_{gs}\right)\right], \quad (3.85)$$

where $\frac{V_{bs}}{V_{ds}} = y_{sub}\left[\frac{\left(1 + j\omega C_{bb} R_{bb}\right) R_{bb}}{1 + \omega^2 R_{bb}^2 C_{bb}^2}\right]$ and

$$y_{sub} = \frac{\omega^2 R_{bb} C_{bb}^2}{1 + \omega^2 R_{bb}^2 \left(C_{db} + C_{bb}\right)^2} + \frac{j\omega C_{db} + j\omega^3 R_{bb}^2 C_{db} C_{bb} \left(C_{db} + C_{bb}\right)}{1 + \omega^2 R_{bb}^2 \left(C_{db} + C_{bb}\right)^2}$$

3.6 CURVE FITTING AND MODEL EXTRAPOLATION

The extracted intrinsic small signal parameters for SiGe HBT and for the bulk CMOS devices were mapped to the corresponding total radiation dose (*d*). The curve fitting toolbox in MATLAB was used to generate equations for curves that best fitted the extracted small signal parameters. The coefficient of determination (R^2) was calculated to establish the variability of the derived equations to the curve of best fit for each of the small signal parameters against extracted values.

The derived equations were used to calculate values of model parameters at a known value of *d* and model parameters at an unknown higher value of *d*. S-parameters were then calculated in the frequency range of 1 GHz to 110 GHz using the calculated model parameters for SiGe HBT. The calculated S-parameters from the known value of *d* were compared to S-parameters from measurement for SiGe HBT, while the calculated S-parameters from the unknown value of *d* was compared with the other graphs to establish the ability of the derived equations to predict damage to the transistor due to radiation.

Similarly, for bulk CMOS devices, the derived equations were used to calculate values of model parameters at a known value of d, and model parameters at an unknown higher value of d. S-parameters were calculated in the frequency range of 1 GHz to 50 GHz using the calculated model parameters for bulk CMOS. The calculated S-parameters from the known value of d were compared to the de-embedded S-parameters from measurement for bulk CMOS devices, while the calculated S-parameters from the unknown value of d was compared with the other graphs to establish the ability of the derived equations in predicting damage to the transistor due to radiation.

3.7 CHAPTER SUMMARY

In this chapter, the prototyping of the SiGe HBT, and the OPEN and SHORT calibration standards has been presented. The chapter also presented the prototyping of bulk CMOS devices and the THRU, REFLECT and LINE calibration standards. The procedure for radiation experiment with details on the radiation experiment setup, determination of the dose rate, the radiation exposure of SiGe HBT and bulk CMOS device presented. The chapter further presented details on S-parameter measurement. The chapter thereafter presented the parameter extraction method for the SiGe HBT in which the de-embedding of pads and feedlines were done together with the extraction of small signal parameters and parameters representing the substrate network. The parameter extraction method for bulk CMOS devices using de-embedded S-parameters was also presented. While the de-embedding of parasitics from pads and feedlines was part of the extraction method for SiGe HBT, it was not part of the extraction method in bulk CMOS devices. The chapter closed with a presentation on curve fitting and model extrapolation for both SiGe HBT and bulk CMOS small signal parameters.

CHAPTER 4 SiGe BiCMOS RESULTS

This chapter first presents the extracted small signal model parameters of SiGe HBT before and after incremental radiation doses. A comparison of simulation results from the extracted model to measured results, as well as to simulated results from the model of the PDK, are then presented. The chapter further compares the noise figure extracted from measured S-parameters to the simulated noise figure from the PDK model, and presents the effect of radiation on noise figure and noise resistance. Equations relating each of the small signal parameters to *d* are then presented. The chapter ends with the validation and usage demonstration of the derived small signal model equations.

4.1 SMALL SIGNAL MODEL PRE-AND POST-RADIATION

The extracted small signal parameters for the model shown in Figure 3.17 using the extraction method outlined in Section 3.5.1, are shown in Table 4.1.

Table 4.1: Extracted intrinsic small signal parameters and substrate parameters

Radiation Dose	R_{bi} **(Ω)**	R_{be} **(kΩ)**	C_{be} **(fF)**	C_{bc} **(fF)**	g_m **(S)**	C_{bep} **(fF)**	R_s **(Ω)**	C_{cso} **(fF)**
Pre-rad	31.61	1.99	81.11	3.96	0.125000	2.938	100.69	0.1000
240 krad	31.77	2.11	81.13	3.98	0.124986	2.941	106.44	0.1059
600 krad	31.94	2.24	81.19	4.03	0.124979	2.944	111.83	0.1096
1200 krad	32.10	2.37	81.23	4.07	0.124972	2.949	114.67	0.1109
1800 krad	32.17	2.48	81.29	4.12	0.124968	2.952	119.59	0.1123
2400 krad	32.32	2.61	81.36	4.15	0.124946	2.957	123.46	0.1138

As shown in Table 4.1, the resistance and capacitance values generally increase as *d* increases while g_m reduces with increase in *d*. The underlying physical interpretation for this trend is discussed in detail in Section 6.1.

4.2 SIMULATION, MODEL AND MEASUREMENT RESULTS

A comparison of S-parameters simulated from the pre-radiation extracted model to the measured S-parameters from the VNA and to the S-parameters simulated from the model in the PDK is done to evaluate the model parameter extraction process. The S-parameter comparisons are shown in Figure 4.1 to Figure 4.4.

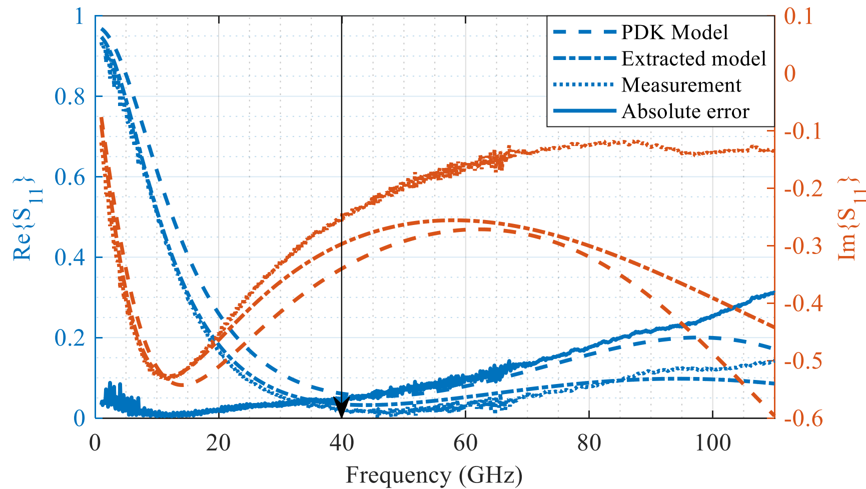

Figure 4.1: Comparison of S_{11} for the extracted model to measurement and the PDK model

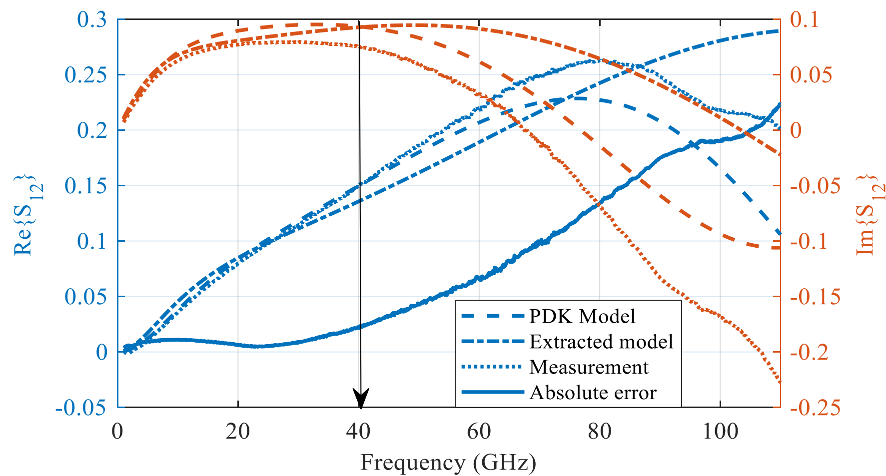

Figure 4.2: Comparison of S_{12} for the extracted model to measurement and the PDK model

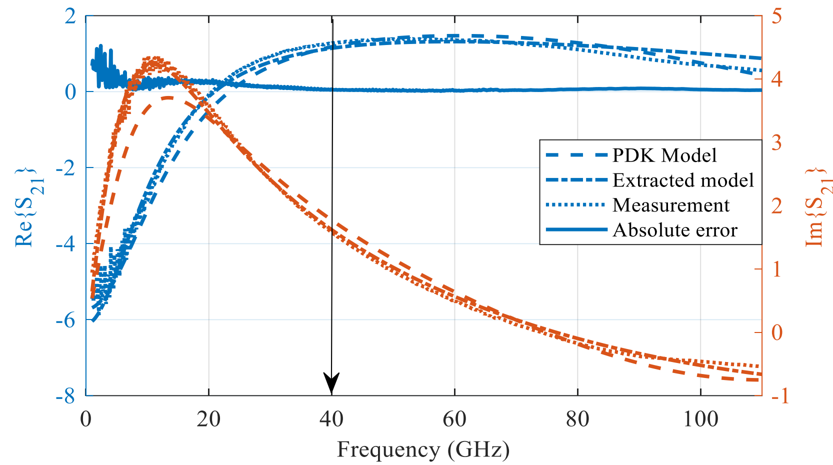

Figure 4.3: Comparison of S_{21} for the extracted model to measurement and the PDK model

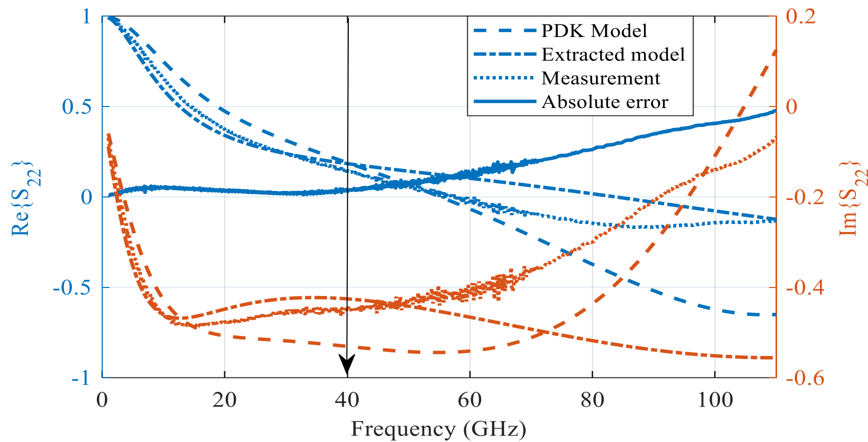

Figure 4.4: Comparison of S_{22} for the extracted model to measurement and the PDK model

There is generally a good agreement in the measured S-parameters with the S-parameters from the extracted model as well as the S-parameters from the model in the PDK at lower frequencies. However, some deviation is observed at higher frequencies, mainly above 40 GHz. This trend can be attributed to the OPEN and SHORT de-embedding method used in post processing the measured results which peels away the entire extrinsic device, leaving only the intrinsic parameters, whereas the pcell includes both the intrinsic and extrinsic structure.

The OPEN and SHORT calibration method uses lumped equivalent circuit to describe parasitics [38]. At higher frequencies, however, the distributive nature of parasitics lead to inaccuracies in the OPEN and SHORT calibration method [39]. This calibration method also

requires the use of ideal OPEN and SHORT calibration standards of which the manufactured standards are good approximations at low frequencies, but not at mm-wave frequencies [38]. The method could however not be avoided as it was required for the adopted small signal model and the extraction method.

Furthermore, the discrepancies between the S-parameters from the model in the PDK and the measured S-parameters can be attributed to the characterisation of the transistor (pcell) in the PDK, which is only validated up to 40 GHz. It therefore follows that S-parameters obtained from the simulations beyond 40 GHz from the model in the PDK are not expected to accurately agree with measured S-parameters.

4.3 NOISE FIGURE SIMULATION AND MODELLING RESULTS

To evaluate the noise parameter extraction process, the noise figure results from simulation of the pcell as outlined in Section 3.1 is compared to the modelled noise figure from measured S-parameters. These are presented in Figure 4.5 for frequencies between 1 GHz and 40 GHz since the pcell is not valid beyond 40 GHz.

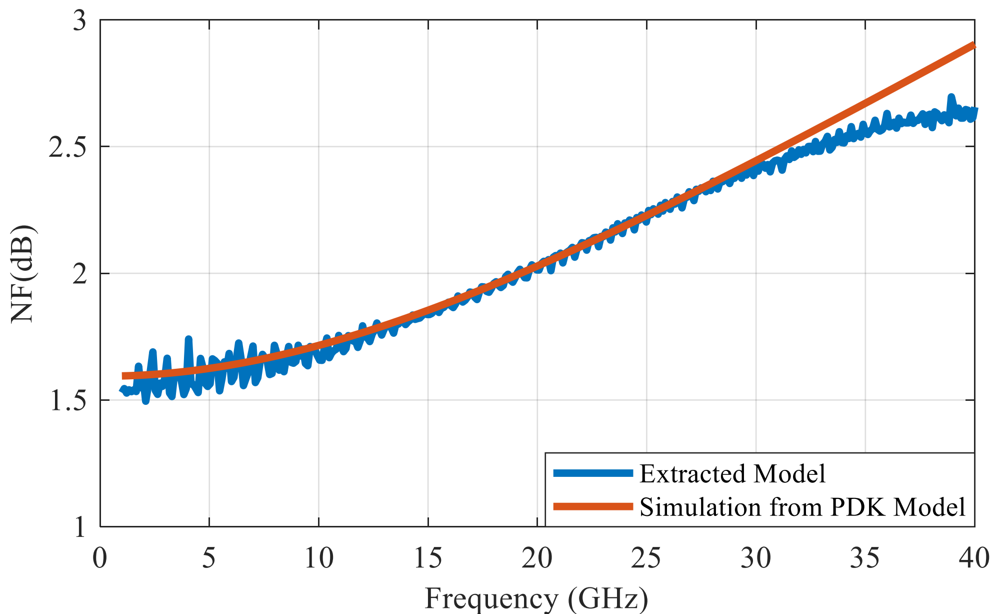

Figure 4.5: Comparison of pcell simulated noise figure to modelled noise figure

Good agreement between the noise figure from the extracted model and the noise figure simulated from the model in the PDK is evident.

To best understand the effect of radiation on noise parameters, *NF* and R_n extracted from measured S-parameters before radiation and at a *d* of 2.4 Mrad in the frequency range of 1 GHz to 40 GHz, according to the method described in Section 3.6.2, are shown in Figure 4.6.

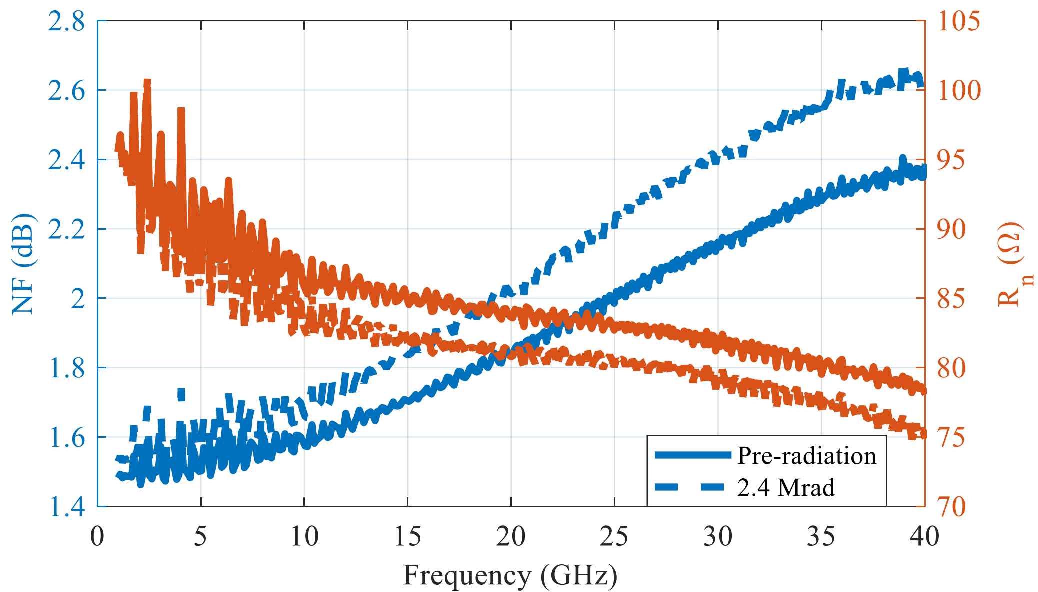

Figure 4.6: Modelled *NF* and R_n before and after radiation

The data indicates an increase in the noise figure with increase in *d*, which can be attributed to the radiation induced increase in base current leading to an increase in the base current shot noise [20]. Furthermore, the data shown is in agreement with previous research studies, which have revealed a reduction in the values of R_n with increase in frequency and *d* [29], [40].

4.4 CURVE FITTING FOR INTRINSIC SMALL SIGNAL PARAMETERS

To derive equations relating changes in the small signal model parameters and the substrate parameters presented in Section 4.1(extracted from measured S-parameters as per the method outlined in Section 3.6) to *d*, the curve fitting toolbox is MATLAB is used. The

derived equations are summarised in Table 4.2. To evaluate the accuracy of the derived model equations, R^2 was used. R^2 is a statistical measure of the similarity of the extracted small signal parameter data to the fitted regression curve. The higher values indicate greater correspondence, up to a maximum of 1 for a perfect agreement. For purposes of this study, the exponential fitting was chosen as it gave the best values of R^2 all above 0.92 while other options such as the linear fitting gave R^2 values as low as 0.7.

Table 4.2: Derived expression for the small signal parameters with their R^2 values

Small signal parameter	**Derived equation**	**R^2**
R_{bi} (Ω)	$R_{bi} = 31.89e^{0.000005446d} - 0.2825e^{-0.002596d}$	0.9959
R_{be} (kΩ)	$R_{be} = 2.164e^{0.00007783d} - 0.1758e^{0.002795d}$	0.9995
C_{be} (fF)	$C_{be} = 81.12e^{0.000001216d} - 0.01079e^{-0.003609d}$	0.9923
C_{bc} (fF)	$C_{bc} = 4.223e^{0.000002402d} – 0.2653e^{-0.003609d}$	0.9957
g_m (S)	$g_m = 0.125e^{-0.0000001506d}$	0.9224
C_{bep} (fF)	$C_{bep} = 2.946e^{0.00000171d} - 0.007794e^{-0.0006757d}$	0.9955
R_s (Ω)	$R_s = 108e^{0.00005579d} – 0.008723e^{-0.004292d}$	0.9963
C_{cso} (fF)	$C_{cso} = 0.1087e^{0.00001884d} - 0.008723e^{-0.004292d}$	0.9956

From Table 4.2, it is evident that all the values R^2 are above 0.92 indicating that the derived equations have fitted the data points accurately and are reliable.

4.5 MODEL VALIDATION AND USAGE DEMOSTRATION

To validate the model, small signal parameter values are calculated using the derived equations presented in Table 4.2 pre-radiation at which the values of small signal parameters are known. To demonstrate the use of the model, small signal parameters are calculated and S-parameter data generated at a *d* of 10 Mrad at which the values of the small signal parameters are unknown. The calculated values of the small signal parameters at *d* of 240 krad and 10 Mrad as well as the extracted small signal model values are shown in Table 4.3. The calculated values for the small signal model parameters are within of the range of extracted small signal model parameter values, which is indicative of the accuracy of the derived small signal model equations in predicting the performance of the transistor under radiation exposure.

Table 4.3: Comparison of calculated and extracted small signal model parameter values

Small signal parameter	Modelled at 240 krad	Calculated at 240 krad	Calculated at 10 Mrad
R_{bi} (Ω)	31.82	31.78	33.67
R_{be} (kΩ)	2.14	2.11	4.71
C_{be} (fF)	81.17	81.14	82.11
C_{bc} (fF)	4.09	4.11	4.33
g_m (S)	0.124992	0.124995	0.124812
C_{bep} (fF)	2.943	2.941	2.997
R_s (Ω)	109.53	109.45	188.68
C_{cso} (fF)	0.10	0.11	0.13

A comparison of the calculated S-parameters at *d* of 240 krad and 10 Mrad to the modelled S-parameters at *d* of 240 krad is done in Figure 4.7 to Figure 4.10 to evaluate the calculation and further validate the model equations.

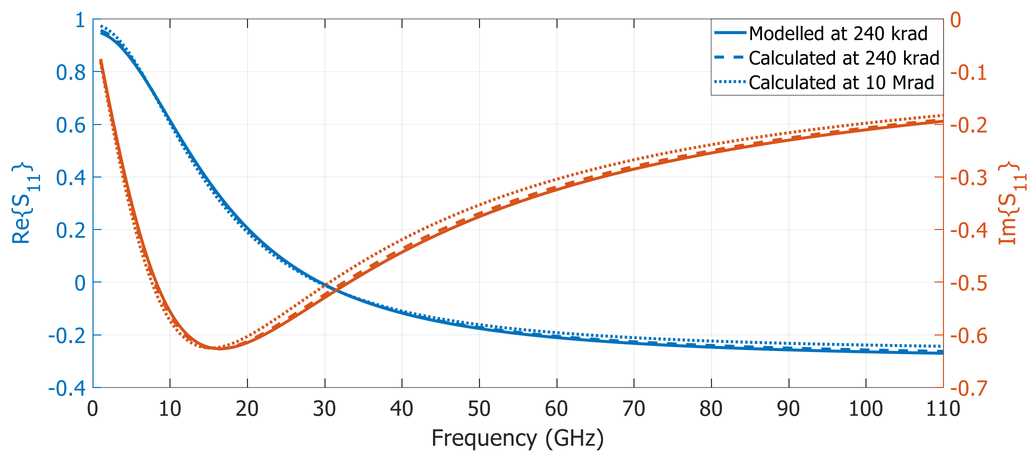

Figure 4.7: Comparison of calculated S_{11} to that of the extracted model

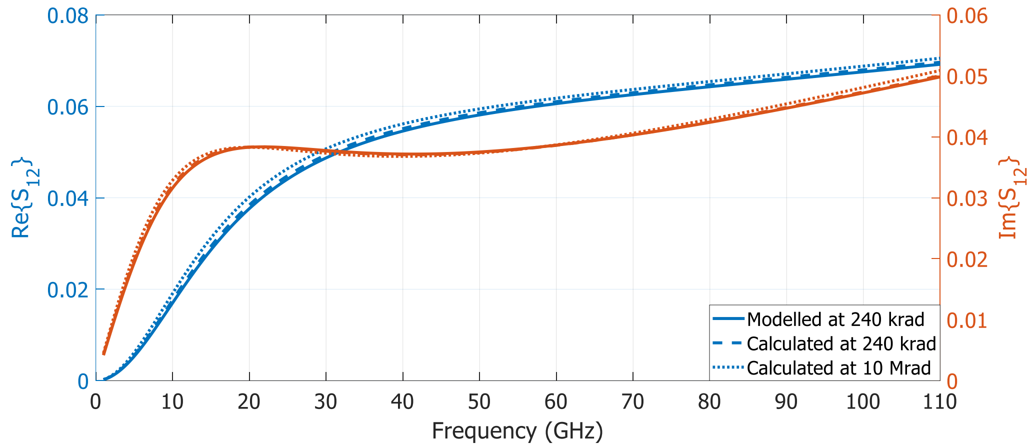

Figure 4.8: Comparison of calculated S_{12} to that of the extracted model

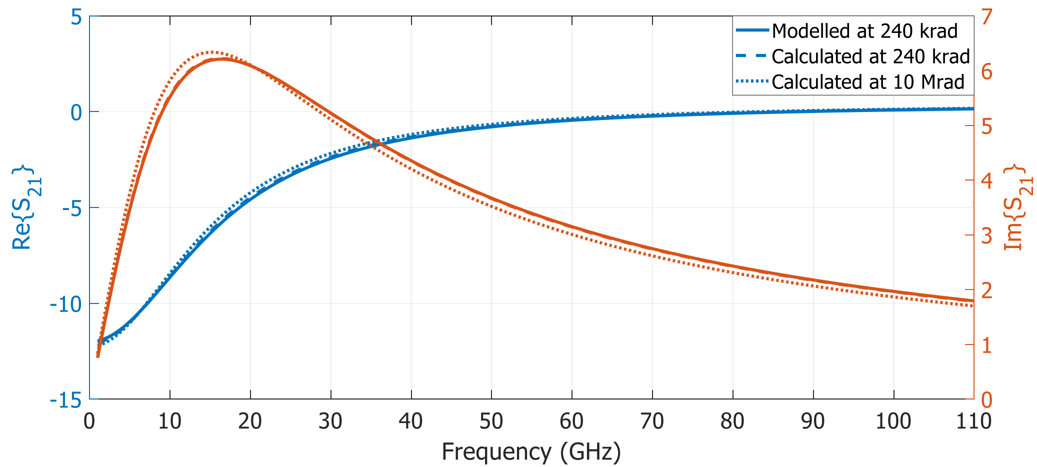

Figure 4.9: Comparison of calculated S_{21} to that of the extracted model

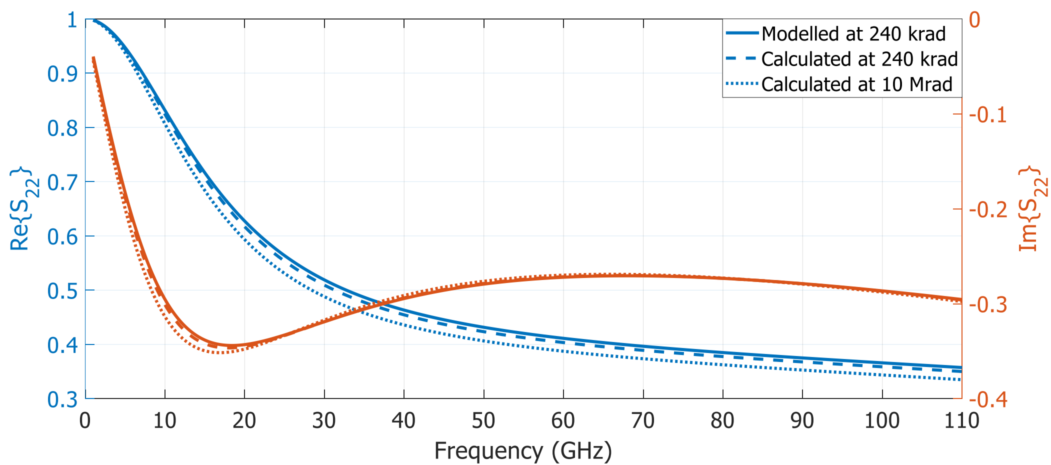

Figure 4.10: Comparison of calculated S_{22} to that of the extracted model

The calculated S-parameters are in good agreement with the modelled S-parameters, while the calculated S-parameters at a *d* of 10 Mrad shows some minimal deviation from the S-parameters modelled and calculated at 240 krad signifying the inbuilt resistance of SiGe HBTs again damage due to TID.

4.6 CHAPTER SUMMARY

In this chapter, the extracted small signal model for SiGe HBT was presented pre- and post-irradiation. S-parameters derived from the extracted model have been compared to measured S-parameters as well as S-parameters simulated from the PDK model. Good agreement between the extracted model and measured results has been shown. The chapter also presented a comparison of the modelled noise figure to the simulated noise figure in which good agreement was observed. Derived small signal model equations relating the extracted small signal model parameters to radiation dose were then presented. The chapter concluded with a validation of the derived small signal model equations by comparing the calculated S-parameter obtained from the small signal model equations at a *d* of 240 krad to simulated S-parameters from the extracted model also at a *d* of 240 krad. The calculated S-parameters at a *d* of 10 Mrad were also presented to show the anticipated effect of further TID exposure.

CHAPTER 5 BULK CMOS RESULTS

This chapter presents extracted small signal model parameters for four NMOS devices (with different gate widths) at various *d*. Comparisons of S-parameters from the extracted small signal model for each of the devices to the measured S-parameters and the S-parameters simulated from the model in the PDK are then presented. The small signal model equations derived using curve fitting application tools in MATLAB are then presented. The chapter concludes with a presentation on the validation of derived small signal model equations.

5.1 SMALL SIGNAL MODEL PRE-AND POST-RADIATION

The extracted small signal model parameters for the model shown in Figure 3.6.3, with the extraction method outlined in Section 3.6.3, are shown for the four devices with different gate width in Table 5.1 to Table 5. 4.

Table 5.1: Small signal parameters for NMOS with total gate width of 5μm at different values of *d*

Parameter	Pre-rad	32 krad	110 krad	210 krad	320 krad	430 krad
R_g(Ω)	19.91	21.93	22.66	23.84	24.92	25.68
C_{gd}(fF)	2.78	2.85	2.96	3.14	3.39	3.55
C_{gs}(fF)	50.50	52.88	55.61	57.50	59.61	60.98
g_m(mS)	1.1001	1.0998	1.0993	1.0989	1.0987	1.0984
R_{ds}(Ω)	848.82	852.68	853.99	855.02	857.16	858.96
C_{sd}(fF)	15.56	16.39	16.90	17.57	18.98	21.00
C_{db}(fF)	41.04	42.67	43.35	44.97	46.02	48.88
C_{bb}(fF)	135.27	136.68	138.98	140.12	142.78	143.64
R_{bb}(Ω)	34.89	36.77	39.07	40.85	42.06	44.19
C_{dg}(fF)	2.78	2.83	2.98	3.24	3.49	3.65

Table 5.2: Small signal parameters for NMOS with total gate width of 10µm at different values of *d*

Parameter	Pre-rad	32 krad	110 krad	210 krad	320 krad	430 krad
$R_g(\Omega)$	23.74	25.08	26.13	27.04	28.72	29.30
C_{gd}(fF)	54.04	54.47	55.27	56.14	57.24	58.03
C_{gs}(fF)	3.49	3.60	3.69	3.75	3.82	3.99
g_m(mS)	2.1011	2.1009	2.1006	2.1004	2.1001	2.1000
$R_{ds}(\Omega)$	748.60	750.88	752.09	753.96	755.09	756.75
C_{sd}(fF)	23.85	24.25	25.05	26.29	27.32	28.66
C_{db}(fF)	44.68	45.99	46.99	47.35	48.37	49.10
C_{bb}(fF)	132.85	133.61	134.78	135.49	136.76	137.98
$R_{bb}(\Omega)$	29.84	30.03	30.97	31.18	31.67	32.07
C_{dg}(fF)	3.47	3.52	3.63	3.74	3.89	3.92

Table 5.3: Small signal parameters for NMOS with total gate width of 25µm at different values of *d*

Parameter	Pre-rad	32 krad	110 krad	210 krad	320 krad	430 krad
$R_g(\Omega)$	16.84	17.15	18.00	18.35	19.25	20.01
C_{gd}(fF)	14.78	16.01	18.82	20.47	22.29	24.19
C_{gs}(fF)	79.80	80.31	81.82	83.88	84.01	86.29
g_m(mS)	5.900	5.895	5.893	5.889	5.886	5.882
$R_{ds}(\Omega)$	616.62	629.64	648.94	674.15	693.38	712.08
C_{sd}(fF)	21.92	23.77	25.75	28.67	31.99	35.01
C_{db}(fF)	51.74	53.03	56.97	58.01	62.88	66.99
C_{bb}(fF)	56.25	57.87	58.94	60.02	61.50	62.99
$R_{bb}(\Omega)$	59.14	100.60	129.42	143.16	158.64	164.94
C_{dg}(fF)	14.77	15.69	16.99	18.67	21.35	24.01

Table 5.4: Small signal parameters for NMOS with total gate width of 50µm at different values of *d*

Parameter	Pre-rad	32 krad	110 krad	210 krad	320 krad	430 krad
$R_g(\Omega)$	38.60	41.52	48.47	58.70	69.27	80.26
C_{gd}(fF)	4.67	4.82	5.00	5.42	5.67	5.93
C_{gs}(fF)	100.46	102.16	106.95	109.16	112.79	115.80
g_m(mS)	12.60	12.50	12.30	12.10	11.89	11.49
$R_{ds}(\Omega)$	619.43	647.51	670.92	699.26	715.18	736.28
C_{sd}(fF)	45.84	46.93	48.22	52.99	54.10	57.86
C_{db}(fF)	64.92	65.13	67.01	69.55	71.32	74.00
C_{bb}(fF)	90.81	94.13	98.92	103.02	107.31	113.42
$R_{bb}(\Omega)$	74.58	76.22	77.91	79.02	80.35	82.00
C_{dg}(fF)	62.52	66.79	69.02	73.47	77.99	90.75

From the data presented in Table 5.1 to Table 5.4, it is evident that the extracted g_m of the devices increase when the total gate width is increased while the drain and source junction capacitances increase when the number of gate fingers is increased, as is expected [41]. The presented data also show an increase in R_{bb} with increase in the number of gate fingers. This is because an increase in the number of gates introduces a more resistive inner junction to body contacts, which ultimately leads to an increase in R_{bb} as reported in [57]. For R_g, however, the opposite is true (as shown in Table 5.1 and Table 5.3) as an increase in the number of gate fingers leads to a reduction in R_g, as discussed in [58]. Furthermore, the data presented indicates an increase in resistance and capacitance values with increase in *d* and a reduction in g_m with increase in *d*. The underlying physical interpretation of these parameters changes with increase in *d* is discussed in Section 6.2.

5.2 SIMULATION, MODEL AND MEASUREMENT RESULTS

Simulated S-parameters from the extracted small signal model for each of the four devices are compared to S-parameters from measurement, as well as to simulated S-parameters from the model in the PDK, to evaluate the parameter extraction method. Figure 5.1 to Figure 5.4

show the comparisons for the device with a single gate finger having a total gate width of 5 μm.

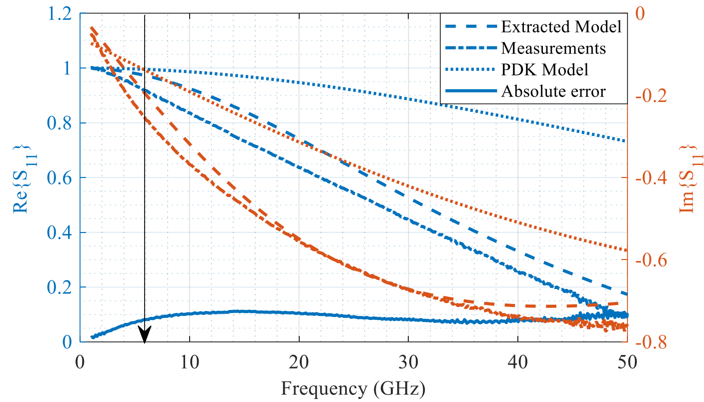

Figure 5.1: Comparison of S_{11} for the extracted model for NMOS with gate width of 5 μm to measurement and the PDK model

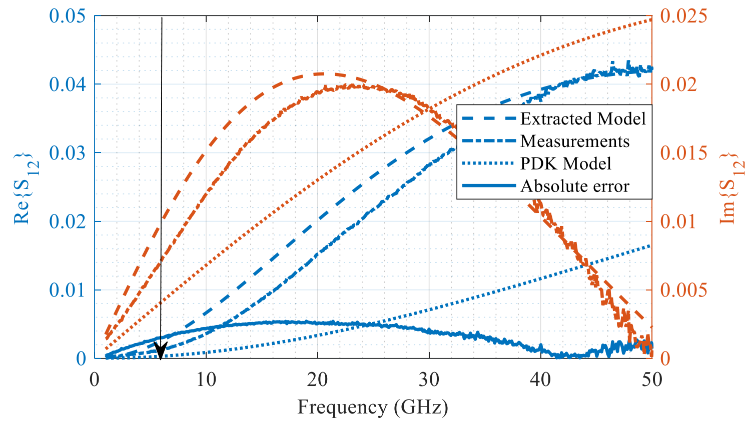

Figure 5.2: Comparison of S_{12} for the extracted model for NMOS with gate width of 5 μm to measurement and the PDK model

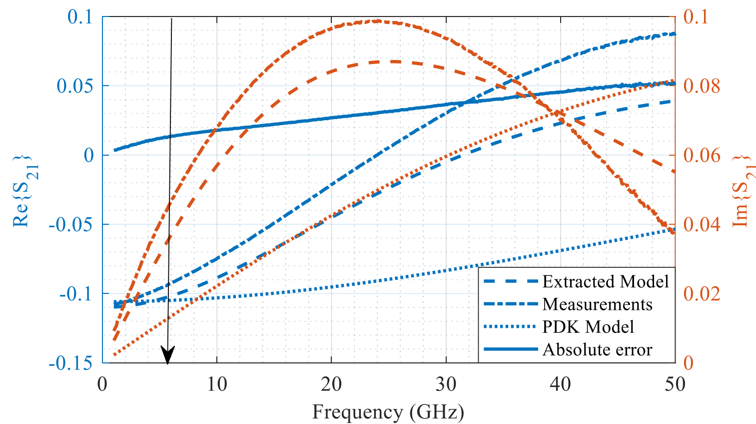

Figure 5.3: Comparison of S_{21} for the extracted model for NMOS with gate width of 5 μm to measurement and the PDK model

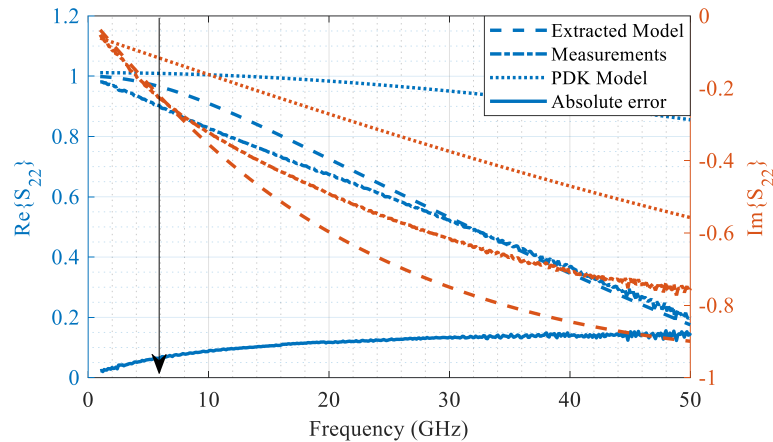

Figure 5.4: Comparison of S_{22} for the extracted model for NMOS with gate width of 5 µm to measurement and the PDK model

S-parameters from the extracted model are generally in agreement with measured S-parameters over the frequency range of interest. However, S-parameters from the model in the PDK only agree well with S-parameters from both measurement and the extracted model up to around 6 GHz. This is because the PDK model of the transistors has only been validated up to 6 GHz.

The S-parameters from the extracted model are compared to the S-parameters from measurements of the device with a gate width of 10µm, as well as compared to simulations with the PDK model to evaluate the model parameter extraction process in Figure 5.5 to Figure 5.8.

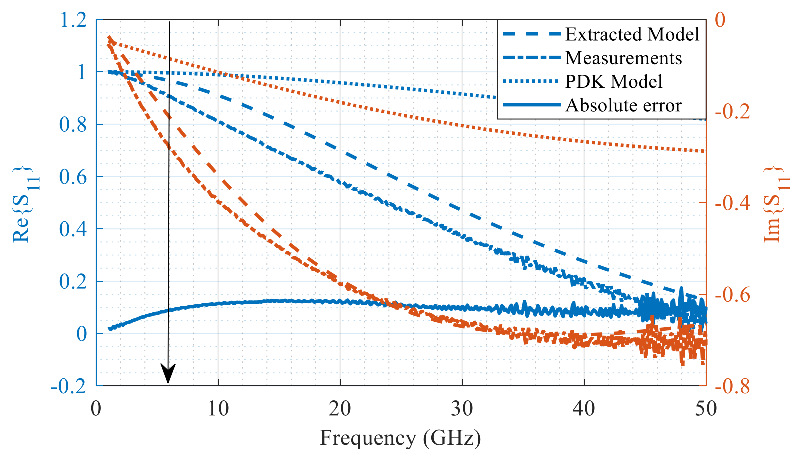

Figure 5.5: Comparison of S_{11} for the extracted model for NMOS with gate width of 10 µm to measurement and the PDK model

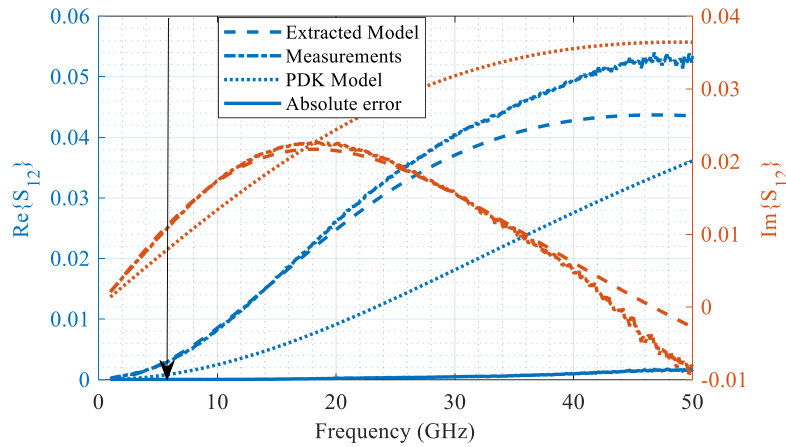

Figure 5.6: Comparison of S_{12} for the extracted model for NMOS with gate width of 10 µm to measurement and the PDK model

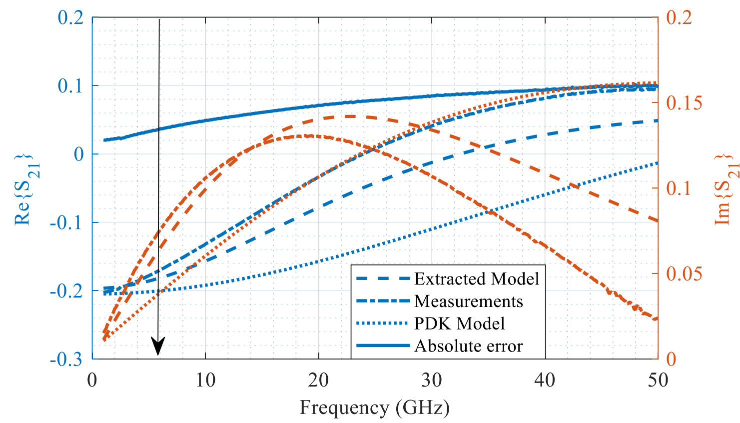

Figure 5.7: Comparison of S_{21} for the extracted model for NMOS with gate width of 10 µm to measurement and the PDK model

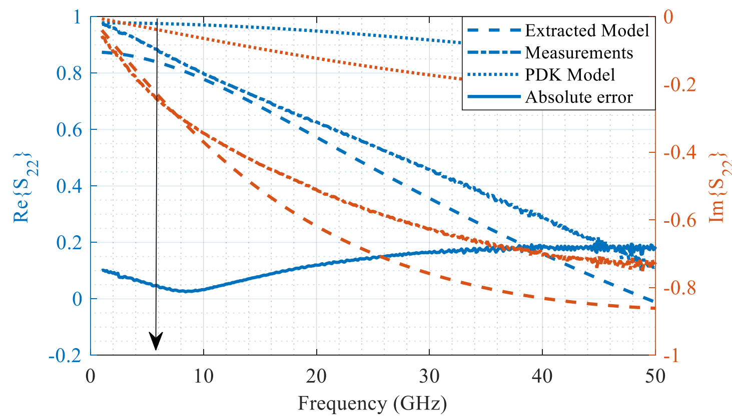

Figure 5.8: Comparison of S_{22} for the extracted model for NMOS with gate width of 10 µm to measurement and the PDK model

Again, good agreement between the S-parameters from the extracted model and the S-parameters from measurements is evident, with discrepancies between the S-parameters from the model in the PDK and the measured results above 6 GHz. On the whole, the model evidently provides better agreement to measurement results for a larger gate.

The S-parameters from the extracted model are compared to the S-parameters from measurements of the device with a gate width of 25µm, and to the simulations with the PDK model to evaluate the model parameter extraction process, in Figure 5.9 to Figure 5.12.

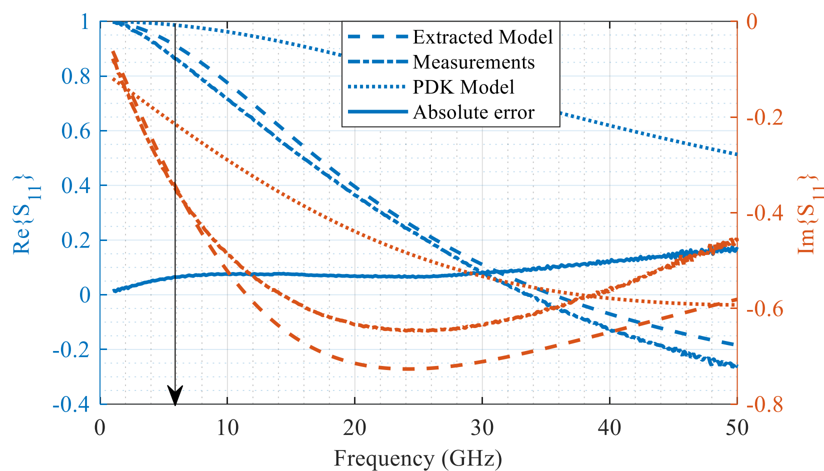

Figure 5.9: Comparison of S_{11} for the extracted model for NMOS with gate width of 25 µm to measurement and the PDK model

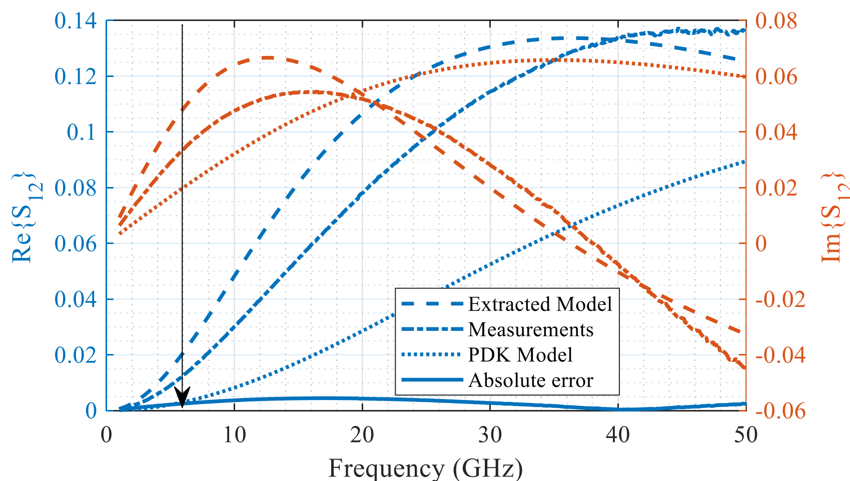

Figure 5.10: Comparison of S_{12} for the extracted model for NMOS with gate width of 25 µm to measurement and the PDK model

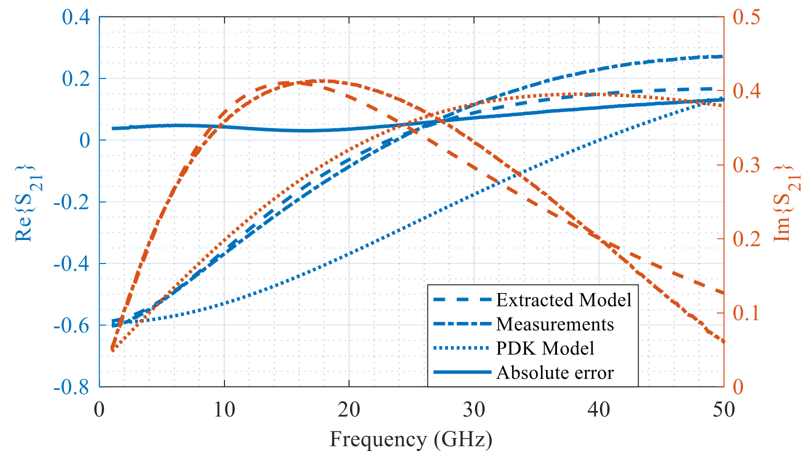

Figure 5.11: Comparison of S_{21} for the extracted model for NMOS with gate width of 25 μm to measurement and the PDK model

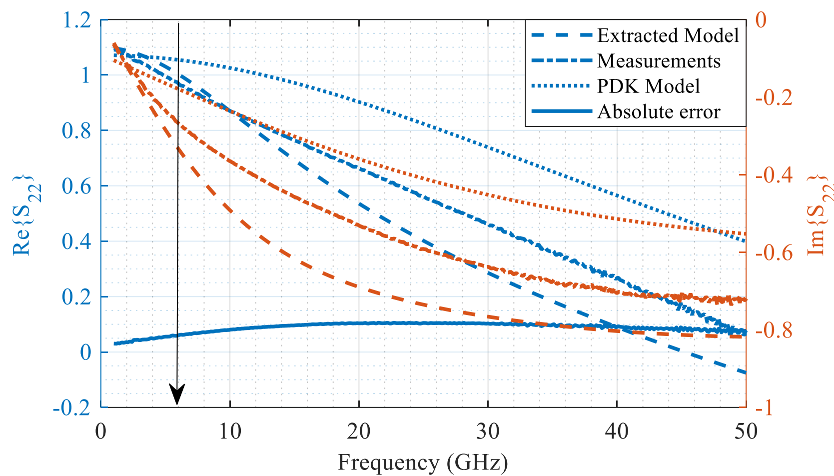

Figure 5.12: Comparison of S_{22} for the extracted model for NMOS with gate width of 25 μm to measurement and the PDK model

Similarly, for the device with a total gate width of 25 μm, the S-parameters from the extracted model agreed quite well with S-parameters from measurement, while those from the model in the PDK only showed some good agreement up to around 6 GHz.

Finally, the S-parameters from the extracted model are compared to the S-parameters from measurements of the device with a gate width of 50 μm, and to the simulations with the PDK model (to evaluate the model parameter extraction process) in Figure 5.13 to Figure 5.16.

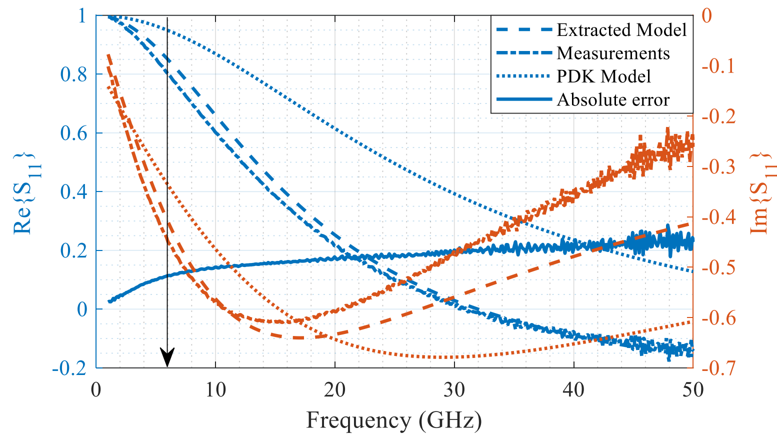

Figure 5.13: Comparison of S_{11} for the extracted model for NMOS with gate width of 50 µm to measurement and the PDK model

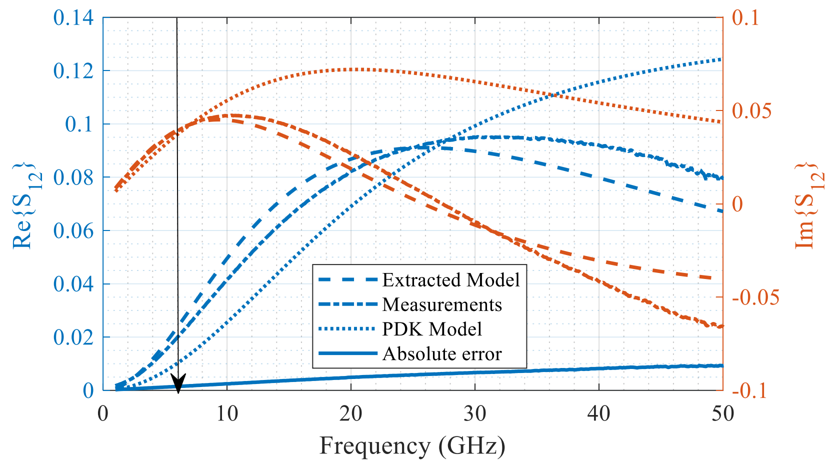

Figure 5.14: Comparison of S_{12} for the extracted model for NMOS with gate width of 50 µm to measurement and the PDK model

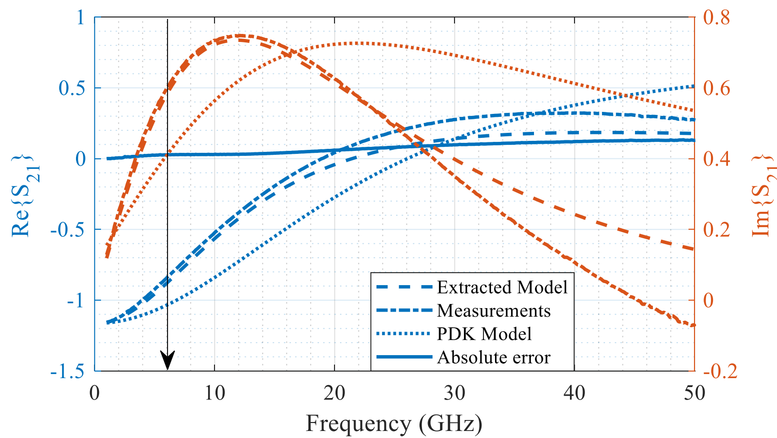

Figure 5.15: Comparison of S_{21} for the extracted model for NMOS with gate width of 50 µm to measurement and the PDK model

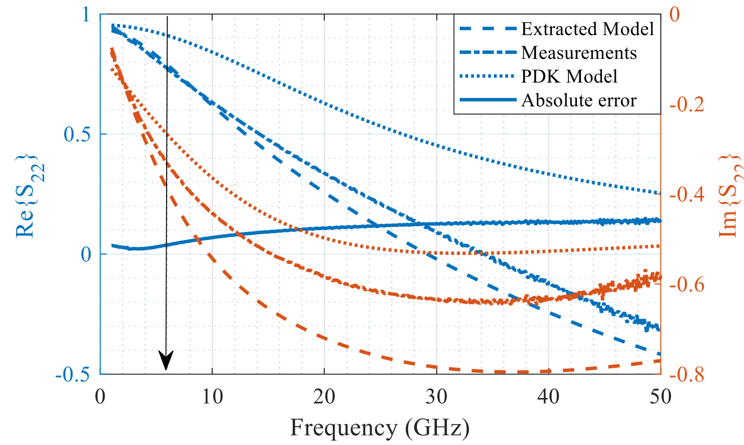

Figure 5.16: Comparison of S_{22} for the extracted model for NMOS with gate width of 50 µm to measurement and the PDK model

5.3 CURVE FITTING AND REGRESSION METHOD FOR SMALL SIGNAL PARAMETERS

The curve fitting toolbox in MATLAB is used to derive equations relating changes in the small signal model parameters (extracted from measured S-parameters and presented in Section 5.1) to *d*. The derived equations are summarised in Table 5.5 to Table 5.8.

Table 5.5: Extracted small signal parameters for the devices with total gate width of 5 µm

Small signal parameter	Derived equation	R^2
$R_g(\Omega)$	$R_g = 21.9e^{0.0000686d} - 1.986e^{-0.007131d}$	0.9973
C_{gd}(fF)	$C_{gd} = 2.782e^{0.000104d}$	0.9964
C_{gs}(fF)	$C_{gs} = 55.18e^{0.00004231d} - 4.719e^{-0.002292d}$	0.9981
g_m(mS)	$g_m = 1.099e^{-0.0000001298d} + 0.001456e^{-0.00102d}$	0.9946
$R_{ds}(\Omega)$	$R_{ds} = 852.3e^{0.000003223d} - 3.578e^{-0.002937d}$	0.9873
C_{sd}(fF)	$C_{sd} = 0.0006337e^{0.003136d} + 15.8e^{0.00009577d}$	0.9915
C_{db}(fF)	$C_{db} = 41.81e^{0.00006133d} - 0.7734e^{-0.08771d}$	0.9817
C_{bb}(fF)	$C_{bb} = 138.1e^{0.00001694d} - 2.901e^{-0.001922d}$	0.9867
$R_{bb}(\Omega)$	$R_{bb} = 37.96e^{0.00006194d} - 3.132e^{-0.002908d}$	0.9958

From Table 5.5, the minimum value of R^2 is above 0.98. This is an indication that all the derived equations fit well to the data.

Table 5.6: Extracted small signal parameters for the devices with total gate width of 10 µm

Small signal parameter	Derived equation	R^2
$R_g(\Omega)$	$R_g = 25.24e^{0.00006477d} - 1.503e^{-0.004097d}$	0.9905
C_{gd}(fF)	$C_{gd} = 63.23e^{0.000004339d} - 9.191e^{-0.000191d}$	0.9982
C_{gs}(fF)	$C_{gs} = 3.563e^{0.00004432d} - 1.486e^{-0.001614d}$	0.9687
g_m(mS)	$g_m = 2.101e^{-0.000001687d} + 0.0003177e^{-0.002717d}$	0.9900
$R_{ds}(\Omega)$	$R_{ds} = 750.8e^{0.000003277d} - 2.211e^{-0.005759d}$	0.9981
C_{sd}(fF)	$C_{sd} = 610.4e^{0.0001434d} - 586.5e^{0.0001459d}$	0.9989
C_{db}(fF)	$C_{db} = 46.13e^{0.00002586d} - 1.46e^{-0.005653d}$	0.9925
C_{bb}(fF)	$C_{bb} = 133.5e^{0.00001361d} - 0.6668e^{-0.004581d}$	0.9941
$R_{bb}(\Omega)$	$R_{bb} = 30.73e^{0.00001764d} - 0.969e^{-0.001842d}$	0.9708

All the derived model equations have their R^2 values above 0.96 as shown in Table 5.6. This signifies a good fit of the curve to data.

Table 5.7: Extracted small signal parameters for the devices with total gate width of 25 µm

Small signal parameter	Derived equation	R^2
$R_g(\Omega)$	$R_g = 17.16e^{0.0000638d} - 0.3454e^{-0.0035d}$	0.9878
C_{gd}(fF)	$C_{gd} = 18.23e^{0.000118d} - 3.596e^{-0.001858d}$	0.9932
C_{gs}(fF)	$C_{gs} = 81.14e^{0.00002456d} - 1.486e^{-0.001614d}$	0.9789
g_m(mS)	$g_m = 5.897e^{-0.000001036d} + 0.003442e^{-0.009175d}$	0.9980
$R_{ds}(\Omega)$	$R_{ds} = 667.6e^{0.00003109d} - 51.36e^{-0.000821d}$	0.9998
C_{sd}(fF)	$C_{sd} = 23.75e^{0.0001634d} - 1.805e^{-0.00251d}$	0.9996
C_{db}(fF)	$C_{db} = 52.49e^{0.0001004d} - 0.8347e^{-0.00496d}$	0.9803
C_{bb}(fF)	$C_{bb} = 57.52e^{0.00003764d} - 1.265e^{-0.00885d}$	0.9986
$R_{bb}(\Omega)$	$R_{bb} = 130.1e^{0.0001018d} - 71.09e^{-0.003286d}$	0.9981

Similarly for the NMOS with a total gate width of 25 µm, the R^2 are all above 0.96 signifying a good fit of the curves to the data.

Table 5.8: Extracted small signal parameters for the devices with total gate width of 50 µm

Small signal parameter	Derived equation	R^2
$R_g(\Omega)$	$R_g = 39.81e^{0.0003003d}$	0.9928
C_{gd}(fF)	$C_{gd} = 5.324e^{0.0001816d} - 0.66e^{0.0005212d}$	0.9974
C_{gs}(fF)	$C_{gs} = 104.6e^{0.00004238d} - 4.414e^{-0.002032d}$	0.9893
g_m(mS)	$g_m = 12.61e^{-0.00003657d}$	0.9847
$R_{ds}(\Omega)$	$R_{ds} = 665.5e^{0.00004202d} - 45.93e^{-0.002494d}$	0.9991
C_{sd}(fF)	$C_{sd} = 58.05e^{0.0000464d} - 12.38e^{-0.00022762d}$	0.9802
C_{db}(fF)	$C_{db} = 64.71e^{0.00005606d}$	0.9933
C_{bb}(fF)	$C_{bb} = 94.21e^{0.00007612d} - 3.501e^{-0.003789d}$	0.9964
$R_{bb}(\Omega)$	$R_{bb} = 76.51e^{0.00002841d} - 1.956e^{-0.004339d}$	0.9965

The equations for curves of best fit for the device with gate width of 50 µm all have R^2 above 0.98, which is a good indication of the accuracy and reliability of the derived equations.

5.4 MODEL VALIDATION AND USAGE DEMONSTRATION

To validate the model, small signal parameter values are calculated using the derived equations presented in Table 5.5 to Table 5.9.

5.4.1 Model validation and usage demonstration for the model of the NMOS device with total gate width of 5 µm

Validation and usage demonstration is performed using S-parameter from the calculated small signal parameters at a *d* of 110 krad and *d* of 1 Mrad. These are compared to S-parameters obtained from the extracted small signal parameters at a *d* of 110 krad. The

extracted and calculated small signal parameters values at a known *d* of 110 krad, as well as the calculated small signal parameter values at a *d* of 1 Mrad are shown in Table 5.9.

Table 5.9: Comparison of calculated and extracted model for NMOS with gate width of 5 µm

Small signal parameter	Extracted at 110 krad	Calculated at 110 krad	Calculated at 1 Mrad
$R_g(\Omega)$	22.62	22.51	34.84
C_{gd}(fF)	2.96	2.95	5.48
C_{gs}(fF)	55.62	55.43	73.32
g_m(mS)	1.0993	1.0995	1.0929
$R_{ds}(\Omega)$	853.99	853.45	872.96
C_{sd}(fF)	16.80	16.76	33.87
C_{db}(fF)	43.44	43.91	45.69
C_{bb}(fF)	138.87	138.82	156.10
$R_{bb}(\Omega)$	39.07	39.07	42.21
C_{dg}(fF)	2.99	2.98	3.19

The S-parameters obtained from the small signal parameters in Table 5.9 are shown in Figure 5.17 to Figure 5.20.

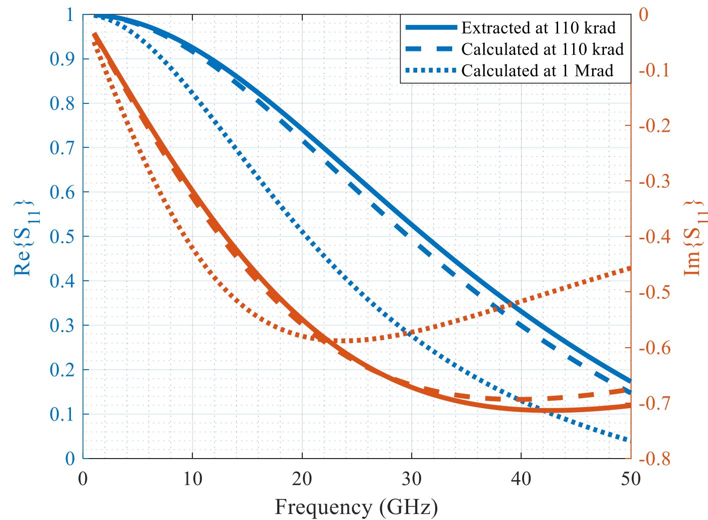

Figure 5.17: Comparison of calculated S_{11} to extracted model for NMOS with gate width of 5 µm

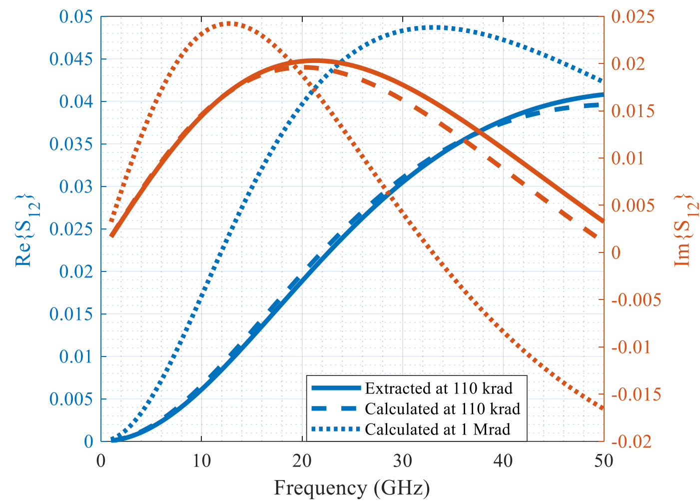

Figure 5.18: Comparison of calculated S_{12} to extracted model for NMOS with gate width of 5 µm

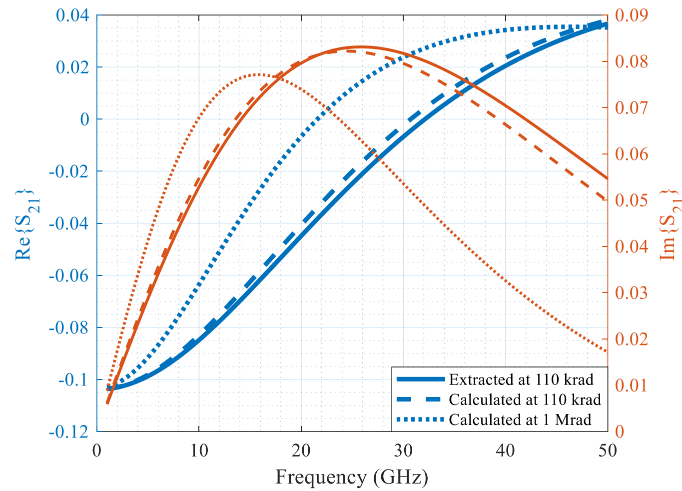

Figure 5.19: Comparison of calculated S_{21} to extracted model for NMOS with gate width of 5µm

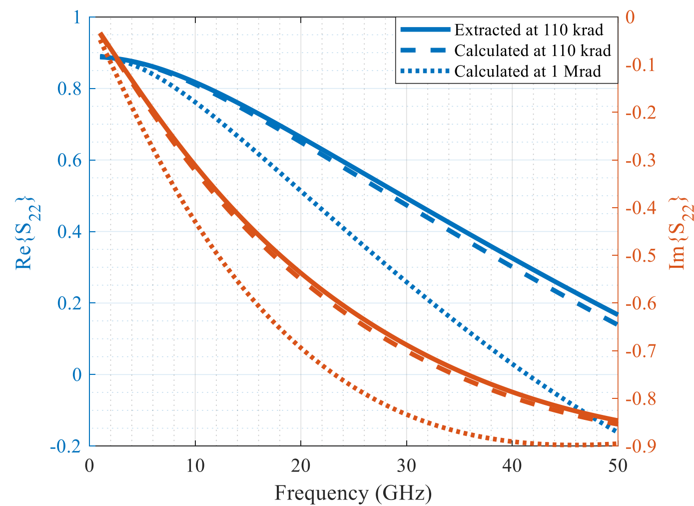

Figure 5.20: Comparison of calculated S_{22} to extracted model for NMOS with gate width of 5µm

5.4.2 Model validation and usage demonstration for the model of the NMOS device with total gate width of 10 µm

Validation and usage demonstration is performed using S-parameter from the calculated small signal parameters at a *d* of 110 krad and *d* of 1 Mrad. These are compared to S-parameters obtained from the extracted small signal parameters at a *d* of 110 krad. The extracted and calculated small signal parameters values at a known *d* of 110 krad, as well as the calculated small signal parameter values at a *d* of 1 Mrad are shown in Table 5.10.

Table 5.10: Comparison of calculated and extracted small signal model parameter values for NMOS with total gate width of 10 µm

Small signal parameter	Extracted at 110 krad	Calculated at 110 krad	Calculated at 1 Mrad
R_g(Ω)	26.13	26.14	39.31
C_{gd}(fF)	55.17	55.24	65.60
C_{gs}(fF)	3.66	3.66	4.76
g_m(mS)	2.1006	2.1008	2.0985
R_{ds}(Ω)	752.09	752.46	766.46
C_{sd}(fF)	25.05	25.06	37.11
C_{db}(fF)	46.90	46.84	54.81
C_{bb}(fF)	134.57	134.57	146.07
R_{bb}(Ω)	30.97	30.79	34.73
C_{dg}(fF)	3.61	3.61	4.96

The S-parameters obtained from the small signal parameters in Table 5.10 are shown in Figure 5.21 to Figure 5.24.

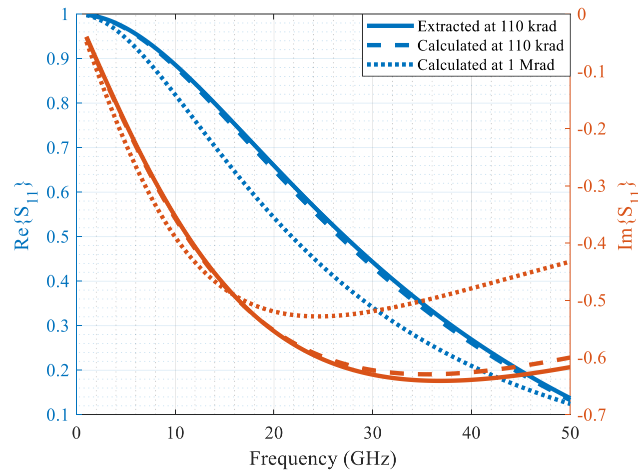

Figure 5.21: Comparison of calculated S_{11} to extracted model for NMOS with gate width of 10µm

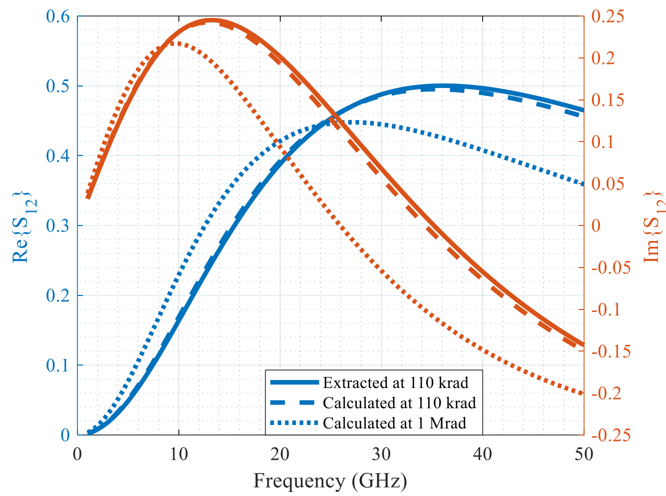

Figure 5.22: Comparison of calculated S_{12} to extracted model for NMOS with gate width of 10µm

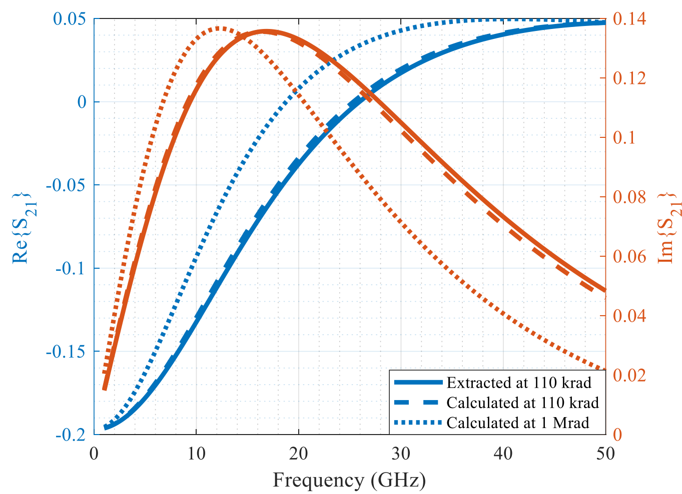

Figure 5.23: Comparison of calculated S_{21} to extracted model for NMOS with gate width of 10µm

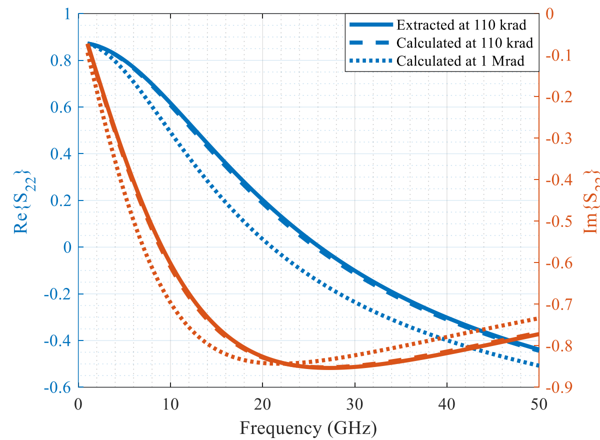

Figure 5.24: Comparison of calculated S_{22} to extracted model for NMOS with gate width of 10µm

5.4.3 Model validation and usage demonstration for the model of the NMOS device with total gate width of 25 µm

Validation and usage demonstration is performed using S-parameter from the calculated small signal parameters at a *d* of 110 krad and *d* of 1 Mrad. These are compared to S-parameters obtained from the extracted small signal parameters at a *d* of 110 krad. The extracted and calculated small signal parameters values at a known *d* of 110 krad, as well as the calculated small signal parameter values at a *d* of 1 Mrad, are shown in Table 5.11.

Table 5.11: Comparison of calculated and extracted small signal model parameter values for NMOS with total gate width of 25 µm

Small signal parameter	Extracted at 110 krad	Calculated at 110 krad	Calculated at 1 Mrad
R_g(Ω)	18.00	17.82	20.79
C_{gd}(fF)	18.08	18.01	68.44
C_{gs}(fF)	81.82	81.86	95.79
g_m(mS)	5.8927	5.8925	5.8565
R_{ds}(Ω)	648.94	649.92	850.49
C_{sd}(fF)	25.35	25.34	78.09
C_{db}(fF)	55.87	55.85	101.77
C_{bb}(fF)	58.83	58.83	73.93
R_{bb}(Ω)	129.42	130.60	281.10
C_{dg}(fF)	16.85	16.82	55.96

The S-parameters obtained from the small signal parameters in Table 5.11 are shown in Figure 5.25 to Figure 5.28.

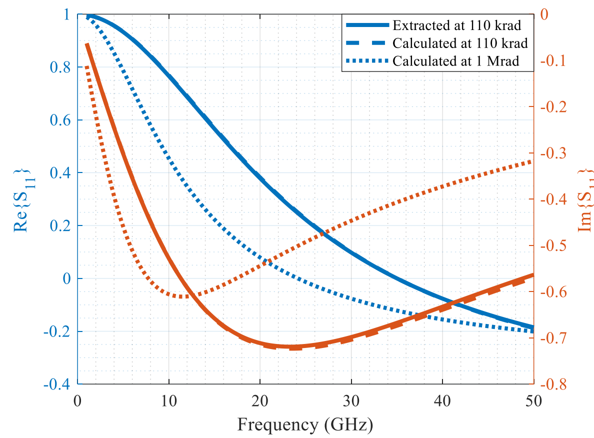

Figure 5.25: Comparison of calculated S_{11} to extracted model for NMOS with gate width of 25µm

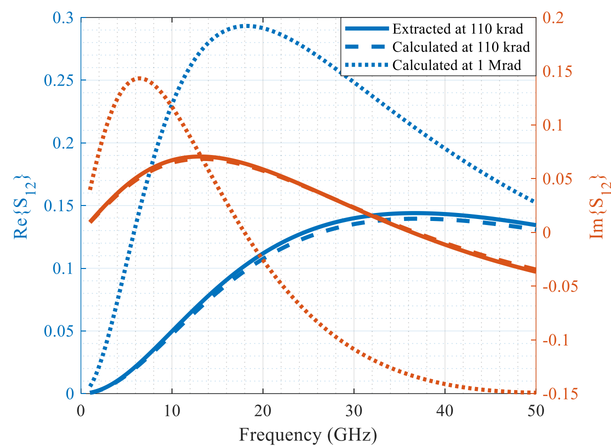

Figure 5.26: Comparison of calculated S_{12} to extracted model for NMOS with gate width of 25µm

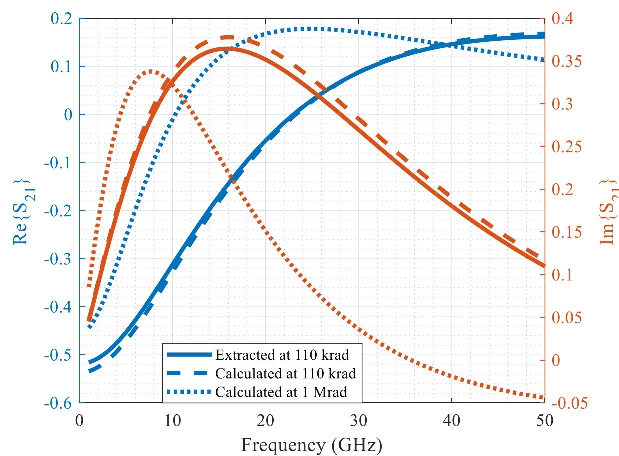

Figure 5.27: Comparison of calculated S_{21} to extracted model for NMOS with gate width of 25µm

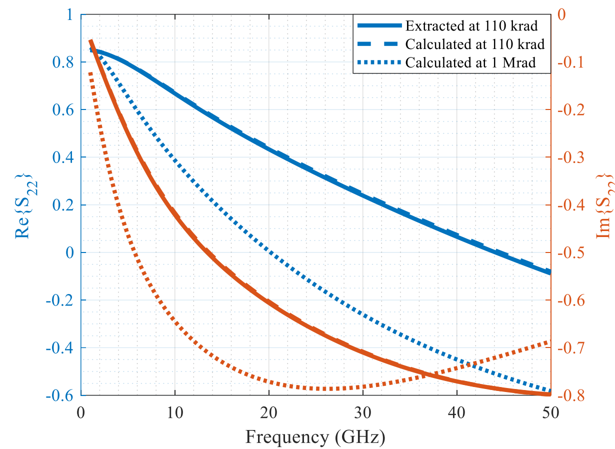

Figure 5.28: Comparison of calculated S_{22} to extracted model for NMOS with gate width of 25μm

5.4.4 Model validation and usage demonstration for the model of the NMOS device with total gate width of 50 μm

Validation and usage demonstration is performed using S-parameter from the calculated small signal parameters at a *d* of 110 krad and *d* of 1 Mrad. These are compared to S-parameters obtained from the extracted small signal parameters at a *d* of 110 krad. The extracted and calculated small signal parameters values at a known *d* of 110 krad, as well as the calculated small signal parameter values at a *d* of 1 Mrad, are shown in Table 5.12.

Table 5.12: Comparison of calculated and extracted small signal model parameter values for NMOS with total gate width of 50 μm

Small signal parameter	Extracted at 110 krad	Calculated at 110 krad	Calculated at 1 Mrad
R_g(Ω)	48.20	48.47	170.94
C_{gd}(fF)	4.92	5.04	11.12
C_{gs}(fF)	106.95	106.98	139.91
g_m(S)	0.012989	0.012600	0.012300
R_{ds}(Ω)	673.78	673.98	901.99
C_{sd}(fF)	49.10	49.11	76.54
C_{db}(fF)	67.11	67.00	92.48
C_{bb}(fF)	98.52	98.46	156.64
R_{bb}(Ω)	77.52	77.75	92.56
C_{dg}(fF)	68.99	68.62	151.29

The S-parameters obtained from the small signal parameters in Table 5.12 are shown in Figure 5.29 to Figure 5.32.

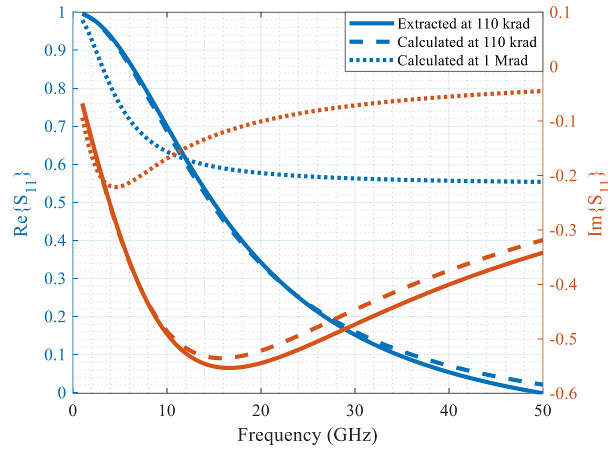

Figure 5.29: Comparison of calculated S_{11} to extracted model for NMOS with gate width of 50μm

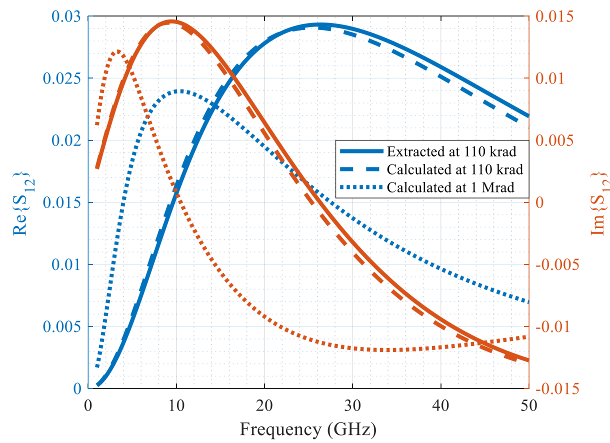

Figure 5.30: Comparison of calculated S_{12} to extracted model for NMOS with gate width of 50μm

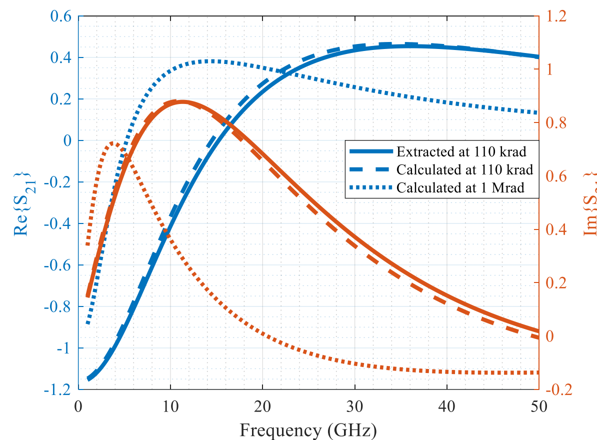

Figure 5.31: Comparison of calculated S_{21} to extracted model for NMOS with gate width of 50μm

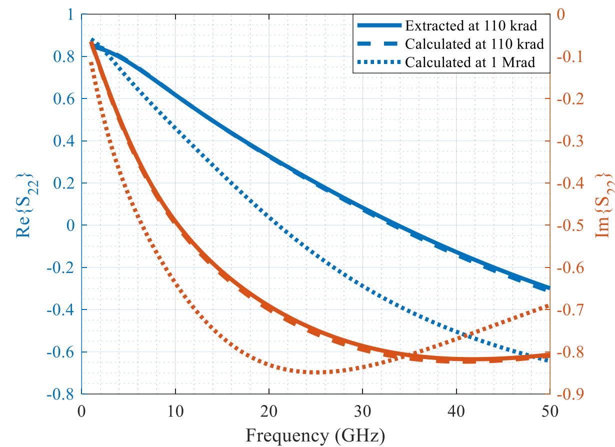

Figure 5.32: Comparison of calculated S_{22} to extracted model for NMOS with gate width of 50µm

5.5 CHAPTER SUMMARY

The chapter has presented the small signal model parameters extracted from measured S-parameters pre- and post-irradiation for the four bulk CMOS devices. A comparison of S-parameters from the extracted model to S-parameters from measurements and S-parameters from simulations with the PDK model was also presented. The chapter subsequently presented derived equations relating each of the small signal model parameters to *d* and concluded with a validation of these equation and their ability to predict the performance of the devices when exposed to extreme radiation doses. It was found that the S-parameter simulation using small signal circuit component values calculated from the fitted model equations generally agree very well with original the extracted model based on measurements. Furthermore, it was found that resistance and capacitance values generally increased with increase in *d* while the values of g_m reduced with increase in *d*.

CHAPTER 6 DISCUSSION

This chapter will discuss the underlying physical interpretation of the observed changes in the models for both SiGe HBT and bulk CMOS devices, and present an error analysis of the derived equations relating small signal parameters to radiation dose.

6.1 PHYSICAL INTERPRETATION OF MODEL CHANGES IN SiGe HBT

From Chapter 4, it was observed that the resistance and capacitance values of the small signal circuit model generally increased with increase in radiation, while g_m generally decreased with increase in *d.* This trend can be attributed to the manner in which ionizing radiation damages the semiconductor dielectric interface. The most susceptible regions to TID damage are the emitter-base (EB) spacer region (separating the base and emitter [3]), which is modelled by R_{bx}, R_{bi}, C_{be}, C_{bep} R_{be} and g_m, and the interface region at the edge of the shallow trench isolation (STI) (which is associated with the collector-base (CB) and substrate junctions [3]) and is modelled by the parameters C_{bc}, R_s, and C_{cso}. Ionizing radiation damages these interfaces in the following ways:

a) By producing traps which act as recombination and generation (G/R) centers. These G/R centers change the operating point of the SiGe HBT.
b) By inducing incomplete bonding at the surfaces of the dielectric.
c) Through the displacement of the host atom in the lattice, thereby producing defects or traps.

The consequence of the produced defects or traps in the EB region is an increase in the resistivity and, hence, an increase in R_{bx}, R_{be}, and $R_{bi.}$ This, in turn, results in the modest increase of the base current. The presence of traps

cause structural modifications in the material leading to an increase in the dielectric constant (ε_r) [4], increasing the EB junction capacitances C_{be} and C_{bep} as

$$C = \frac{\varepsilon_r \varepsilon_o A}{t} \tag{6.1}$$

where ε_r is the dielectric constant, ε_o is the vacuum permittivity, A is the base area while t is the EB junction thickness. Similarly, the capacitances C_{bc} and C_{cso} increase with increase in d.

6.2 IMPACT OF RADIATION ON THE PERFORMANCE OF SiGe HBT

Changes in the small signal model parameters presented in Table 4.1 up to 2400 krad were minimal. This is a further confirmation of the inbuilt tolerance of SiGe to radiation damage also reported in previous research studies [3]. The devices are, therefore, expected to operate well up to high values of d such as the ones expected over a satellite's lifetime.

To evaluate the impact of TID on the transistor's performance, the modelled S_{11}, S_{22} unilateral gain (U), magnitude of S_{21}, forward current gain (A_i), f_T, f_{max} and the modelled NF are considered pre- and post-irradiation.

The Smith Chart for S_{11} is presented in Figure 6.1 to evaluate the impact of radiation on the performance of SiGe HBT.

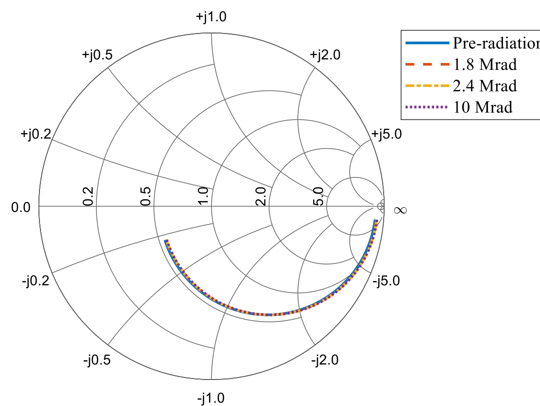

Figure 6.1: Modelled Smith Chart presentation of S_{11} at various values of d

It is evident from Figure 6.1 (reading the curves clockwise from low to high frequencies) that there is a minimal change in S_{11}, which is indicative of the inbuilt tolerance of SiGe HBT to TID. The minimal change in S_{11} is also an indication that there is no significant input mismatch caused by TID if the device is designed to be matched at *d* of 10 Mrad. It is also clear that S_{11} becomes resistive as the device's exposure to TID is increased.

The Smith Chart for S_{22} is presented in Figure 6.2 to further evaluate the impact of radiation on the performance of SiGe HBT.

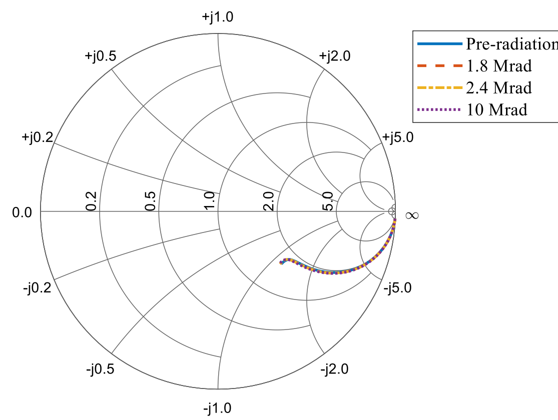

Figure 6.2: Modelled Smith Chart presentation of S_{22} at various values of *d*

It is shown in Figure 6.2 that there are insignificant changes in S_{22} (reading the curves clockwise from low to high frequencies) up to *d* of 10 Mrad signifying the tolerance of SiGe to TID.

The performance of the SiGe HBT under TID exposure is further analyzed using *U*. This is a figure of merit used to measure of the activity of the transistor and is defined as [36],

$$U = \frac{\left| y_{21} - y_{12} \right|^2}{4\left[\mathrm{Re}(y_{11})\mathrm{Re}(y_{22}) - \mathrm{Re}(y_{12})\mathrm{Re}(y_{21})\right]} \quad (6.3)$$

If $U > 1$, the device is considered active and considered passive otherwise.

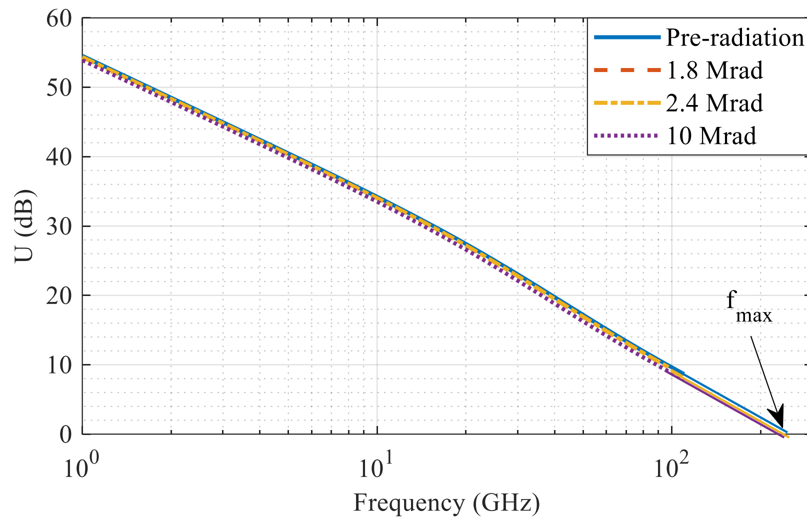

Figure 6.3: Modelled unilateral gain of the transistor at various values of *d*

There is a minor reduction in values of *U* after radiation, signifying the resilience of SiGe HBT to damage when exposed to TID. Figure 6.3 has also shows that the device's f_{max} changes from about 204.6 GHz pre-radiation to about 201.1 GHz after exposure to a *d* of 10 Mrad, a change which is not very significant further comfirming the resilience of SiGe HBTs to TID.

$|S_{21}|$, is evaluated pre-and post-radiation, to analyze the impact of radiation on the performance of the transistor in Figure 6.4.

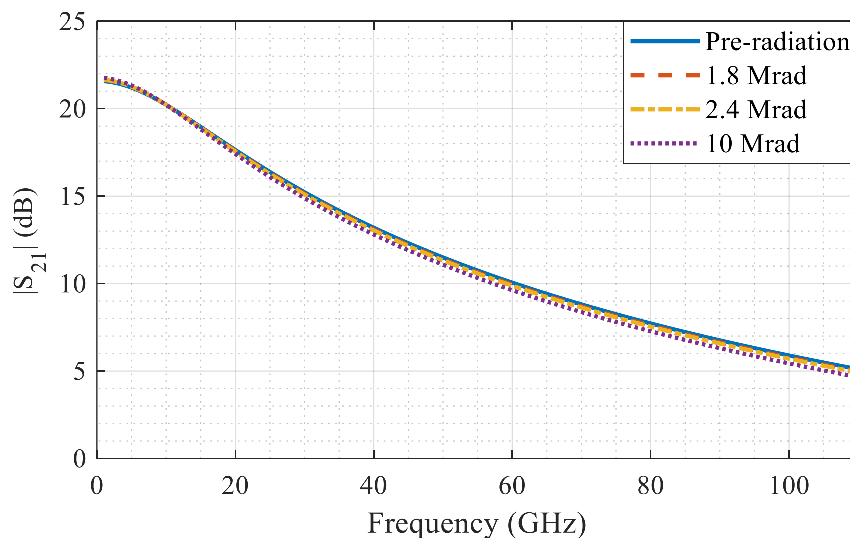

Figure 6.4: Modelled $|S_{21}|$ at various values of *d*

The data presented in Figure 6.4 clearly indicate a reduction in $|S_{21}|$ with increase in the device's exposure to TID. However, the decrease in $|S_{21}|$ is minimal, signifying an inbuilt tolerance to TID of SiGe HBT up to 10 Mrad.

To further evaluate the impact of radiation on the transistor, $|A_i|$ is analyzed pre-and post-radiation in Figure 6.5.

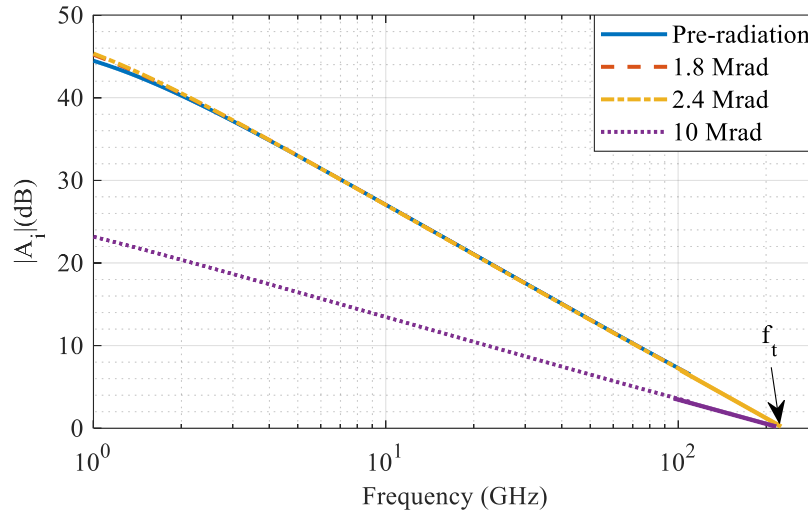

Figure 6.5: Modelled forward current gain at various values of *d*

It is clear that $|A_i|$ is minimally affected by radiation up to *d* of 2.4 Mrad indicative of the natural tolerance of SiGe HBT to TID. Similarly, the 0 dB extrapolation shows that there are insignificant changes in f_t up to a *d* of 2.4 Mrad. It is however shown that f_t reduces to 222 GHz at a *d* of 10 Mrad from 226 GHz pre-radiation. The change in roll-off slope from the expected -20 dB/decade to -10 dB/decade is an unexpected result, and may be the result of imperfect extrapolation. This should be verified by extrapolating from a dataset with larger experimental values of total dose.

The impact of TID on the performance of SiGe can also be evaluated through noise modelling. To this end, the modelled *NF* at various values of *d* are presented in Figure 6.6

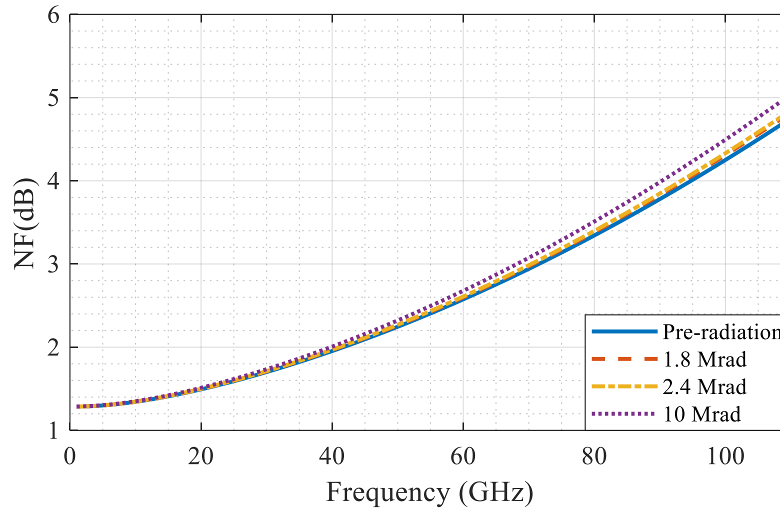

Figure 6.6: Modelled noise figure at various values of *d*

As shown in Figure 6.10, the model indicate minimal changes in *NF* pre-and post-radiation up to a *d* of 7.5 Mrad, and a sharp increase in *NF* at a *d* of 10 Mrad. This confirms the inbuilt resilience of SiGe HBT against TID. It further proves that despite this inbuilt resilience to TID, SiGe HBTs are expected to fail after exposure to high *d*. The increase in *NF* after a *d* of 10 Mrad, can be attributed to the increase in both thermal and shot noise due to high doses of radiation. As shown in Section 4.1, radiation causes an increase in the base resistance leading to an increase in the thermal noise, ultimately increasing *NF*. It therefore follows that the noise performance of the transistor is significantly affected by TID.

6.3 PHYSICAL INTERPRETATION OF MODEL CHANGES IN BULK CMOS DEVICES

Ionizing radiation can cause damage to bulk CMOS devices through the production of an electron hole pair in the gate oxide. While the electrons are usually quickly swept out of the oxide, holes travel through polaron-hopping to the interfaces where they get trapped by interface states. The trapped charges can shift the threshold voltage, increasing R_g and reducing g_m. Trapped charges can further cause a reduction in the mobility of the device and an increase in the surface resistivity in the lightly doped drain [28]. An increase in the surface resistivity of the drain leads to an increase in R_{ds} and R_{bb}.

Furthermore, through displacement of atoms in both Si and in the oxide, ionizing radiation can generate oxide and interface traps leading to an increase in the oxide and interface trap charge densities. This can cause structural modification in the material by increasing the dielectric constant, and eventually increasing the gate oxide capacitance (C_{gs} and C_{gd}) and the drain source interface capacitance (C_{db}, C_{bb}, and C_{sd}) as indicated in [42].

6.4 IMPACT OF RADIATION ON THE PERFORMANCE OF CMOS DEVICES

Changes in the small signal model parameters for bulk CMOS devices due to TID were presented in Table 5.1 to 5.4 up to 430 krad. To gain further insight into the changes caused by model variations the Smith Chart for S_{11}, the Smith Chart for S_{22}, U, the magnitude of S_{21}, $|A_i|$, f_T, and f_{max} are considered pre-and post-radiation for each of the four different devices.

6.4.1 Impact of radiation on NMOS device with total gate width of 5 µm

The impact of TID on the NMOS device with a total gate width of 5 µm is presented.

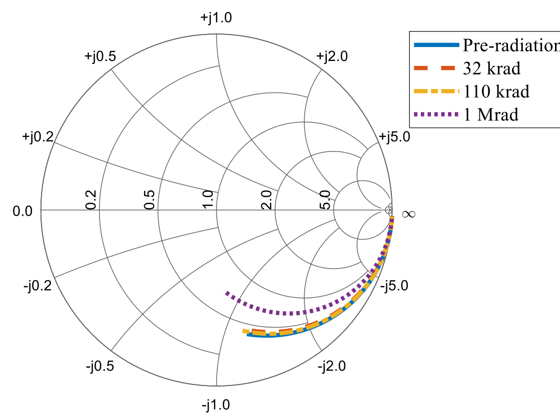

Figure 6.7: Smith Chart for S_{11}at various values of *d* for the device with gate width of 5µm

It is evident from Figure 6.7 (reading the curves clockwise from low to high frequencies) that S_{11} becomes more resistive and less capacitive with increase in *d.* Alterations are thus vital in the input matching network due to TID induced changes in the input impedance.

The impact of TID on the performance of the NMOS device with gate width of 5 µm is further evaluated by analyzing S_{22} on a Smith Chart shown in Figure 6.8.

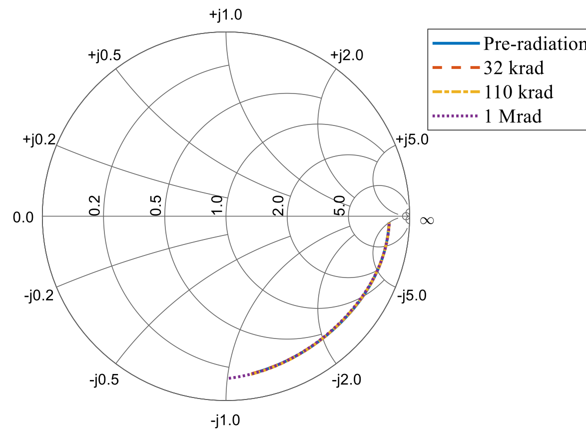

Figure 6.8: Smith Chart for S_{22} at various values of *d* for the device with gate width of 5µm

There is no significant change observed in S_{22} with increase in *d*, therefore, the output matching network does not require changes after radiation up to a *d* of 430 krad. At a d of 1 Mrad, some minimal change is observed in S_{22} suggesting damage due to TID. It therefore implies that the output impedance matching network will require slight adjustment when the device is exposed to a *d* of 1 Mrad.

To further evaluate the performance of the device pre-and post-radiation for the NMOS device with a total gate width of 5 µm, *U* is analyzed in Figure 6.9.

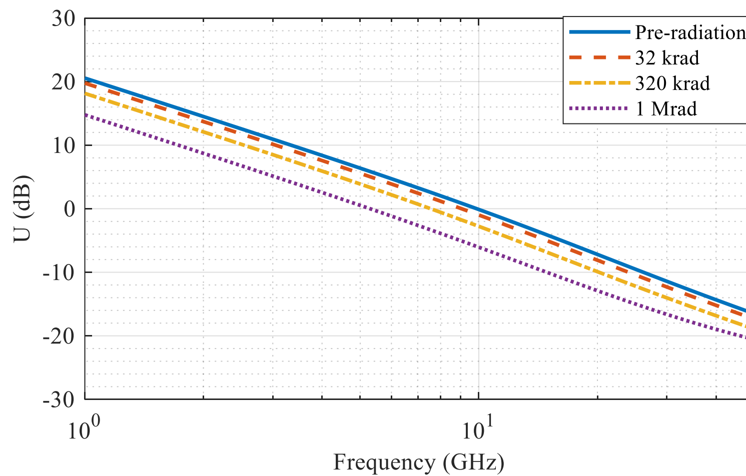

Figure 6.9: Unilateral gain at various *d* values for NMOS device with gate width of 5 µm

It is shown in Figure 6.9 that U reduces with increase in *d* and that the 0 dB intercept of the device reduces signifying reduction of the f_{max} of the device due to TID.

The impact of radiation on the performance of the NMOS device is further analyzed using $|S_{21}|$ in Figure 6.10.

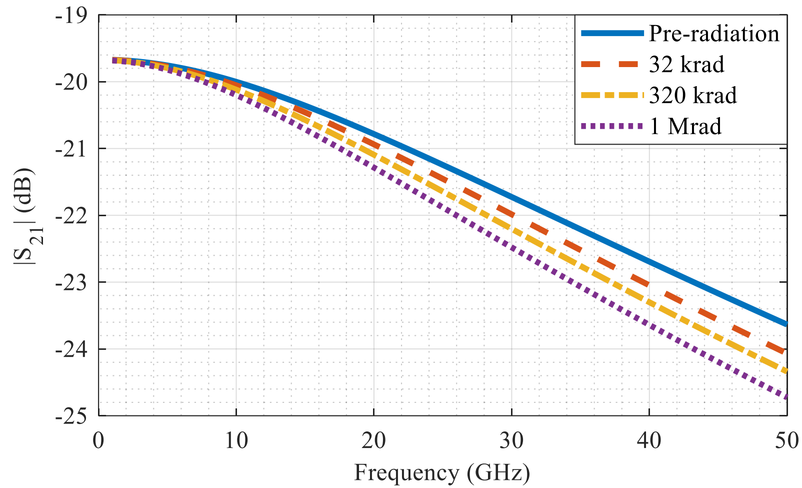

Figure 6.10: $|S_{21}|$ at various *d* values for NMOS device with gate width of 5 µm

The pre-and post-radiated values of $|S_{21}|$ are all negative, as shown in Figure 6.10. Furthermore, it is evident that $|S_{21}|$ reduces with increase in *d*, as expected.

To further evaluate the impact of radiation on the performance of the device, $|A_i|$ is analyzed pre-and post-radiation in Figure 6.11.

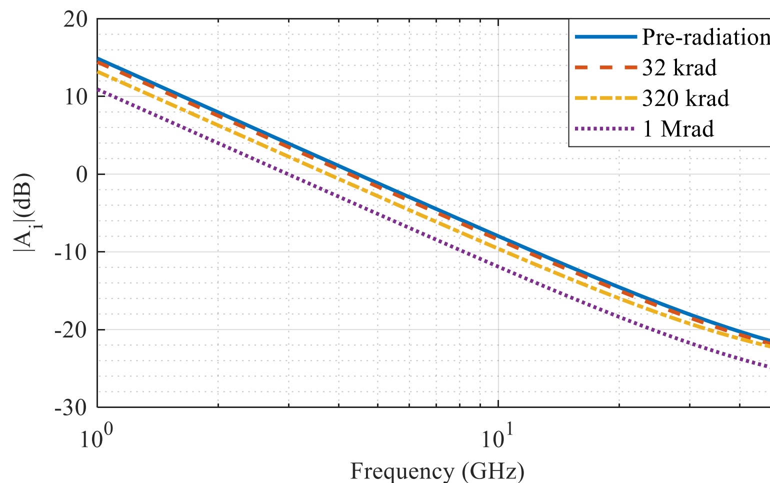

Figure 6.11: $|A_i|$ at various *d* values for NMOS device with gate width of 5 µm

A reduction in $|A_i|$ with increase in d has been shown in Figure 6.11. It is also clear that the reduction in $|A_i|$ is more at lower frequencies that at higher frequencies.

The pre-and post-radiation f_t and f_{max} for the device are analyzed to evaluate the impact of TID on the NMOS device with a total gate width of 5 µm. f_T is obtained from the 0 dB intercept in Figure 6.11 whereas f_{max} is obtained the 0 dB intercept in Figure 6.9.

The pre-and post-radiation f_t and f_{max} are summarized in Table 6.1.

Table 6.1: f_t and $f$max pre-and post-radiation

Radiation dose (*d*)	**f_t (GHz)**	**f_{max} (GHz)**
Pre-radiation	3.30	10.3
32 krad	3.15	9.40
110 krad	3.00	9.20
210 krad	2.90	8.25
320 krad	2.78	7.70
430 krad	2.70	7.50
1 Mrad	2.20	5.50

It is clear from Table 6.2 that both f_t and f_{max} reduce with increase in d as expected.

6.4.2 Impact of radiation on NMOS device with total gate width of 10 µm

The impact of TID on the input match network of the NMOS device with total gate width of 10 µm is analyzed using the Smith Chart of S_{11} in Figure 6.12.

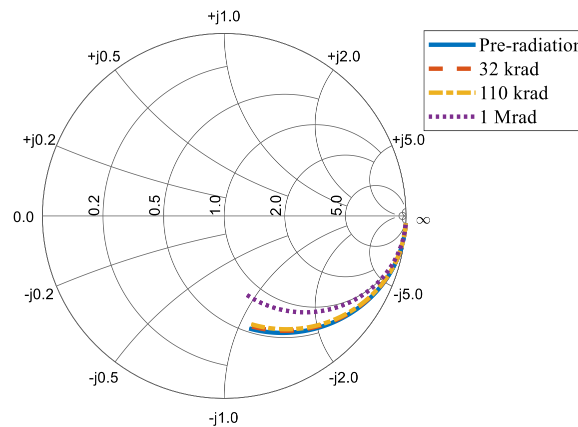

Figure 6.12: Smith Chart for S_{11} at various *d* values for NMOS device with gate width of 10 µm

It is evident that an increase in *d* significantly affects S_{11} by causing it to be more resistive an ultimately altering the input impedance as shown in Figure 6.12. It therefore follows that the input impedance matching network must be altered as the device is exposed to incremental TID to carter for the increased resistance.

The Smith Chart for S_{22} is also analyzed to evaluate the impact of TID on the performance of the NMOS device with total gate width of 10 µm in Figure 6.13.

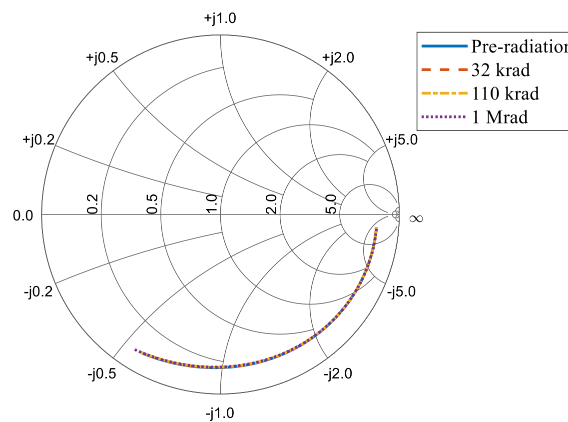

Figure 6.13: Smith Chart for S_{22} at various *d* values for NMOS device with gate width of 10 µm

It has been shown that there is no significant change in the output impedance with increase in TID. There are no alterations required in the output impedance matching network.

The performance of the device is analyzed pre-and post-radiation using U in Figure 6.14

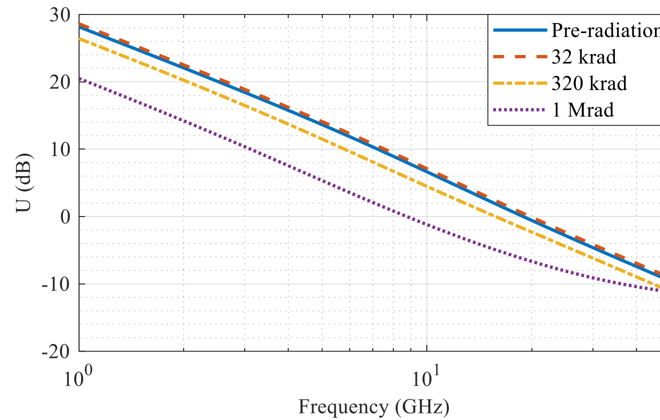

Figure 6.14: Unilateral gain at various d values for NMOS device with gate width of 10 µm

It is evident that U reduces with increase in d and also that the 0 dB intercept reduces with increase in d signifying reduction of f_{max} as the device gets exposed to TID as expected.

To further evaluate the impact of TID on the performance of NMOS device with total gate width of 10 µm, $|S_{21}|$ is analyzed pre-and post-radiation.

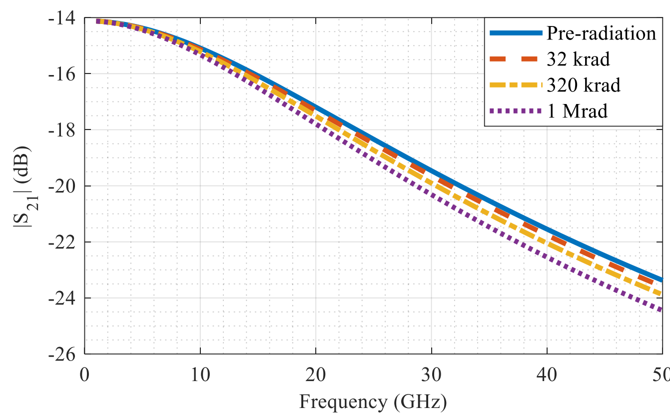

Figure 6.15: $|S_{21}|$ at various d values for NMOS device with gate width of 10 µm

From Figure 6.15, $|S_{21}|$ is negative for the device with total gate width of 10 µm in the frequency range of interest, pre-and post-radiation. Furthermore, it is clear that $|S_{21}|$ reduces as d is increased.

The impact of TID on the performance of the NMOS device is further evaluated by analyzing $|A_i|$ pre-and post-radiation in Figure 6.16.

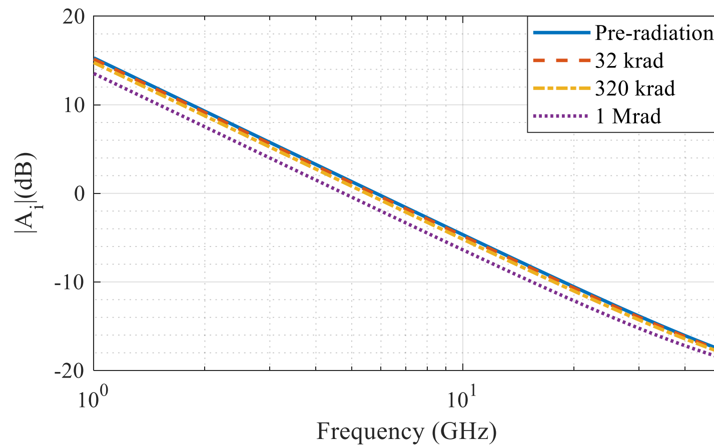

Figure 6.16: $|A_i|$ at various d values for NMOS device with gate width of 10 µm

From Figure 6.16, it is clear that $|A_i|$ reduces with increase in d signifying damage on the device due to TID. It is also clear that f_t reduces with increase in d as shown from the 0 dB intercept in Figure 6.16.

The values of f_t obtained from Figure 6.16 and the values of f_{max} obtained from Figure 6.14 pre-and post-radiation are shown in Table 6.2.

Table 6.2: Pre-and post-radiation values of f_t and f_{max} for a device with gate width of 10 µm

Radiation dose (*d*)	**f_t (GHz)**	**f_{max} (GHz)**
Pre-radiation	10.05	20.43
32 krad	9.71	19.82
110 krad	8.98	18.44
210 krad	8.27	16.97
320 krad	7.85	15.75
430 krad	7.07	14.00
1 Mrad	4.82	8.76

It is clear from Table 6.3 that both f_t and f_{max} reduce with increase in d signifying reduced performance of the device with increase in TID exposure.

6.4.3 Impact of radiation on NMOS device with total gate width of 25 µm

The impact of TID on the input impedance matching of the NMOS device with a total gate width of 25 is analyzed using the Smith Chart of S_{11} in Figure 6.17.

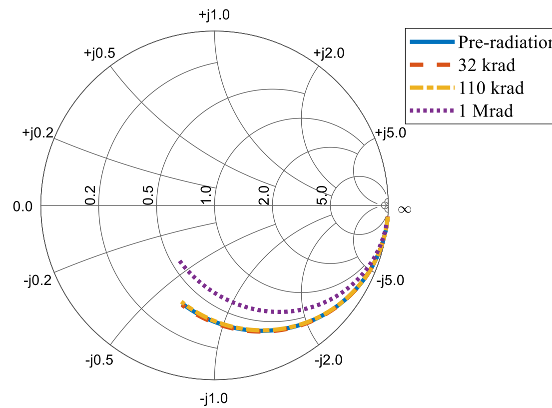

Figure 6.17: Smith Chart for S_{11} at various *d* values for NMOS device with gate width of 25 µm

The input impedance mismatch is shown on the Smith Chart in Figure 6.17 where S_{11} becomes more resistive as the device's exposure to TID is increased. This implies that the input impedance matching network requires alteration as the device is exposed to incremental TID.

The impact of TID on the output impedance is also analyzed using the Smith Chart for S_{22} in Figure 6.18.

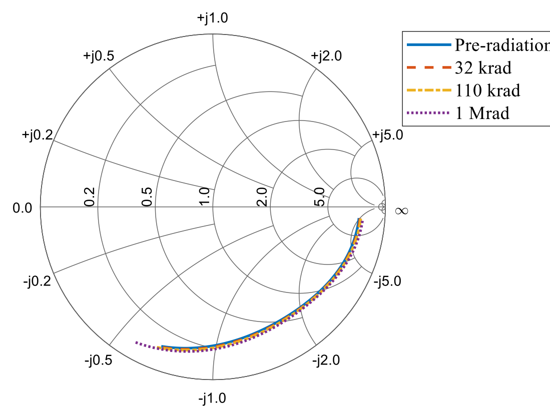

Figure 6.18: Smith Chart for S_{22} at various *d* values for NMOS device with gate width of 25 µm

A minor change in S_{22} is evident from the Smith Chart presented in Figure 6.18, signifying the changes in the output impedance as a result of the device's exposure to TID. It follows that modifications in the output impedance matching network may be required as the device's exposure to TID is increased.

The impact of TID on the activity of the NMOS device with total gate width of 25 μm is analyzed using the graphs of *U* in Figure 6.19.

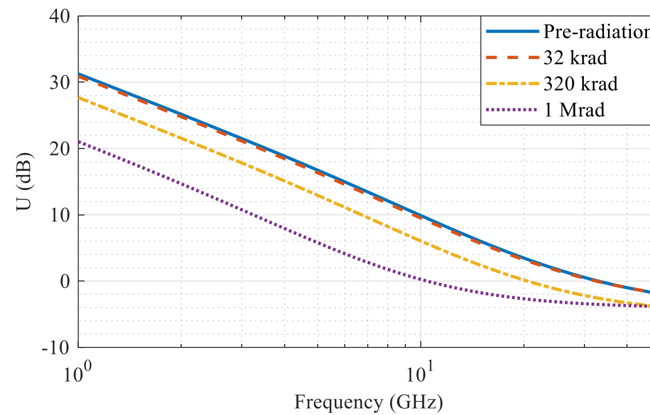

Figure 6.19: Unilateral gain at various *d* values for NMOS device with gate width of 25 μm

It is evident from Figure 6.19 reduces with increase in exposure to TID. Furthermore the 0 dB intercept for the device reduces with increase in d signifying a reduction in the f_{max} of the device with increase in exposure to TID.

The $|S_{21}|$ of the device is next analyzed pre-and post-radiation to evaluate the impact of TID on the performance of the NMOS with total gate width of 25 μm in Figure 6.20.

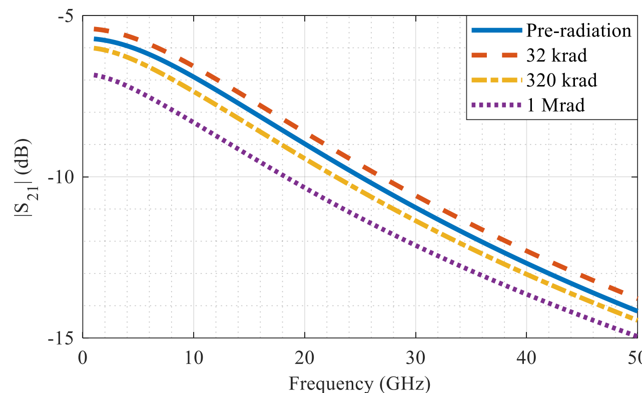

Figure 6.20: $|S_{21}|$ at various *d* values for NMOS device with gate width of 25 μm

It is evident that $|S_{21}|$ reduces with increase in d as shown in Figure 6.20, signifying reduced performance of the device due to damage caused by TID as expected.

The impact of TID is further analyzed with $|A_i|$, pre-and post-radiation shown in Figure 6.21.

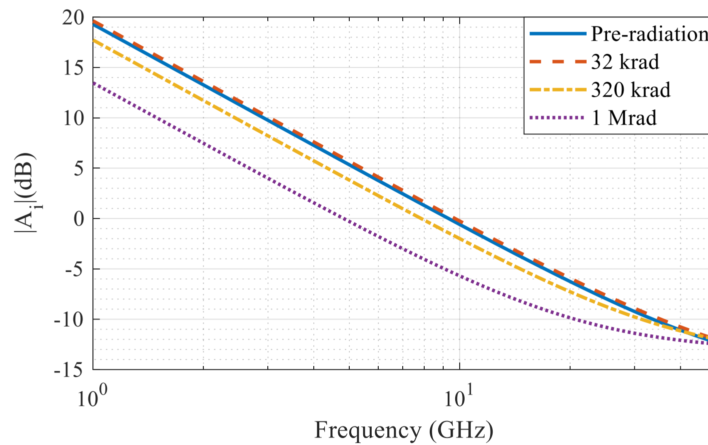

Figure 6.21: $|A_i|$ at various d values for NMOS device with gate width of 25 µm

It has been shown than $|A_i|$ reduces with increase in d. The 0 dB intercept also reduces with increase in d signifying a reduction in the f_t of the device as it gets exposed to TID.

The impact of TID on the performance of the NMOS device with gate width of 25 µm is also analyzed using the pre-and post-radiation values of f_t obtained from the 0 dB intercept of Figure 6.21 and f_{max} obtained from the 0 dB intercept of Figure 6.19 which are shown in Table 6.3.

Table 6.3: Pre-and post-radiation values of f_t and f_{max} for a device with gate width of 25 µm

Radiation dose (d)	**f_t (GHz)**	**f_{max} (GHz)**
Pre-radiation	14.67	32.98
32 krad	14.42	32.53
110 krad	13.23	29.42
210 krad	12.66	24.32
320 krad	12.01	20.50
430 krad	11.28	18.94
1 Mrad	5.09	10.43

The values of both f_t and f_{max} reduce with increase in d as shown in Table 6.3 signifying the reduced performance of the NMOS device caused by TID. This agree with previous research findings which have suggested similar trends.

6.4.4 Impact of radiation on NMOS device with total gate width of 50 µm

The impact of TID on the input impedance matching conditions for the NMOS device with gate width of 50 µm is analyzed pre-and post-radiation. To this end, the Smith Chart for S_{11} is analyze pre-and post-radiation in Figure 6.22.

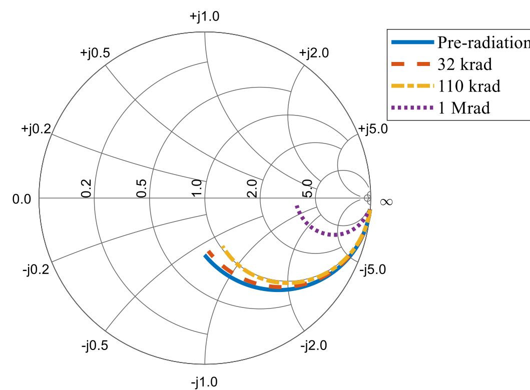

Figure 6.22: Smith Chart for S_{11} at various d values for NMOS device with gate width of 50 µm

The data presented on the Smith Chart (reading the curves in a clockwise direction from low to high frequencies) in Figure 6.22 indicate a significant change in the input impedance conditions with S_{11} becoming more resistive with increase in d. This implies that the input impedance matching network requires alteration as the device is exposed to incremental TID.

The impact of TID on the output impedance is analyzed using the Smith Chart of S_{22} in Figure 6.23.

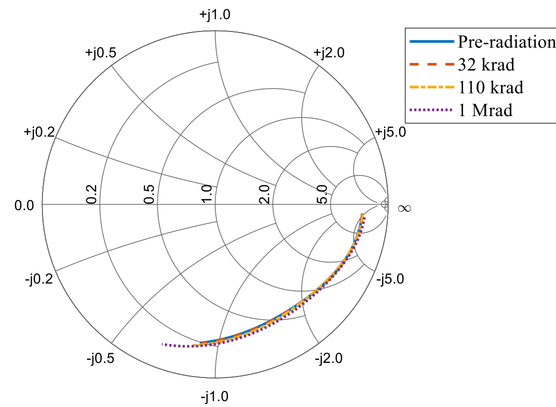

Figure 6.23: Smith Chart for S_{22} at various d values for NMOS device with gate width of 50 µm

A minor change in S_{22} is evident from the Smith Chart presented in Figure 6.23, signifying the changes in the output impedance as a result of the device's exposure to TID. It follows that modifications in the output impedance matching network may be required as the device's exposure to TID is increased.

The impact of TID on the activity of the device is analyzed by assessing U pre-and post-radiation in Figure 6.24.

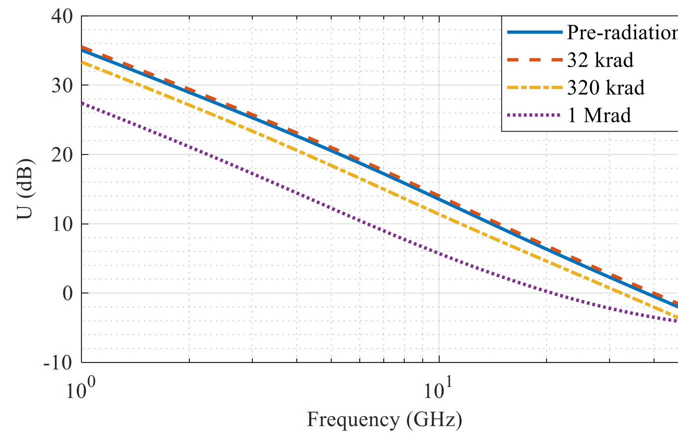

Figure 6.24: Unilateral gain at various d values for NMOS device with gate width of 50 µm

It is evident that U reduces with increase in d as shown in Figure 6.24. Furthermore, it is clear that the 0 dB intercept reduces with increase in d signifying reducing f_{max} with increase in exposure to TID.

The performance of the device pre-and post-radiation is further analyzed by evaluating $|S_{21}|$ and $|A_i|$ in Figure 6.25 and Figure 6.26 respectively.

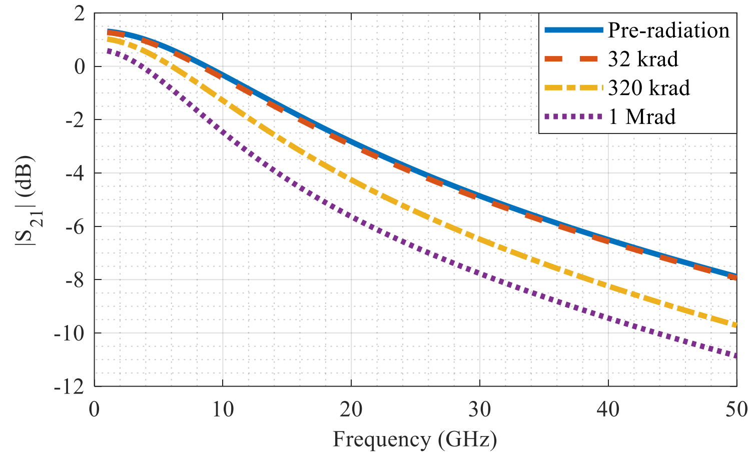

Figure 6.25: $|S_{21}|$ at various d values for NMOS device with gate width of 50 µm

It has been shown that $|S_{21}|$ decreases as d increases signifying damage of the device due to TID.

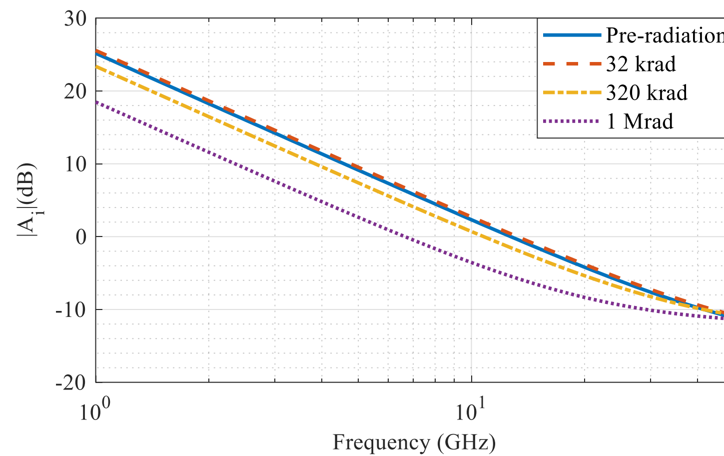

Figure 6.26: $|A_i|$ at various d values for NMOS device with gate width of 50 µm

It has been shown in Figure 6.26 that $|A_i|$ reduces with increase in d. Furthermore, the 0 dB intercept also reduced with increase in d signifying a reduction in f_t as the device gets exposed to TID.

The analysis of the impact of TID on the performance of the NMOS device with gate width of 50 µm is done by evaluating the f_t values obtained from the 0 dB intercept of Figure 6.26

and the f_{max} values obtained from the 0 dB intercept of Figure 6.24 pre-and post-radiation using Table 6.4.

Table 6.4: Pre-and post-radiation values of f_t and f_{max} for a device with gate width of 50 µm

Radiation dose (*d*)	**f_t (GHz)**	**f_{max} (GHz)**
Pre-radiation	23.73	39.56
32 krad	21.96	39.33
110 krad	19.98	38.92
210 krad	19.70	36.62
320 krad	18.20	33.58
430 Mrad	17.35	28.69
1 Mrad	8.91	19.96

The values of both f_t and f_{max} reduce with increase in d as shown in Table 6.4 signifying the reduced performance of the NMOS device caused by TID.

CHAPTER 7 CONCLUSION

This chapter will present the general conclusions based on analyses in Chapters 4 to 6, and provide a critical analysis of research objectives. The chapter will provide answers to research questions based on experimental results and evaluate if the objectives of the research have been met. Challenges and limitations of the work will then be discussed and the chapter will conclude with recommendations for future works.

7.1 GENERAL CONCLUSION BASED ON THE DISCUSSION

7.1.1 General conclusion on SiGe HBT

The derived small signal model for SiGe HBT from measured results compared well with both measured S-parameters and S-parameters from the model in the PDK over the entire frequency range of interest. The derived model equations are therefore considered accurate and reliable.

The curves that were used to derive the small signal model equations, fitted well with measured data, with the minimum R^2 value for g_m greater than 0.92 while the curves for rest of the small signal parameters had R^2 values all greater than 0.99. The value of 0.92 is indeed an indication that the derived exponential curves relating each of the small signal parameters to radiation dose accurately approximated the measured data and can therefore predict changes in the small signal model when the device is exposed to radiation.

From the results shown in Section 4.3, it can be concluded that *NF* increases with increase in *d* while R_n reduces with increase in *d,* confirming research findings in [29].

The extracted small signal parameters showed a general pattern of increase in all the small signal parameter resistances and capacitances while g_m decreased with increase in d. This is consistent with previous studies [4]. It can therefore be concluded that ionizing radiation degrades SiGe HBTs by increasing resistances and capacitances and decreasing g_m. There minor changes shown on the Smith Charts of S_{22} and Smith Chart S_{11} in Section 6.2 lead to conclusion that TID does not significantly affect the output or input impedance of SiGe HBTs, although there is marginally greater influence at the output compared to the input.

It was further shown that the U of the device decreased with increase in d in the entire frequency range. Furthermore, as the device's exposure to TID was increased, the f_t and f_{max} of the device decreased. It can therefore be concluded from the presented data in Section 6.2, that an increase in TID reduces $|S_{21}|$, $|A_i|$, U, f_t and $f_{max.}$ Again, it should, however, be pointed out that only minor degradation is observed over the dose range, limiting the veracity of the findings. A repeat experiment with a larger dose range, to observe greater parameter variation, is highly recommended.

7.1.2 General conclusion on bulk CMOS devices

Transistors in the PDK model for the 0.35 µm C35B3C3 CMOS process have been characterised up to 6 GHz. It therefore follows that the comparison beyond 6 GHz should not be considered reliable. The derived model, however, compared reasonably well with the model in the PDK up to 6 GHz, and with measured S-parameters up to 50 GHz. The extracted model is therefore considered reliable and can be used to infer small signal model changes due to ionizing radiation.

The small signal model parameter $C_{gs,}$ for the device (total gate width of 10 µm), with the worst fitting curve had R^2 of 0.9687. The other small signal for the device featured curve fits with $R^2 > 0.97$. In the rest of the bulk CMOS devices, the curve fit produced a minimum R^2 above 0.96 for all small signal parameters. It can therefore be concluded that the derived model equations can accurately predict changes in the small signal parameters when the devices are exposed to radiation.

The extracted small signal parameters in bulk CMOS devices also showed a general pattern of increase in all the small signal parameter resistances and capacitances and a decrease in g_m. This led to the conclusion that ionizing radiation degrades bulk CMOS devices by increasing resistances and capacitances and decreasing g_m.

From the Smith Charts for S_{11} and S_{22} in Section 6.4, it was shown that TID affected the input impedance of the device significantly, but the output impedance to a far less extent. It was further shown that transistors with larger gates suffered more damage due to TID than those with smaller gates, as evidenced by the large changes shown on the Smith Charts for S_{11} and S_{22} for larger gates compared to the changes for transistors with smaller gates after radiation. This agrees well with previous research findings.

It was further shown than TID reduced $|S_{21}|$, $|A_i|$, U, f_T and f_{max}, which is in agreement with previous research finding.

7.2 CONCLUSION BASED ON RESEARCH OBJECTIVES

The research objectives were to model changes in the small signal parameters for SiGe HBT and for bulk CMOS devices at constant voltage biases against TID at mm-wave and microwave frequencies. This has been met, as equations relating each of the small signal model parameters to TID were derived and validated for both SiGe HBT and bulk CMOS devices. From this research study, the model parameter variations that lead to the overall changes previously reported in literature are now known, for the first time.

7.3 LIMITATIONS AND CHALLENGES

The first challenge faced in this research was that measurement of S-parameters could not be done in situ, as the available setup only allowed for remote radiation experiment. Furthermore, the devices were not radiated under DC bias, as it proved challenging to do so with the available equipment.

Secondly, it was also not possible to adhere to all of the ESA-ESCC 22900 radiation testing guidelines due to the available equipment. However, it is anticipated that testing under the exact criteria will produce results qualitatively similar to what were observed here.

The other challenge was that noise measurements could not be performed for both SiGe HBT and bulk CMOS devices in this work. Successful noise measurement of the selected SiGe HBT and bulk CMOS devices required the use of muxcouplers in the setup as well as substantial Y-factor. Muxcouplers, however, introduce losses, which lowers the Y-factor thereby affecting noise measurement. As pointed out previously, the observed degradation of the SiGe device was only minor over the dose range, which may lead to a significant margin for error in the deduced results.

7.4 RECOMMENDATIONS FOR FUTURE WORKS

Radiation experiments were done with the terminals of the devices floating in the radiation lab, while linear measurements were done in a separate lab within an hour after radiation exposure. Future experiments should carry out the radiation experiment with linear measurements so as to characterise with S-parameters obtained from devices in their biased condition. In the case of the SiGe HBT, these tests should also then be completed over a larger dose range.

In this research, the full frequency sweep from 1 GHz to 110 GHz was covered for SiGe HBT while for bulk CMOS devices, characterisation was done from 1 GHz to 50 GHz. These frequency ranges are too wide for a study were interest is on mm-wave frequencies. Future works should consider focusing on smaller frequency bands of specific interest to mm-wave applications.

Exponential curve fitting of the form $Ae^{B.d}+C$ was used in the study. There are, however, other fitting functions possible, including a simple linear fit. Future works could consider different fitting functions and also consider repeating the experiment for a statistically significant sample of devices, to see if the fitting and derived equations hold.

In this research study, the derived equations did not relate changes in small signal parameters due to radiation to gate width, but only related the changes to d. Future works could consider deriving equations that would factor in the size of the gate for bulk CMOS devices and the size of the base for SiGe HBTs.

The work in this research focused on small signal linear models around single bias points in both SiGe HBT and bulk CMOS devices. Future work should consider characterisation and modelling of radiation induced changes in non-linear models at various bias points, such as in the EKV or ACM models.

In this study, the slow recoveries due to annealing at room temperature (once the devices were removed from the radiation source) were not taken into consideration. Future works could consider taking this into consideration.

REFERENCES

[1] Y. Yu, P. G. M. Baltus, and A. H. M. Van Roermund, *Integrated 60GHz RF beamforming in CMOS*. Springer Science & Business Media, 2011.

[2] F. Alimenti, V. Palazzari, A. Battistini, L. Aluigi, S. M. WHITE, and L. ROSELLI, “A System-on-Chip millimeter-wave radiometer for the space-based observation of solar flares,” in *15th Conference on Microwave Techniques COMITE 2010*, 2010, pp. 3–8.

[3] J. D. Cressler, “Radiation Effects in SiGe Technology,” *IEEE Trans. Nucl. Sci.*, vol. 60, no. 3, pp. 1992–2014, Jun. 2013.

[4] F. B. Ergin, R. Turan, S. T. Shishiyanu, and E. Yilmaz, “Effect of γ-radiation on HfO2 based MOS capacitor,” *Nucl. Instruments Methods Phys. Res. Sect. B Beam Interact. with Mater. Atoms*, vol. 268, no. 9, pp. 1482–1485, May 2010.

[5] J. D. Cressler, “On the potential of SiGe HBTs for extreme environment electronics,” *Proc. IEEE*, vol. 93, no. 9, pp. 1559–1582, 2005.

[6] A. Madan, S. D. Phillips, J. D. Cressler, P. W. Marshall, Q. Liang, and G. Freeman, “Impact of Proton Irradiation on the RF Performance of 65 nm SOI CMOS Technology,” *IEEE Trans. Nucl. Sci.*, vol. 56, no. 4, pp. 1914–1919, 2009.

[7] H. K. Gummel and H. C. Poon, “An integral charge control model of bipolar transistors,” *Bell Syst. Tech. J.*, vol. 49, no. 5, pp. 827–852, 1970.

[8] H. S. Hajghassem, W. D. Brown, and J. G. Williams, “Neutron dosimetry using the

bipolar transistor Gummel-Poon model parameter C 2," *Nucl. Instruments Methods Phys. Res. Sect. B Beam Interact. with Mater. Atoms*, vol. 61, no. 3, pp. 309–314, 1991.

[9] S. Datta, K. P. Roenker, and M. M. Cahay, "A Gummel–Poon model for pnp heterojunction bipolar transistors with a compositionally graded base," *Solid. State. Electron.*, vol. 44, no. 6, pp. 991–1000, 2000.

[10] B. R. Ryum and I. M. Abdel-Motaleb, "A Gummel-Poon model for abrupt and graded heterojunction bipolar transistors (HBTs)," *Solid. State. Electron.*, vol. 33, no. 7, pp. 869–880, 1990.

[11] F. Fiori and V. Pozzolo, "Modified Gummel-Poon model for susceptibility prediction," *Electromagn. Compat. IEEE Trans.*, vol. 42, no. 2, pp. 206–213, 2000.

[12] H. C. De Graaff and W. J. Kloosterman, "Modeling of the collector epilayer of a bipolar transistor in the Mextram model," *IEEE Trans. Electron Devices*, vol. 42, no. 2, pp. 274–282, 1995.

[13] H. C. De Graaff, W. J. Kloosterman, J. A. M. Geelen, and M. Koolen, "Experience with the new compact MEXTRAM model for bipolar transistors," in *Bipolar Circuits and Technology Meeting, 1989., Proceedings of the 1989*, 1989, pp. 246–249.

[14] U. Basaran, N. Wieser, G. Feiler, and M. Berroth, "Small-signal and high-frequency noise modeling of SiGe HBTs," *Microw. Theory Tech. IEEE Trans.*, vol. 53, no. 3, pp. 919–928, 2005.

[15] S. Bousnina, P. Mandeville, A. B. Kouki, R. Surridge, and F. M. Ghannouchi, "A new analytical and broadband method for determining the HBT small-signal model parameters," in *Microwave Symposium Digest. 2000 IEEE MTT-S International*, 2000, vol. 3, pp. 1397–1400.

[16] J.-L. Olvera-Cervantes, J. D. Cressler, J.-L. Medina-Monroy, T. Thrivikraman, B. Banerjee, and J. Laskar, "A New Analytical Method for Robust Extraction of the

Small-Signal Equivalent Circuit for SiGe HBTs Operating at Cryogenic Temperatures," *Microw. Theory Tech. IEEE Trans.*, vol. 56, no. 3, pp. 568–574, 2008.

[17] H.-Y. Chen, K.-M. Chen, G.-W. Huang, and C.-Y. Chang, "Small-Signal Modeling of SiGe HBTs Using Direct Parameter-Extraction Method," *IEEE Trans. Electron Devices*, vol. 53, no. 9, pp. 2287–2295, Sep. 2006.

[18] K. Lee, K. Choi, S.-H. Kook, D.-H. Cho, K.-W. Park, and B. Kim, "Direct Parameter Extraction of SiGe HBTs for the VBIC Bipolar Compact Model," *IEEE Trans. Electron Devices*, vol. 52, no. 3, pp. 375–384, Mar. 2005.

[19] K. Xia, G. Niu, D. C. Sheridan, and S. L. Sweeney, "Frequency and bias-dependent modeling of correlated base and collector current rf noise in sige hbts using quasi-static equivalent circuit," *IEEE Trans. Electron Devices*, vol. 53, no. 3, pp. 515–522, 2006.

[20] J. D. Cressler and G. Niu, *Silicon-Germanium heterojunction bipolar transistors*. Artech house, 2003.

[21] M. T. Yang, P. P. C. Ho, Y. J. Wang, T. J. Yeh, and Y. T. Chia, "Broadband small-signal model and parameter extraction for deep sub-micron MOSFETs valid up to 110 GHz," in *IEEE Radio Frequency Integrated Circuits (RFIC) Symposium, 2003*, 2003, pp. 369–372.

[22] S. N. Ong, K. S. Yeo, K. W. J. Chew, and L. H. K. Chan, "Substrate-Induced Noise Model and Parameter Extraction for High-Frequency Noise Modeling of Sub-Micron MOSFETs," *IEEE Trans. Microw. Theory Tech.*, vol. 62, no. 9, pp. 1973–1985, Sep. 2014.

[23] N. Facts and J. S. Center, "Understanding Space Radiation," FS-2002-10-080-JSC, Oct, 2002.

[24] E. R. Benton and E. V Benton, "Space radiation dosimetry in low-Earth orbit and beyond," *Nucl. Instruments Methods Phys. Res. Sect. B Beam Interact. with Mater.*

Atoms, vol. 184, no. 1, pp. 255–294, 2001.

[25] J. M. Roldan, W. E. Ansley, J. D. Cressler, S. D. Clark, and D. Nguyen-Ngoc, "Neutron radiation tolerance of advanced UHV/CVD SiGe HBT BiCMOS technology," *IEEE Trans. Nucl. Sci.*, vol. 44, no. 6, pp. 1965–1973, 1997.

[26] B. M. Haugerud *et al.*, "Proton and gamma radiation effects in a new first-generation SiGe HBT technology," *Solid. State. Electron.*, vol. 50, no. 2, pp. 181–190, 2006.

[27] Shiming Zhang, Guofu Niu, J. D. Cressler, S. D. Clark, and D. C. Ahlgren, "The effects of proton irradiation on the RF performance of SiGe HBTs," *IEEE Trans. Nucl. Sci.*, vol. 46, no. 6, pp. 1716–1721, 1999.

[28] L. W. Massengill, "Radiation Effects in Si CMOS Platforms," in *Extreme Environment Electronics*, CRC Press, 2012, pp. 155–174.

[29] S. Venkataraman *et al.*, "Impact of proton irradiation on the RF performance of 0.12 μm CMOS technology [MOSFET devices]," in *Reliability Physics Symposium, 2005. Proceedings. 43rd Annual. 2005 IEEE International*, 2005, pp. 356–359.

[30] J. M. Lauenstein, "Standards for Radiation Effects Testing: Ensuring Scientific Rigor in the Face of Budget Realities and Modern Device Challenges," 2015.

[31] H. Hemmati, *Deep space optical communications*, vol. 11. John Wiley & Sons, 2006.

[32] E. B. S. No, "22900,'Total dose steady-state irradiation test method,' Issue 3 (2007).".

[33] National Institute of Standards and Technology, "ESTAR: Stopping powers and ranges for electrons," *National institute of stanadards and technology*, 2019. [Online]. Available: https://physics.nist.gov/PhysRefData/Star/Text/ESTAR.html.

[34] The Radiation Dose Assessment, "External Dose Assessment," *RADAR-The Decay Data*, 2019. [Online]. Available: http://www.doseinfo-radar.com/RADARDecay.html.

[35] H. T. Mebrahtu, W. Gao, W. E. Kieser, X. L. Zhao, P. J. Thomas, and R. I. Hornsey, “SPICE models of fluorine-ion-irradiated CMOS devices,” *IEEE Trans. Electron Devices*, vol. 54, no. 8, pp. 1963–1971, 2007.

[36] J. Gao, *Heterojunction Bipolar Transistors for circuit design: microwave modeling and parameter extraction*. John Wiley & Sons, 2015.

[37] J. Stenarson and K. Yhland, “A Reformulation and Stability Study of TRL and LRM Using S-Parameters,” *IEEE Trans. Microw. Theory Tech.*, vol. 57, no. 11, pp. 2800–2807, Nov. 2009.

[38] X. Wei *et al.*, “An improved on-chip 4-port parasitics de-embedding method with application to RF CMOS,” in *Silicon Monolithic Integrated Circuits in RF Systems, 2007 Topical Meeting on*, 2007, pp. 24–27.

[39] Q. Liang *et al.*, “A simple 4-port parasitic de-embedding methodology for high-frequency characterization of SiGe HBTs,” in *Radio Frequency Integrated Circuits (RFIC) Symposium, 2003 IEEE*, 2003, pp. 357–360.

[40] B. Banerjee, S. Venkataraman, C.-H. Lee, and J. Laskar, “Broadband noise modeling of SiGe HBT under cryogenic temperatures,” in *Radio Frequency Integrated Circuits (RFIC) Symposium, 2007 IEEE*, 2007, pp. 765–768.

[41] B. Razavi, R.-H. Yan, and K. F. Lee, “Impact of distributed gate resistance on the performance of MOS devices,” *IEEE Trans. Circuits Syst. I Fundam. Theory Appl.*, vol. 41, no. 11, pp. 750–754, 1994.

[42] Y. Li *et al.*, “Study of γ-ray irradiation influence on TiN/HfO2/Si MOS capacitor by C-V and DLTS,” *Superlattices Microstruct.*, vol. 120, pp. 313–318, Aug. 2018.

APPENDICES

1. SiGe HBT MATLAB Code for Parameter extraction and model validation

```
clc;clear;
format long
%% De-embedding data
d1       = read(rfdata.data,'open_pre_rad.S2P');
d2       = read(rfdata.data,'short_pre_rad.S2P');
d3       = read(rfdata.data,'hbt_pre_rad.S2P');
d4       = read(rfdata.data,'hbt_simp_embedded_mod.S2P');%% Embedded with
extracted parasitics.
d5       = read(rfdata.data,'hbt_comp_embedded_mod.S2P');%% Embedded with
extracted parasitics.

fm       = d4.Freq;
fd       = d3.Freq;
w        = 2.*pi.*fd;
I_b      = 24.63e-6;
I_c      = 5.473e-3;
k1       = 1.38064852e-23;
q        = 1.60217662e-19;
To       = 290;

%% Exctraction of parameters from de-embedding data
y_pad    = extract(d1,'Y_PARAMETERS');
z_pad    = extract(d2,'Z_PARAMETERS');
y_D      = extract(d3,'Y_PARAMETERS');
s_D      = extract(d3,'S_PARAMETERS',50);
s_M      = extract(d4,'S_PARAMETERS',50);
s_C      = extract(d5,'S_PARAMETERS',50);
h_D      = extract(d3,'H_PARAMETERS');

%% Y-parameters from the open calibration standard
yp11 = shiftdim(y_pad(1,1,:));
yp12 = shiftdim(y_pad(1,2,:));
yp21 = shiftdim(y_pad(2,1,:));
yp22 = shiftdim(y_pad(2,2,:));

%% Z-Parameters from the short calibration standard
zp11 = shiftdim(z_pad(1,1,:));
zp12 = shiftdim(z_pad(1,2,:));
zp21 = shiftdim(z_pad(2,1,:));
zp22 = shiftdim(z_pad(2,2,:));
```

```
%% Y-Parameters of the extrinsic transistor
yD11 = shiftdim(y_D(1,1,:));
yD12 = shiftdim(y_D(1,2,:));
yD21 = shiftdim(y_D(2,1,:));
yD22 = shiftdim(y_D(2,2,:));

%% H-Parameters
h_11 = shiftdim(h_D(1,1,:));
h_12 = shiftdim(h_D(1,2,:));
h_21 = shiftdim(h_D(2,1,:));
h_22 = shiftdim(h_D(2,2,:));

%% Extraction of S-parameters from model and experimental results
sM11 = shiftdim(s_M(1,1,:));
sM12 = shiftdim(s_M(1,2,:));
sM21 = shiftdim(s_M(2,1,:));
sM22 = shiftdim(s_M(2,2,:));

sD11 = shiftdim(s_D(1,1,:));
sD12 = shiftdim(s_D(1,2,:));
sD21 = shiftdim(s_D(2,1,:));
sD22 = shiftdim(s_D(2,2,:));

sC11 = shiftdim(s_C(1,1,:));
sC12 = shiftdim(s_C(1,2,:));
sC21 = shiftdim(s_C(2,1,:));
sC22 = shiftdim(s_C(2,2,:));

%% Extraction of pad capacitances from the open calibration standard
Cbco  = -imag(yp12)./w;
Cbeo  = (imag(yp11)+imag(yp12))./w;
Cbcp  = (imag(yp22)+imag(yp21))./w;

%% Extraction of pad resistances and inductances from the short
calibration standard
Rbx   = real(zp11)-real(zp12);
Rc    = real(zp22)-real(zp21);
Re    = real(zp12);
Lb    = imag(zp11-zp12)./w;
Le    = imag(zp12)./w;
Lc    = imag(zp22-zp21)./w;

%% De-emebedding of parasitic capacitances, inducatnaces and resistances

for no=1:length(Cbeo)
    Mj(:,:,no) = [j.*w(no).*(Cbeo(no)+Cbco(no)) -j.*w(no).*Cbco(no); -
j.*w(no).*Cbco(no) j.*w(no).*(Cbcp(no)+Cbco(no))];
    Yj(:,:,no) = y_D(:,:,no)-Mj(:,:,no);
    Zj(:,:,no) = inv(Yj(:,:,no));
    Nj(:,:,no) =
[(Rbx(no)+Re(no))+j.*w(no).*(Lb(no)+Le(no)),Re(no)+j.*w(no).*Le(no);Re(no
)+j.*w(no).*Le(no),(Rc(no)+Re(no))+j.*w(no).*(Lc(no)+Le(no))];
    Zk(:,:,no) = Zj(:,:,no)-Nj(:,:,no);
    Yk(:,:,no) = inv(Zk(:,:,no));
```

```
    Hk(:,:,no) = y2h(Yk(:,:,no));
    Sk(:,:,no) = y2s(Yk(:,:,no),50);

end

 y11 = shiftdim(Yk(1,1,:));
 y12 = shiftdim(Yk(1,2,:));
 y21 = shiftdim(Yk(2,1,:));
 y22 = shiftdim(Yk(2,2,:));

 h11 = shiftdim(Hk(1,1,:));
 h12 = shiftdim(Hk(1,2,:));
 h21 = shiftdim(Hk(2,1,:));
 h22 = shiftdim(Hk(2,2,:));

 s11 = shiftdim(Sk(1,1,:));
 s12 = shiftdim(Sk(1,2,:));
 s21 = shiftdim(Sk(2,1,:));
 s22 = shiftdim(Sk(2,2,:));

 %% Extraction of intrinsic base resistance
 Rbi    = real(1./y11);

 %% Extraction of Cbc and Cbep
 A     = imag((y11.*y22-y12.*y21)./(y11+y21))./w;
 B     = (Rbi.*real((y11.*y22-y12.*y21)./(y22+y12))).^-1;
 Cbc   = A.*B;
 Cbep  = A-Cbc;

%% Extraction of Substrate parasitics Ccso and Rs
 Ccso    = -(w.*imag(1./(y12+y22))).^-1;
 Rs      = real(1./(y12+y22-j.*w.*Ccso));

 %% Extraction of gm, Rbe and Cbe
 Ybep   = j.*w.*Cbep;
 Ybc    = j.*w.*Cbc;
 gm     = (real(1./(y21-y12))-Rbi.*real((y11+y12)./(y21-y12))).^-1;
 Ypi    = ((-y11.*(1+Rbi.*Ybc)+Ybc.*(1+Rbi.*Ybep)+Ybep))./(Rbi.*(y11-
Ybep)-1);
 Rbe    = 1./(real(Ypi));
 Cbe    = (imag(Ypi))./w;

 %% Noise modelling using Y-Parameters
 S_in    = (2*q*I_b + (2*q*I_c./((abs(h21)).^2)));
 S_invn = 2*q*I_c.*(y11./(abs(y21)).^2);
 S_vn    = (2*q*I_c)./((abs(y21)).^2)+4*k1*To*Rbi;

%% Calculation of noise parameters
 Rn    = S_vn./(4*k1*To);
 G     = sqrt((S_in./S_vn)-(imag(S_invn)./(S_vn)).^2);
 B     = -imag(S_invn)./S_vn;
 NF    = 1 + 2*Rn_prerad.*(G_prerad+(real(S_invn)./S_vn));
 Y     = G_prerad + j.*B_prerad;
```

2. SiGe HBT MATLAB Code for model usage demonstration

```
clc;clear;
format long
d1       = read(rfdata.data,'hbt_rad4.s2p');
d2       = read(rfdata.data,'HBTSimModel.S2P');
d3       = read(rfdata.data,'open_pre_rad.S2P');
d4       = read(rfdata.data,'short_pre_rad.S2P');

fm       = d1.Freq;
w        = 2*pi*fm;
SM1      = extract(d1,'S_PARAMETERS',50);
SM2      = extract(d2,'S_PARAMETERS',50);

y_pad = extract(d3,'Y_PARAMETERS');
z_pad = extract(d4,'Z_PARAMETERS');

sd_11 = shiftdim(SM1(1,1,:));
sd_12 = shiftdim(SM1(1,2,:));
sd_21 = shiftdim(SM1(2,1,:));
sd_22 = shiftdim(SM1(2,2,:));

s_11  = shiftdim(SM2(1,1,:));
s_12  = shiftdim(SM2(1,2,:));
s_21  = shiftdim(SM2(2,1,:));
s_22  = shiftdim(SM2(2,2,:));

%% Y-parameters from the open calibration standard
yp11 = shiftdim(y_pad(1,1,:));
yp12 = shiftdim(y_pad(1,2,:));
yp21 = shiftdim(y_pad(2,1,:));
yp22 = shiftdim(y_pad(2,2,:));

%% Z-Parameters from the short calibration standard
zp11 = shiftdim(z_pad(1,1,:));
zp12 = shiftdim(z_pad(1,2,:));
zp21 = shiftdim(z_pad(2,1,:));
zp22 = shiftdim(z_pad(2,2,:));

%% Extraction of pad capacitances, resistances and inductances
Cbco  = -imag(yp12)./w;
Cbeo  = (imag(yp11)+imag(yp12))./w;
Cbcp  = (imag(yp22)+imag(yp21))./w;
Rbx   = real(zp11)-real(zp12);
Rc    = real(zp22)-real(zp21);
Re    = real(zp12);
Lb    = imag(zp11-zp12)./w;
Le    = imag(zp12)./w;
Lc    = imag(zp22-zp21)./w;

%% Calculated values pre-radiation using the Matlab code stated above
```

```
R_bi   = 31.61;
R_be   = 1.99e3;
C_be   = 81.11e-15;
C_bc   = 3.96e-15;
g_m    = 0.125000;
C_bep = 2.938e-15;
R_s    = 100.69;
C_cso = 0.1000e-15;
C_bcp = 27.83e-15;
freq    = transpose([1e9:109000000:110e9]);

%% Extract y-parameters
Y_pi = (1./R_be)+j.*w.*C_be;
Y_bc = j.*w.*C_bc;
Y_bcp= j.*w.*C_bcp;
Y_bep= j.*w.*C_bep;
%%
y_11 = (Y_pi+Y_bc)./(1+R_bi.*(Y_pi +Y_bc))+Y_bep;
y_12 = (-Y_bc)./(1+R_bi.*(Y_pi+Y_bc))-Y_bep;
y_21 = ((g_m-Y_bc)./(1+R_bi.*(Y_pi+Y_bc)))-Y_bep;
y_22 =
(Y_bc+R_bi.*Y_bc.*((w./w).*g_m+Y_pi))./(1+R_bi.*(Y_pi+Y_bc))+Y_bep;

%% Converting Y -params to S, H and Z-Params
for no=1:length(Y_pi2)
    Y_p(:,:,no)  = [y_11(no) y_12(no); y_21(no) y_22(no)];
    Hk(:,:,no)   = y2h(Y_p(:,:,no));
    Sk(:,:,no)   = y2s(Y_p(:,:,no),50);
    Zk(:,:,no)   = inv(Y_p(:,:,no));
end

s_11 = shiftdim(Sk(1,1,:));
s_12 = shiftdim(Sk(1,2,:));
s_21 = shiftdim(Sk(2,1,:));
s_22 = shiftdim(Sk(2,2,:));

h_11 = shiftdim(Hk(1,1,:));
h_12 = shiftdim(Hk(1,2,:));
h_21 = shiftdim(Hk(2,1,:));
h_22 = shiftdim(Hk(2,2,:));

z_11 = shiftdim(Zk(1,1,:));
z_12 = shiftdim(Zk(1,2,:));
z_21 = shiftdim(Zk(2,1,:));
z_22 = shiftdim(Zk(2,2,:));


%% Unilateral power gain
U   = 10*log10(((abs(y1_21-y1_12)).^2)./(4.*((real(y1_11)).*real(y1_22))-
(real(y1_12).*real(y1_21))));

%% Current gain
Ai = 20*log10(abs(h1_21));
```

```
%% Noise modelling using Y-Parameters

I_b = 24.63e-6;
I_c = 5.473e-3;
k = 1.38064852e-23;
q = 1.60217662e-19;
To = 290;

S_in   = (2*q*I_b + (2*q*I_c./((abs(h_21)).^2)));
S_invn = 2*q*I_c.*(y_11./(abs(y1_21)).^2);
S_vn   = (2*q*I_c)./((abs(y_21)).^2)+4*k*To*R_bi;

%% Calculation of noise parameters
Rn_a = Sa_vn./(4*k*To);
G_a  = sqrt((Sa_in./Sa_vn)-(imag(Sa_invn)./(Sa_vn)).^2);
B_a  = -imag(Sa_invn)./Sa_vn;
NF_a = 1 + 2*Rn_a.*(G_a+(real(Sa_invn)./Sa_vn));
Y_a  = G_a + 1i.*B_a;
F_a  =  (1-Y_a.*50)./(1+Y_a.*50);
```

3. Bulk CMOS MATLAB Code for parameter extraction and model validation

```
clc
clear
close all
%% Load Parameters Pre-rad
dat          = read(rfdata.data,'nmos_pre_rad.s2p');
Sm           = extract(dp,'S_PARAMETERS',50);
SReflect     = sparameters('Reflect_pre_rad.s2p');
Sthru        = sparameters('Thru_pre_rad.s2p');
Sline        = sparameters('Line_pre_rad.s2p');
Sd           = sparameters('nmos_pre_rad.s2p');
yc_params    = extract(dat,'Y_PARAMETERS');

%% Extract the frequency
freq         = dat.Freq;
w            = 2.*pi.*freq;
w2           = w.^2;

%% Extraction of measured  thru stand Sparameters of individual
components
Sthru11=rfparam(Sthru,1,1);
Sthru12=rfparam(Sthru,1,2);
Sthru21=rfparam(Sthru,2,1);
Sthru22=rfparam(Sthru,2,2);
SthruT=[Sthru11,Sthru12,Sthru21,Sthru22];

%% Extraction of measured  short stand Sparameters of individual
components
SReflect11=rfparam(SReflect,1,1);
SReflect12=rfparam(SReflect,1,2);
```

```
SReflect21=rfparam(SReflect,2,1);
SReflect22=rfparam(SReflect,2,2);
SReflectT=[SReflect11,SReflect12,SReflect21,SReflect22];

%% Extraction of measured  line stand Sparameters of individual
components
Sline11=rfparam(Sline,1,1);
Sline12=rfparam(Sline,1,2);
Sline21=rfparam(Sline,2,1);
Sline22=rfparam(Sline,2,2);
SlineT=[Sline11,Sline12,Sline21,Sline22];

%% Extraction of measured NMOS Sparameters of individual components
sd11=rfparam(Sd,1,1);
sd12=rfparam(Sd,1,2);
sd21=rfparam(Sd,2,1);
sd22=rfparam(Sd,2,2);
sdT=[sd11,sd12,sd21,sd22];

%% Extraction of modelled NMOS S-parameters before radiation
sm11=shiftdim(Sm(1,1,:));
sm12=shiftdim(Sm(1,2,:));
sm21=shiftdim(Sm(2,1,:));
sm22=shiftdim(Sm(2,2,:));

%% Extraction of S-parameters for the model
Sd11=rfparam(Sd,1,1);
Sd12=rfparam(Sd,1,2);
Sd21=rfparam(Sd,2,1);
Sd22=rfparam(Sd,2,2);

sm_11=shiftdim(Sm(1,1,:));
sm_12=shiftdim(Sm(1,2,:));
sm_21=shiftdim(Sm(2,1,:));
sm_22=shiftdim(Sm(2,2,:));

yc11 = shiftdim(yc_params(1,1,:));
yc12 = shiftdim(yc_params(1,2,:));
yc21 = shiftdim(yc_params(2,1,:));
yc22 = shiftdim(yc_params(2,2,:));


%% Call the TRL function
[Sx,GL]=trl(SthruT,SReflectT,SlineT,sdT,freq);

si11 = Sx(:,1);
si12 = Sx(:,2);
si21 = Sx(:,3);
si22 = Sx(:,4);

for no=1:length(si11)
    Si(:,:,no) = [si11(no) si12(no);si21(no) si22(no)];
end
y_params = s2y(Si,50);
```

```
y11 = shiftdim(y_params(1,1,:));
y12 = shiftdim(y_params(1,2,:));
y21 = shiftdim(y_params(2,1,:));
y22 = shiftdim(y_params(2,2,:));

%% Extraction of small signal parameters
A_1 = -imag(y12);
P_1= polyfit(w,A_1,1);
A_1poly = polyval(P_1,w);
Cgd   = P_1(1);
A_2 = imag(y11)+imag(y12);
perCent=1;
nPoint=floor(perCent*length(A_2));
P_2= polyfit(w(1:nPoint),A_2(1:nPoint),1);
A_2poly = polyval(P_2,w);
Cgs = P_2(1);
A_3 = real(y11);
a_3 = (imag(y11)).^2;
perCent=1;
nPoint=floor(perCent*length(A_3));
P_3= polyfit(a_3(1:nPoint),A_3(1:nPoint),1);
A_3poly = polyval(P_3,a_3);
Rg  = P_3(1);
A = real(y21);
P1= polyfit(w2,A,1);
Apoly = polyval(P1,w2);
gm  = P1(2);

B = imag(y21);
P2= polyfit(w,B,1);
Bpoly = polyval(P2,w);
m1  = P2(1);
Cdg = -m1-(Cgd+Cgs).*Rg.*gm;

C = real(y22);
P3 = polyfit(w2,C,1);
Cpoly=polyval(P3,w2);
gds= P3(2);

Ya  = (w2.*Cgd.*Rg.*((Cgd+Cgs).*Rg.*gm+Cdg)+j.*w.*Cgd.*Rg.*(gm-
w2.*Cgd.*Rg.*(Cgd+Cgs)))./(1+w2.*Rg.^2.*(Cgd+Cgs).^2);
R   = real(y22)-gds-real(Ya);
I   = imag(y22)-w.*Cgd-imag(Ya);

D       = w2./R;
P4      = polyfit(w2,D,1);
Dpoly   = polyval(P4,w2);
mr  = P4(1);
cr  = P4(2);

E = w.*I./R;
P5      = polyfit(w2,E,1);
Epoly   = polyval(P5,w2);
mi  = P5(1);
```

```
ci  = P5(2);
Cdb = mi./mr;

F = I./w;
P6 = polyfit(w2,F,1);
Fpoly=polyval(P6,w2);
g= P6(2);
gmbRbb = (g./Cdb)-1;

p = 2 - ((mi.^2.*cr)./mr).*(gmbRbb).^2;
q = 2.*Cdb-2.*(mi.^2.*cr./mr).*(gmbRbb.*Cdb).*(1+gmbRbb);
r = Cdb.^2.*(1-(mi.^2.*cr./mr).*(1+gmbRbb).^2);
Cbb = ((-q+sqrt(q.^2 -4.*p.*r))./(2.*p));
Rbb = (1./(Cbb.*(Cdb+Cbb))).*(sqrt((mr./cr).*(Cbb.^2+(Cdb+Cbb).^2)));

a   = Rbb.^3.*Cdb.*Cbb.^2.*(Cdb.*(1+gmbRbb)+gmbRbb.*Cbb);
b   = Rbb.*Cdb.*(Cdb.*(1+gmbRbb)+gmbRbb.*Cbb);
c   = Rbb.^2.*(Cbb.^2+(Cdb+Cbb).^2);
d   = Rbb.^4.*Cbb.^2.*(Cdb+Cbb).^2;
e   = Rbb.^4.*Cdb.*Cbb.^3.*(Cdb+Cbb);
f   = Rbb.^2.*Cdb.*Cbb.*(Cdb+Cbb.*(1+gmbRbb));

G   = I-(w.^5.*e+w.^3.*f+w.*g)./(1+w2.*c+w.^4.*d);
Q4= polyfit(w,G,1);
Gpoly = polyval(Q4,w);
Csd  = Q4(1);
```

4. TRL function Code for 2nd tier calibration

```
The TRL function code was written by C. van Niekerk, on 07/06/1995 based
on the work presented in the following paper:

G.F. Engen, C.A. Hoer, "Thru-Reflect-Line: An Improved Technique for
Calibrating the Dual Six-Port Automatic Network Analyser," IEEE Trans.
MTT, Vol. 27,No. 12, December 1979, pp. 987-998

function [Sx,GL]=trl(Sthru,Sopen,Sline,Sdut,freq);

 % Define the imaginary constant

i=sqrt(-1);

% Convert the measured s-parameters of the DEVICE to one variable

S11d = Sdut(:,1);
S21d = Sdut(:,2);
S12d = Sdut(:,3);
S22d = Sdut(:,4);

% Convert the measured s-parameters of the REFLECT standerd to one
variable

S11r = Sopen(:,1);
S22r = Sopen(:,4);
```

```
% Convert the measured s-parameters of the THRU standerd to one variable

S11t = Sthru(:,1);
S21t = Sthru(:,2);
S12t = Sthru(:,3);
S22t = Sthru(:,4);

% Convert the measured s-parameters of the LINE standerd to one variable

S11l = Sline(:,1);
S21l = Sline(:,2);
S12l = Sline(:,3);
S22l = Sline(:,4);

% Compute the wave cascading matrix for the thru standerd

R11t = -(S11t.*S22t - S12t.*S21t)./S21t;
R12t =  S11t./S21t;
R21t = -S22t./S21t;
R22t =  1 ./ S21t;

% Compute the wave cascading matrix for the line standerd

R11l = -(S11l.*S22l - S12l.*S21l)./S21l;
R12l =  S11l./S21l;
R21l = -S22l./S21l;
R22l =  1 ./ S21l;

% Compute the wave cascading matrix for the device standerd

R11m = -(S11d.*S22d - S12d.*S21d)./S21d;
R12m =  S11d./S21d;
R21m = -S22d./S21d;
R22m =  1 ./ S21d;

% Calculate the two possible virtual error networks for port A
% and port B using the s-parameters of the thru and line standerds

% Determine the number of frequency points

nfreq=length(freq);

for n = 1:nfreq

  Rt = [ R11t(n) R12t(n) ; R21t(n) R22t(n) ];
  Rl = [ R11l(n) R12l(n) ; R21l(n) R22l(n) ];
  T  = Rl*inv(Rt);

% Solve a set of quadratic equations to get the values of r11a/r21a
% and r12a/r22a

  A =  T(2,1);
```

```
  B =  T(2,2) - T(1,1);
  C = -T(1,2);

  K1 = (-B + sqrt((B^2)-4*A*C))/(2*A);
  K2 = (-B - sqrt((B^2)-4*A*C))/(2*A);

% Choose between the two possible roots to get the right values for
% b and c/a

  if abs(K1)<abs(K2)
    b  = K1;
    ca = 1/K2;
  end;

  if abs(K2)<abs(K1)
    b  = K2;
    ca = 1/K1;
  end;

% Calculates the propogation constant of the LINE standerd.

  GL(n) = -log(T(1,1)+T(1,2)*ca);

% Calculates "a"

  w1 = S11r(n);
  w2 = S22r(n);

  g =  1/S21t(n);
  d = -(S11t(n)*S22t(n) - S12t(n)*S21t(n));
  e =  S11t(n);
  f = -S22t(n);

  gamma     = (f-d*ca)/(1-e*ca);
  beta_alfa = (e-b)/(d-b*f);

  a = sqrt(((w1-b)*(1+w2*beta_alfa)*(d-b*f))/((w2+gamma)*(1-w1*ca)*(1-
e*ca)));

% Calculates the reflection coeffisients at each port to determine the
correct
% sign that should be assigned to a

  R1a = (w1-b)/(a-w1*a*ca);
  R1b = (w1-b)/(w1*a*ca-a);

% An open is used for the reflection measurement.  Use this information
to
% chose the sign of a

  if abs(angle(R1a)*180/pi)<90
    a = a;
    as(n) = a;
```

```
    c = ca*a;
  end;

  if abs(angle(R1b)*180/pi)<90
    a = -a;
    as(n) = a;
    c = ca*a;
  end;

  R1(n) = (w1-b)/(a-c*w1);

  alfa = (d-b*f)/(a*(1-e*ca));
  beta = beta_alfa*alfa;

  r22p22 = R11t(n)/(a*alfa + b*gamma);

  IRa = [ 1 -b ; -c a ];
  IRb = [ 1 -beta ; -gamma alfa ];

  Rm  = [ R11m(n) R12m(n) ; R21m(n) R22m(n) ];

  Rx = 1/(r22p22*(alfa-gamma*beta)*(a-b*c))*IRa*Rm*IRb;

  S11x(n) =  Rx(1,2)/Rx(2,2);
  S12x(n) =  Rx(1,1) - Rx(1,2)*Rx(2,1)/Rx(2,2);
  S21x(n) =  1/Rx(2,2);
  S22x(n) = -Rx(2,1)/Rx(2,2);

end;

Sx=[S11x.' S21x.' S12x.' S22x.'];
```

5. Bulk CMOS MATLAB Code for model verification and usage demonstration

```
clc
clear
close all

d           = read(rfdata.data,'nmos4_pre_rad.s2p');
Sd          = extract(d,'S_PARAMETERS',50);
frm         = d.Freq;

sd_11=shiftdim(Sd(1,1,:));
sd_12=shiftdim(Sd(1,2,:));
sd_21=shiftdim(Sd(2,1,:));
sd_22=shiftdim(Sd(2,2,:));

%% NMOS 50 um
%% Calculated at Pre-radiation for the NMOS with a total gate width of 50
um using the generated equations from curve fitting
R_g  =  38.600;
C_gd =  4.671e-15;
```

```
C_gs =  100.460e-15;
g_m  =  12.6001e-3;
g_ds =  1./619.43;
C_sd =  45.842e-15;
C_db =  64.915e-15;
C_bb =  90.806e-15;
R_bb =  74.575;
C_dg =  62.520e-15;


%% frequency
f    = transpose([1e9:49000000:50e9]);
w    = 2.*pi.*f;
Y_sub=
(w.^2.*R_bb.*C_db.^2)./(1+w.^2.*R_bb.^2.*(C_db+C_bb).^2)+(j.*w.*C_db+j.*w
.^3.*R_bb.^2.*C_db.*C_bb.*(C_db+C_bb))./(1+w.^2.*R_bb.^2.*(C_db+C_bb).^2)
;

 %% Calculations of Y-params pre-radiation

y_11 =
(w.^2.*(C_gd+C_gs).^2.*R_g+j.*w.*(C_gd+C_gs))./(1+w.^2.*R_g.^2.*(C_gd+C_g
s).^2);
y_12 = (-w.^2.*C_gd.*(C_gd+C_gs).*R_g-
j.*w.*C_gd)./(1+w.^2.*R_g.^2.*(C_gd+C_gs).^2);
y_21 = (g_m-w.^2.*C_dg.*(C_gd+C_gs).*R_g-
j.*w.*((C_gd+C_gs).*R_g.*g_m+C_dg))./(1+w.^2.*R_g.^2.*(C_gd+C_gs).^2);
y_22 =
Y_sub+g_ds+j.*w.*(C_sd+C_gd)+(w.^2.*C_gd.*R_g.*((C_gd+C_gs).*R_g.*g_m+C_d
g)+j.*w.*C_gd.*R_g.*(g_m-
w.^2.*C_gd.*R_g.*(C_gd+C_gs)))./(1+w.^2.*R_g.^2.*(C_gd+C_gs).^2);

%% Converting Y -params to S-Params
for no=1:length(f)
    Ym(:,:,no) = [y_11(no) y_12(no); y_21(no) y_22(no)];
    Sm(:,:,no) = y2s(Ym(:,:,no),50);
    Hm(:,:,no) = y2h(Ym(:,:,no));
end

 s_11 = shiftdim(Sm(1,1,:));
 s_12 = shiftdim(Sm(1,2,:));
 s_21 = shiftdim(Sm(2,1,:));
 s_22 = shiftdim(Sm(2,2,:));

 h_11 = shiftdim(Hm(1,1,:));
 h_12 = shiftdim(Hm(1,2,:));
 h_21 = shiftdim(Hm(2,1,:));
 h_22 = shiftdim(Hm(2,2,:));

%% Calculations of Y-params
y_11 =
(w.^2.*(C_gd+C_gs).^2.*R_g+j.*w.*(C_gd+C_gs))./(1+w.^2.*R_g.^2.*(C_gd+C_g
s).^2);
y_12 = (-w.^2.*C_gd.*(C_gd+C_gs).*R_g-
j.*w.*C_gd)./(1+w.^2.*R_g.^2.*(C_gd+C_gs).^2);
```

```
y_21 = (g_m-w.^2.*C_dg.*(C_gd+C_gs).*R_g-
j.*w.*((C_gd+C_gs).*R_g.*g_m+C_dg))./(1+w.^2.*R_g.^2.*(C_gd+C_gs).^2);
y_22 =
Y_sub+g_ds+j.*w.*(C_sd+C_gd)+(w.^2.*C_gd.*R_g.*((C_gd+C_gs).*R_g.*g_m+C_d
g)+j.*w.*C_gd.*R_g.*(g_m-
w.^2.*C_gd.*R_g.*(C_gd+C_gs)))./(1+w.^2.*R_g.^2.*(C_gd+C_gs).^2);

%% Converting Y -params to S and H-Params
for no=1:length(f)
    Ym(:,:,no) = [y_11(no) y_12(no); y_21(no) y_22(no)];
    Sm(:,:,no) = y2s(Ym(:,:,no),50);
    Hk(:,:,no) = y2h(Ym(:,:,no));
end

 s_11 = shiftdim(Sm(1,1,:));
 s_12 = shiftdim(Sm(1,2,:));
 s_21 = shiftdim(Sm(2,1,:));
 s_22 = shiftdim(Sm(2,2,:));

 h_11 = shiftdim(Hk(1,1,:));
 h_12 = shiftdim(Hk(1,2,:));
 h_21 = shiftdim(Hk(2,1,:));
 h_22 = shiftdim(Hk(2,2,:));

%% Unilateral power gain
 U    = 10*log10(((abs(y_21-y_12)).^2)./(4.*((real(y_11)).*real(y_22))-
(real(y_12).*real(y_21))));

 %% Current gain
 Ai   = 20*log10(abs(h_21));
```

6. TRL function Code for 2nd tier calibration

```
% TRL performs a two-tier TRL calibration for a vector network analyser.
% See TRLPOST.M for some post processing functions that can be performed.
%
% Writer  : C. van Niekerk
% Version : 3.50
% Date    : 07/06/1995

% This code is based on the work in the presented in the following paper:
%
% G.F. Engen, C.A. Hoer, "Thru-Reflect-Line: An Improved Technique for
% Calibrating the Dual Six-Port Automatic Network Analyser,"
% IEEE Trans. MTT, Vol. 27,No. 12, December 1979, pp. 987-998


function [Sx,GL]=trl(Sthru,Sopen,Sline,Sdut,freq);


 % Define the imaginary constant

i=sqrt(-1);
```

```
% Convert the measured s-parameters of the DEVICE to one variable

S11d = Sdut(:,1);
S21d = Sdut(:,2);
S12d = Sdut(:,3);
S22d = Sdut(:,4);

% Convert the measured s-parameters of the REFLECT standerd to one
variable

S11r = Sopen(:,1);
S22r = Sopen(:,4);

% Convert the measured s-parameters of the THRU standerd to one variable

S11t = Sthru(:,1);
S21t = Sthru(:,2);
S12t = Sthru(:,3);
S22t = Sthru(:,4);

% Convert the measured s-parameters of the LINE standerd to one variable

S11l = Sline(:,1);
S21l = Sline(:,2);
S12l = Sline(:,3);
S22l = Sline(:,4);

% Compute the wave cascading matrix for the thru standerd

R11t = -(S11t.*S22t - S12t.*S21t)./S21t;
R12t =  S11t./S21t;
R21t = -S22t./S21t;
R22t =  1 ./ S21t;

% Compute the wave cascading matrix for the line standerd

R11l = -(S11l.*S22l - S12l.*S21l)./S21l;
R12l =  S11l./S21l;
R21l = -S22l./S21l;
R22l =  1 ./ S21l;

% Compute the wave cascading matrix for the device standerd

R11m = -(S11d.*S22d - S12d.*S21d)./S21d;
R12m =  S11d./S21d;
R21m = -S22d./S21d;
R22m =  1 ./ S21d;

% Calculate the two possible virtual error networks for port A
% and port B using the s-parameters of the thru and line standerds

% Determine the number of frequency points
```

```
nfreq=length(freq);

for n = 1:nfreq

  Rt = [ R11t(n) R12t(n) ; R21t(n) R22t(n) ];
  Rl = [ R11l(n) R12l(n) ; R21l(n) R22l(n) ];
  T  = Rl*inv(Rt);

% Solve a set of quadratic equations to get the values of r11a/r21a
% and r12a/r22a

  A =  T(2,1);
  B =  T(2,2) - T(1,1);
  C = -T(1,2);

  K1 = (-B + sqrt((B^2)-4*A*C))/(2*A);
  K2 = (-B - sqrt((B^2)-4*A*C))/(2*A);

% Choose between the two possible roots to get the right values for
% b and c/a

  if abs(K1)<abs(K2)
    b  = K1;
    ca = 1/K2;
  end;

  if abs(K2)<abs(K1)
    b  = K2;
    ca = 1/K1;
  end;

% Calculates the propogation constant of the LINE standerd.

  GL(n)  = -log(T(1,1)+T(1,2)*ca);

% Calculates "a"

  w1 = S11r(n);
  w2 = S22r(n);

  g =  1/S21t(n);
  d = -(S11t(n)*S22t(n) - S12t(n)*S21t(n));
  e =  S11t(n);
  f = -S22t(n);

  gamma      = (f-d*ca)/(1-e*ca);
  beta_alfa = (e-b)/(d-b*f);

  a = sqrt(((w1-b)*(1+w2*beta_alfa)*(d-b*f))/((w2+gamma)*(1-w1*ca)*(1-
e*ca)));
```

```
% Calculates the reflection coeffisients at each port to determine the
correct
% sign that should be assigned to a

  R1a = (w1-b)/(a-w1*a*ca);
  R1b = (w1-b)/(w1*a*ca-a);

% An open is used for the reflection measurement.  Use this information
to
% chose the sign of a

  if abs(angle(R1a)*180/pi)<90
    a = a;
    as(n) = a;
    c = ca*a;
  end;

  if abs(angle(R1b)*180/pi)<90
    a = -a;
    as(n) = a;
    c = ca*a;
  end;

  R1(n) = (w1-b)/(a-c*w1);

  alfa = (d-b*f)/(a*(1-e*ca));
  beta = beta_alfa*alfa;

  r22p22 = R11t(n)/(a*alfa + b*gamma);

  IRa = [ 1 -b ; -c a ];
  IRb = [ 1 -beta ; -gamma alfa ];

  Rm  = [ R11m(n) R12m(n) ; R21m(n) R22m(n) ];

  Rx = 1/(r22p22*(alfa-gamma*beta)*(a-b*c))*IRa*Rm*IRb;

  S11x(n) =  Rx(1,2)/Rx(2,2);
  S12x(n) =  Rx(1,1) - Rx(1,2)*Rx(2,1)/Rx(2,2);
  S21x(n) =  1/Rx(2,2);
  S22x(n) = -Rx(2,1)/Rx(2,2);

end;

Sx=[S11x.' S21x.' S12x.' S22x.'];
```